Geometrically Tunable Optical Properties of Metal Nanoparticles

1

Hao Jing, Li Zhang, and Hui Wang

Contents

H. Jing • L. Zhang • H. Wang (✉)
Department of Chemistry and Biochemistry, University of South Carolina, Columbia, SC, USA

Challa S.S.R. Kumar (ed.), *UV-VIS and Photoluminescence Spectroscopy for Nanomaterials Characterization*, DOI 10.1007/978-3-642-27594-4_1,

1 Definition of the Topic

Noble metal nanoparticles exhibit fascinating geometrically tunable optical properties that are dominated by their localized surface plasmon resonances (LSPRs). By judiciously tailoring the geometric parameters of a metal nanoparticle, one can fine-tune the nanoparticle's optical responses in a precisely controllable manner and thereby selectively implement desired optical properties into nanomaterial systems or nanodevices for specific applications. In this chapter, we present a review on the recent experimental and theoretical advances in the understanding of the geometry–optical property relationship of metallic nanoparticles in various geometries.

2 Overview

Metal nanoparticles are an important class of subwavelength optical components whose optical properties can be fine-tuned over a broad spectral range by tailoring their geometric parameters. The fascinating optical characteristics of metallic nanoparticles are essentially determined by the collective oscillations of free electrons in the metals, known as plasmons. Metallic nanostructures possess geometry-dependent localized surface plasmon resonances, which has stimulated growing interests in a rapidly expanding array of metallic nanoparticle geometries, such as nanorods, nanoshells, nanoprisms, nanostars, and nanocages. The resonant excitation of plasmons also leads to large enhancements of the local electromagnetic field in close proximity to the nanoparticle surface, resulting in dramatically enhanced cross sections for nonlinear optical spectroscopies such as surface-enhanced Raman scattering. These highly tunable plasmonic properties of metal nanoparticles allow for the development of fundamentally new metal-based subwavelength optical elements with broad technological potential, an emerging field known as plasmonics.

The past decades have witnessed significant advances in scientific understanding of the origin of the optical tunability of metallic nanoparticle systems, primarily driven by the rapid advances in the geometry-controlled nanoparticle fabrication and assembly and electrodynamics modeling of nanoparticle systems. In this chapter, we present a state-of-the-art review on the geometrically tunable plasmonic properties of metallic nanostructures in various geometries. We describe, both experimentally and theoretically, the relationship between the particle geometry and optical properties in a series of nanoparticle geometries, including

strongly coupling multi-nanoparticle systems, to demonstrate how the optical responses of a nanoparticle can be fine-tuned by judiciously tailoring the geometric parameters of the particle and how the tunable optical properties can be used to tackle grand challenges in diverse fields, such as photonics, energy conversion, spectroscopies, molecular sensing, and biomedicine.

3 Introduction

Nanoparticles exhibit a whole set of fascinating size- and shape-dependent physical and chemical properties that are dramatically different from those of either the corresponding bulk materials or the atomic and molecular systems [1]. Nanoparticles of noble metals, such as Au, Ag, and Cu, have attracted tremendous attention due to their interesting geometry-dependent optical properties. Actually, the vivid, beautiful color of colloidal metal nanoparticles has been an object of fascination since ancient times. One of the oldest examples is the famous Lycurgus Cup (Byzantine Empire, fourth century AD) (Fig. 1.1). This glass cup shows a striking red color when light is shone into the cup and transmitted through the glass, while viewed in reflected light, it appears green. This peculiar behavior is essentially due to the small Au–Ag bimetallic nanoparticles embedded in the glass, which show a strong optical absorption of light in the green part of the visible spectrum.

While these optical characteristics of metal colloids have been known and used for centuries, our scientific understanding on the origin of these properties has emerged far more recently, beginning with the development of classical electromagnetic theory. About a century ago, Gustav Mie applied Maxwell's equations to explain the strong absorption of green light by a Au nanosphere under plane wave illumination [2], which established, for the first time, the rigorous scientific foundation for our understanding of this interesting phenomenon. Essentially, the fascinating optically resonant behaviors of metal nanoparticles are determined by the collective oscillations of free electrons in the metals, known as plasmons. A plasmon resonance can be optically excited when a photon is absorbed at the metal–dielectric interface and transfers the energy into the collective electron oscillations, which are coupled in-phase with the incident light at a certain resonant frequency. For metal nanoparticles, the plasmon resonance frequencies are dependent upon the size and shape of the nanoparticles as the oscillations of free electrons are confined by the particle boundaries over finite nanoscale dimensions. It is well-known that solid spherical Au nanoparticles of ~30 nm in diameter strongly absorb green light at ~520 nm when their characteristic dipole plasmon resonance is optically excited, giving rise to a deep red color when dispersed in colloidal solutions. Michael Faraday was the first person to observe this spectacular phenomenon [3]. In 1857, he prepared the first stable suspension of Au colloids by reducing gold chloride with phosphorus in water. Some of his original samples are still well preserved and on display at the Faraday Museum in London.

The past two decades have witnessed rapid advances in the geometry-controlled fabrication of metallic nanostructures and electrodynamics simulation of the

Fig. 1.1 Pictures of the Lycurgus Cup (on display in the British Museum)

nanoparticles' optical properties, which allow for the development of quantitative understanding of the structure–property relationship of a series of metallic nanoparticle geometries with increasing structural complexity. It has become increasingly apparent that by adjusting the geometric parameters of metal nanostructures, one can fine-tune the wavelengths at which the nanoparticles interact with the incident light in a highly precise manner [1, 4–8]. The plasmon resonance frequencies of a metal nanoparticle are not only a function of the electronic properties of the constituent metal and the dielectric properties of the surrounding medium but also, especially on the nanometer-length scale, more sensitively dependent upon the size and shape of the particle. It is of paramount importance to create highly tunable plasmon resonances of nanoparticles over a broad spectral range because it can open a whole set of new opportunities for photonic, optoelectronic, spectroscopic, and biomedical applications. For example, expanding the plasmonic tunability of metallic nanoparticles from the visible into the near-infrared (NIR) "water window" where tissues and blood are relatively transparent provides unique opportunities for the integrated high-contrast cancer imaging and high-efficiency photothermal therapy [9, 10]. This has, in turn, stimulated tremendous interests in a rapidly expanding array of metal nanoparticle geometries, such as nanorods [11–16] nanoprisms [17–21], nanoshells [22–24] nanostars [25, 26], and nanocages [27, 28]. A key feature of these nanostructures is that their plasmon resonances are geometrically tunable, which enables one to set the plasmon resonances at a specific laser wavelength or spectral region that match a particular application.

In this chapter, we present a comprehensive review on the geometrically tunable optical properties of metal nanostructures. In Sect. 4, we give a brief introduction to the fundamentals of plasmon resonances supported by metal nanoparticles, covering both the experimental measurements and the theoretical methods for plasmon modeling. In Sect. 5, we start from the optical properties of the simplest geometry, solid metal nanospheres, to discuss how the free carrier density of the materials, the electronic properties of metals, and the size of spherical particles determine the

particles' overall optical properties. We also talk about the optical tunability of bimetallic heterostructured and alloy nanospheres. In Sects. 6 and 7, we focus on two representative nanoparticle geometries, nanorods and nanoshells, respectively, to demonstrate how various geometric parameters determine the plasmon-dominated optical properties of the nanoparticles with a particular focus on fundamental understanding of the origin of the optical tunability in these nanoparticle geometries. Essentially, the frequencies of plasmon resonances of metallic nanorods are determined by the aspect ratio of the nanorods, whereas the highly tunable nanoshell LSPRs arise from the interactions between the plasmon modes supported by the inner- and outer-shell surfaces. In Sect. 8, we give a brief survey of the structure–property relationships of several representative nanoparticle geometries with anisotropic structures, such as nanoprisms, nanopolyhedra, nanostars, and nanocages. In Sect. 9, we set out to talk about the geometrically tunable optical properties of more complicated multi-nanoparticle systems in which strong plasmon coupling occurs. We particularly emphasize on how the plasmonic interactions between nanoparticle building blocks give rise to the hybridized plasmon modes of the multiparticle systems and further enhanced local fields in the interparticle junctions that are exploitable for surface-enhanced spectroscopies. Finally, in Sect. 10, we summarize the latest progress in nanoparticle plasmonics over the past two decades and briefly comment on how the geometrically tunable LSPRs of metal nanoparticle systems will broadly impact the fundamental research on nanophotonics and technological applications of metal nanostructures.

4 Localized Surface Plasmon Resonances (LSPRs)

4.1 Plasmons: Collective Oscillations of Free Electrons

Early understanding of the theory of nanoparticle plasmons dates back to the work done by Mie [2] and Faraday [3] more than a century ago. In this chapter, it is not intended to thoroughly cover the plasmon theories in detail, since a good number of excellent reviews, such as the books by Kreibig and Vollmer [29] and by Bohren and Huffman [30] as well as review articles by Mulvaney [31] and by El-Sayed [5], have already been published on this topic, and the readers are encouraged to read them for further details. Here we only want to give a brief introduction to the fundamentals of plasmon resonances of metal nanoparticles.

Essentially, plasmons arise from the collective oscillations of free electrons in metallic materials. Under the irradiation of an electromagnetic wave, the free electrons are driven by the electric field to coherently oscillate at a plasmon frequency of ω_B relative to the lattice of positive ions [29]. For a bulk metal with infinite sizes in three dimensions in vacuum, ω_B can be expressed as

$$\omega_B = \sqrt{\frac{4\pi e^2 n}{me}} \tag{1.1}$$

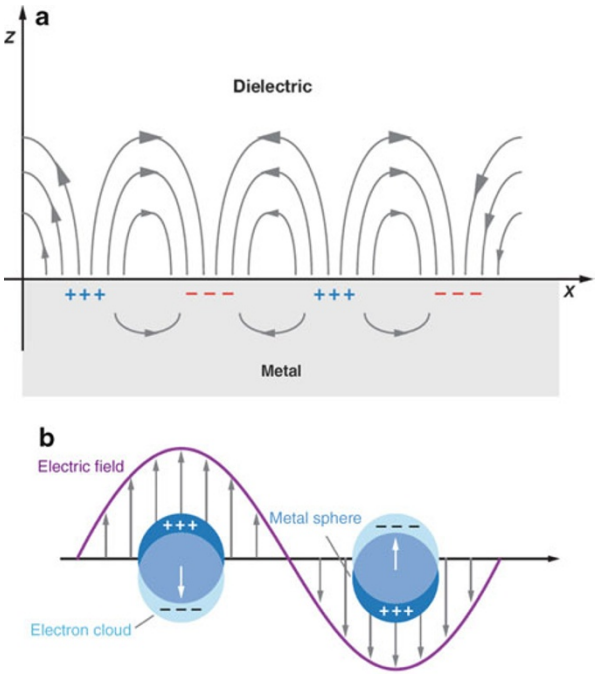

Fig. 1.2 Schematic illustrations of (**a**) a propagating plasmon at metal–dielectric interface and (**b**) a LSPR of a metal nanosphere (Adapted with permission from Ref. [33]. Copyright 2007 Annual Reviews)

where n is the number density of electrons and e and m_e are the charge and effective mass of electrons, respectively.

However, in reality, we have to deal with metallic structures of finite dimensions that are surrounded by materials with different dielectric properties. Since an electromagnetic wave impinging on a metal surface only has a certain penetration depth (~50 nm for Ag and Au), only the electrons on the surface are the most significant. Therefore, their collective oscillations are properly termed as surface plasmons [32]. At a metal–vacuum interface, application of the boundary conditions results in a surface plasmon mode with a frequency $\omega_{surf} = \frac{\omega_p}{\sqrt{2}}$. As is shown in Fig. 1.2a, such a surface plasmon mode represents a longitudinal charge density wave that travels across the surface [33], also widely known as a propagating plasmon. A surface plasmon mode can be excited through a resonance mechanism by passing an electron through a thin metallic film or by reflecting an electron or a photon from the surface of a metallic film when the frequency and wave vectors of both the incident light and the surface plasmon match each other.

In metallic nanoparticle systems, the collective oscillations of free electrons are confined to a finite volume defined by the particle dimensions. Since the plasmons of nanoparticles are localized rather than propagating, they are known as localized surface plasmon resonances (LSPRs). When the free electrons in a metallic nanostructure are driven by the incident electric field to collectively oscillate at a certain resonant frequency, the incident light is absorbed by the nanoparticles. Some of these photons will be released with the same frequency and energy in all directions,

which is known as the process of scattering. Meanwhile, some of these photons will be converted into phonons or vibrations of the lattice, which is referred to as absorption [30]. Therefore, LSPRs manifest themselves as a combined effect of scattering and absorption in the optical extinction spectra. As depicted in Fig. 1.2b, the free electrons of Au nanospheres oscillate coherently in response to the electric field of incident light [33]. The multipolar resonant frequencies can be represented as $\omega_{S.l} = \omega_B \sqrt{\frac{l}{2l+1}}$ (l = 1, 2, 3, 4. . .) when this process occurs in a vacuum. It has been known that the number, location, and intensity of LSPR peaks of Au or Ag nanoparticles are strongly correlated with both the shape and size of the nanoparticles.

4.2 Experimental Methodology of LSPR Measurements

There are generally two important effects associated with the excitation of LSPRs, the existence of optical extinction maxima at the plasmon resonance frequencies (far-field properties) and significantly enhanced electric fields in close proximity to the particle's surface (near-field properties). The far-field plasmonic properties of metal nanoparticles can be most conveniently measured by performing extinction spectroscopy measurements on colloidal nanoparticle suspensions or on thin films of nanoparticles immobilized on or embedded in a substrate at ensemble level using UV–visible–NIR spectrometers. In these measurements, both absorption and scattering contribute to the overall extinction. The polydispersity of the samples may introduce inhomogeneous broadening to the overall bandwidth and modify the line shape of the extinction spectra. To bypass the ensemble-averaging effects, one can use a dark-field microscope coupled with a spectrometer to probe the wavelength-dependent light-scattering properties of individual nanoparticles at single-particle level. Figure 1.3 shows a dark-field microscopy image of Au nanoparticles of different geometries and the corresponding scattering spectra of each individual nanoparticle [34]. The different nanoparticles exhibit dramatically different colors and intensities in the microscopy images and are resonant with the incident light at different wavelengths. By adding linear polarizers and other optical accessories to the dark-field microscope, the spatial distribution of the scattering light at a certain wavelength can be measured. By correlating the optical characteristics probed by dark-field microscopy with the detailed structural information obtained from electron microscopies at single-particle level, one can develop quantitative understanding of the structure–property relationship of individual nanoparticles without the ensemble-averaging effects. Since the electrodynamics simulations are mostly carried out on individual nanoparticles, the single-particle measurements provide unique opportunities to directly compare the experimental spectra to the simulated results.

In addition to the abovementioned far-field measurements, near-field scanning optical microscopy (NSOM) has been applied to the near-field measurements of LSPRs. NSOM is a powerful imaging tool which permits super-resolution imaging of samples through the interaction of the light with the samples close to the metal

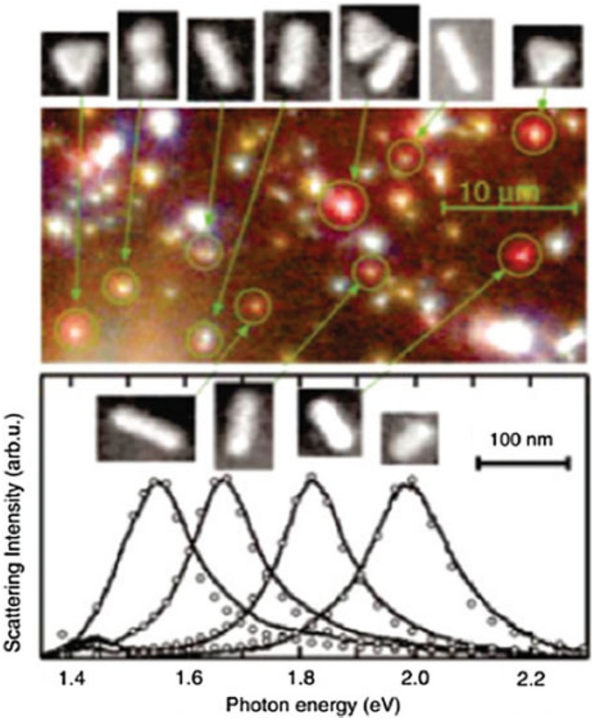

Fig. 1.3 Dark-field microscopy image, corresponding scanning electron microscopy images, and light-scattering spectra of Au nanocrystals of different shapes (Reprinted with permission from Ref. [34]. Copyright 2003 American Institute of Physics)

aperture, breaking the diffraction barrier of light [35–38]. However, for conventional aperture-type NSOM, the resolution is limited by the aperture size of the tip. Since the effective transmission area decreases as the fourth power of the aperture diameter [39, 40], the resolution improvement comes at the price of a sharp decrease in signal-to-noise ratio and contrast of NSOM images. Recently, differential near-field scanning optical microscopy (DNSOM) is introduced to improve the light transmission, which involves scanning a rectangular (e.g., a square) aperture (or a detector) in the near-field of the object of interest and recording the power of the light collected from the rectangular structure as a function of the scanning position [41].

Electron energy loss spectroscopy (EELS) is another powerful method for near-field mapping of LSPRs. When a material is exposed to a beam of electrons with a narrow range of kinetic energies, the constituent atoms can interact with these electrons via electrostatic (Coulomb) forces, resulting in elastic and inelastic scattering of electrons. Among them, inelastic scattering is associated with the energy loss of electrons, which can be measured via an electron spectrometer and interpreted in terms of what caused the energy loss [42]. EELS is a very powerful probe for the excitation on the surface and ultrathin films, in particular, for the collective excitations of electron oscillations (plasmons). Plasmon excitations are directly related to the band structure and electron density in a small volume of the particle probed by the focused electron beam [43]. With the recent proliferation of

aberration-corrected and monochromated transmission electron microscopes (TEMs), mapping the energy and spatial distribution of metallic nanoparticle plasmon modes on nanometer-length scales using EELS has become possible [44–47]. For example, Liz-Marzan and coworkers utilized a novel method relied on the detection of plasmons as resonance peaks in EELS to record maps of plasmons with sufficiently high resolution to reveal the dramatic spatial field variation over silver nanotriangles [48]. The near-field plasmon modes of isolated and coupled Au nanorods have also been imaged using EELS and energy-filtered transmission electron microscope (EFTEM) [49]. More recently, plasmon mapping of a series of high-aspect-ratio Ag nanorods using EELS was also reported [50]. These data indicate that correlated studies will ultimately provide a unified picture of optical and electron beam-excited plasmons and reinforce the notion that plasmon maps derived from EELS have direct relevance for the plethora of processes relying on optical excitation of plasmons.

The local field enhancements on the surface of nanoparticles arising from plasmonic excitations can also be indirectly probed by surface-enhanced spectroscopies. For example, the local field enhancements provide well-defined "hot spots" for surface-enhanced Raman scattering (SERS) [51–54]. Once the molecules get into these hot regions in vicinity to a metallic nanostructure, their spectroscopic signals can be dramatically amplified. It has been demonstrated that SERS enhancements are dependent on the fourth power of the local field enhancements. Therefore, the Raman enhancements of the probing molecules in close proximity to a metal nanostructure provide a way to evaluate the local field enhancements. Since Raman enhancements are sensitively dependent on the distance between molecules and metal surfaces, one can smartly construct molecular rulers to map out the local field enhancement profiles surrounding a nanoparticle based on SERS [55].

4.3 Simulations of LSPRs

The most commonly used theoretical methods for the modeling of the LSPRs of metallic nanoparticles include both analytical and numerical methods [56–59]. The analytical methods are either derived from Mie scattering theory for spheres or from the quasi-static (Gans) model as applied to spheroids. Most popular numerical methods for electrodynamics simulations include the discrete dipole approximation (DDA), the finite-difference time-domain (FDTD) method, the finite element method (FEM), and boundary element method (BEM).

It was realized almost a century ago that classical electromagnetic theory (i.e., solving Maxwell's equations for light interacting with a particle) based on Mie scattering theory provides a quantitative description of the scattering and absorption spectra of spherical nanoparticles. However, Mie's work is incapable of addressing shape effects. Although the quasi-static approximation developed later is an alternative to elucidate the optical properties of spheroids, the solution is even harder to use because of frequency-dependent dielectric functions included in Maxwell's

equations. Meanwhile, the numerical methods for solving Maxwell's equations come in many different flavors. For example, the discrete dipole approximation (DDA) is a frequency domain approach that approximates the induced polarization in a complex particle by the response of a cubic grid of polarizable dipoles. The finite different time domain (FDTD) method can be applied in both two and three dimensions, in which a clever finite differencing algorithm is applied to Maxwell's equation by Yee [60], using grids for the electric field **E** and magnetic field **H**, which are shifted by half a grid spacing relative to each other. Using the finite element method (FEM), the solutions to Maxwell's equations are expanded in locally defined basis functions chosen such that boundary conditions are satisfied on the surfaces of the elements. Boundary element method (BEM) is another numerical computational method of solving linear partial differential equations which have been formulated as integral equations. These numerical methods have been shown to be capable of simulating both the far-field and near-field plasmonic properties of metallic nanostructures of almost arbitrary structural complexity.

In addition to the analytical and numerical methods mentioned above, the time-dependent density functional theory (TDDFT) is one of the most convenient approaches for the fully quantum mechanical calculations of the optical properties of metallic nanoparticles [61–63]. TDDFT, an extension of density functional theory (DFT) with conceptual and computational foundations analogous to DFT, is to use the time-dependent electronic density instead of time-dependent wave function to derive the effective potential of a fictitious noninteracting system which returns the same density as any given interacting system.

Combined experimental and theoretical efforts over the past two decades have shed light on the interesting geometry dependence of plasmonic properties of metallic nanoparticles with increasing geometric complexity. In the following section, before moving onto those more complicated nanoparticle geometries, we will start from the simplest geometry, a nanosphere, to demonstrate how the LSPRs can be systematically tuned by changing the compositional and geometric parameters of the nanosphere.

5 LSPRs of Metallic Nanospheres

5.1 LSPRs of Single-Component Nanospheres

Strong optical scattering and absorption of light by noble metal nanospheres in visible spectral region due to LSPRs are a classical electromagnetic effect, which was described theoretically by Mie in 1908 by solving Maxwell's equations. Mie's theory is most useful in describing the plasmonic properties of metallic particles that are spherically symmetric. Mie scattering theory is the exact solution to Maxwell's electromagnetic-field equations for a plane wave interacting with a homogeneous sphere of radius R with the same dielectric constant as bulk metal. The extinction cross section of the spheres can be obtained as a series of multipolar oscillations if the boundary conditions are specified. Therefore, the

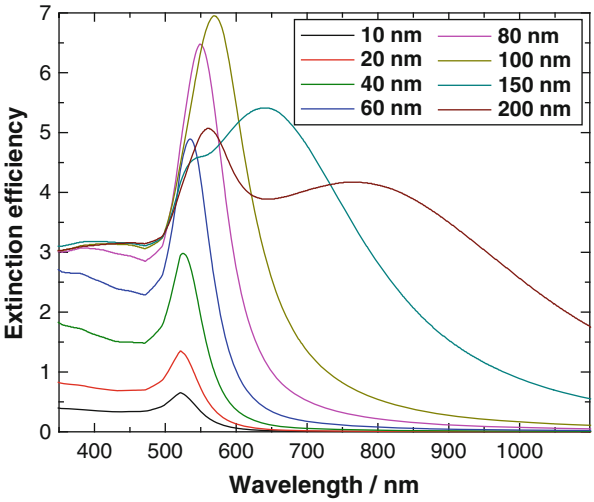

Fig. 1.4 Extinction spectra calculated using Mie scattering theory for Au nanospheres with diameters ranging from 10 nm to 200 nm dispersed in water. The calculated extinction is expressed as an efficiency, which is the ratio of the energy scattered or absorbed by the particle to the energy incident on its physical cross section

electrodynamics calculations can be simplified by only focusing upon low-order plasmon oscillations when the diameter of the spherical particle is much smaller than the wavelength of the radiation (within the quasi-static limit) and only dipole oscillation ($l = 1$) contributes to the extinction cross section which is a sum of both scattering and absorption. Based on this, the most popular form of Mie's theory for spherical nanoparticles within quasi-static limit is given as

$$C_{ext} = \frac{24\pi^2 R^3 {\varepsilon_m}^{3/2}}{\lambda} \bullet \frac{\varepsilon_2}{(\varepsilon_1 + 2\varepsilon_m)^2 + {\varepsilon_2}^2} \tag{1.2}$$

where C_{ext} is the extinction cross section of the spheres, ε_m is the dielectric constant of the surrounding medium, λ is the wavelength of the radiation, R is the radius of a homogeneous sphere, and ε_1 and ε_2 denote the real and imaginary part of the complex dielectric function of the particle material, respectively. A resonance occurs whenever the condition of $\varepsilon_1 = -2\varepsilon_m$ is satisfied, which explains the dependence of the LSPR extinction peak on the surrounding dielectric environment. It is this LSPR peak that accounts for the brilliant colors of a wide variety of metallic nanoparticles. The imaginary part of the dielectric function also plays a role in the plasmon resonance, relating to the damping, that is, resonance peak broadening in the spectrum.

For a small Au nanosphere within the quasi-static limit, its LSPR has an almost fixed resonance frequency and shows limited tunability. As shown in Fig. 1.4, the extinction spectra calculated using Mie theory for Au nanospheres smaller than 100 nm show that LSPR peaks are located in the green part of the visible region. According to the full Mie-theory solution, a limited red shift of LSPR wavelength and broadening of the resonant line shape appear as Au nanospheres progressively become larger within the sub-100-nm-size regime. As the particle size further

increases to the size regime beyond the quasi-static limit, the overall spectral line shape becomes more complicated as the higher-order multipolar resonances, such as quadrupole ($l = 2$) and octupole ($l = 3$), become increasingly significant in the extinction spectra in addition to the dipolar plasmon resonances due to the phase-retardation effects, resulting in further redshifted and broadened dipolar plasmon bands. Such size dependence of LSPRs has been experimentally observed to be in very good agreement with Mie scattering theory calculations for Au and Ag spherical or quasi-spherical particles over a broad size range both within and beyond the quasi-static limit [64, 65].

5.2 Effects of Materials' Electronic Properties on LSPRs of Nanospheres

In addition to the particle size, the frequencies of LSPRs of a nanosphere also rely on the electronic properties of the constituent materials. The LSPR frequency, although tunable by varying the nanoparticle size and local medium, is primarily controlled through the free electron density (N) of the material. Although LSPRs typically arise in nanostructures of noble metals, they are not fundamentally limited to noble metals and can also occur in other non-noble metals, conducting metal oxides and semiconductors with appreciable free carrier densities. Recently, Alivisatos and coworkers demonstrated that in analogy to noble metal nanoparticles, doped semiconductor quantum dots may also exhibit LSPRs whose resonance frequencies can be tuned by controlling the free carrier densities of the materials [66]. Figure 1.5 depicts the modulation of the LSPR frequency (ω_{sp}) of a spherical nanoparticle within the quasi-static limit through control over its free carrier concentration (N). In this figure, the LSPR frequency can be estimated using the following equation:

$$\omega_{SP} = \frac{1}{2\pi}\sqrt{\frac{Ne^2}{\varepsilon_0 m_e(\varepsilon_\infty + 2\varepsilon_m)}} \tag{1.3}$$

Here the high frequency dielectric constant (ε_∞) is assumed to be 10, the medium dielectric constant ε_m is set as 2.25 for toluene, and the effective mass of the free carrier m_e is assumed to be that of a free electron. e is the electronic charge, and ε_0 is the permittivity of free space. The top panel shows a calculation of the number of dopant atoms required for nanoparticle sizes ranging from 2 to 12 nm to achieve a free carrier density between 10^{17} and 10^{23} cm^{-3}. To achieve LSPRs in the visible region, a metallic material in which every atom contributes a free carrier to the nanoparticle is required. For LSPRs in the infrared, carrier densities of 10^{19}–10^{22} cm^{-3} are required. Below 10^{19} cm^{-3}, the number of carriers (for a 10-nm nanocrystal) may be too low (<10) to support an LSPR mode.

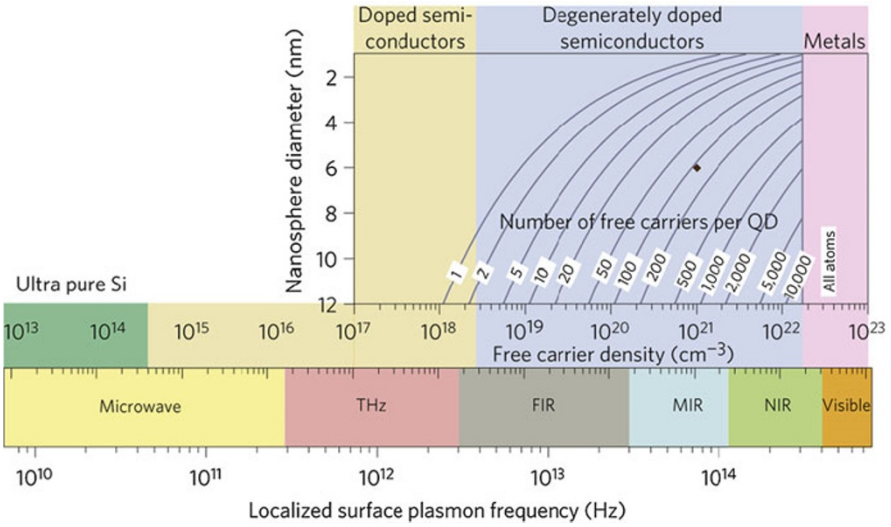

Fig. 1.5 LSPR frequency dependence on free carrier density and doping constraints (Reprinted with permission from Ref. [66]. Copyright 2011 Nature Publishing Groups)

The most commonly studied plasmonic materials so far are noble metals, such as Au, Ag, and Cu, which have free electron densities in the range of 10^{22}–10^{23} cm^{-3} with corresponding LSPRs in the visible. For non-noble metals, such as Pb, In, Hg, Sn, Cd, and Al, their LSPR frequencies lie in the UV region of the spectrum, and nanoparticles do not display well-defined LSPR bands that are as tunable as those of the noble metals. In addition, small particles of these non-noble metals are also chemically unstable and readily oxidized, making it difficult to measure their LSPRs. The LSPRs of doped semiconductor nanoparticles typically occur in the infrared and are not as strong and well-defined as those of noble metal nanoparticles. The geometry dependence of LSPRs of doped semiconductor nanoparticles is still poorly understood at the present stage. Therefore, we will only focus on the plasmonic properties of noble metal nanoparticles, Au and Ag nanoparticles in particular, because of not only their relatively high chemical and photostability but also more importantly their intense and geometrically tunable LSPRs across the visible and NIR regions.

In addition to the free electron densities of the materials, the optical properties of noble metal nanospheres are also strongly influenced by the electronic band structures of the constituent metal, which determine the metal's dielectric functions. The complex dielectric function of a material, denoted as $\varepsilon = \varepsilon_1 + i\varepsilon_2$, describes a material's response to an applied electric field. ε_1 determines the degree to which the material polarizes in response to an applied field, while ε_2 controls the relative phase of this response with respect to the applied field. Intrinsic loss mechanisms (e.g., electron scattering) of a material are all

condensed into ε_2. For the noble metals at optical frequencies, the dielectric function can be expressed as the sum

$$\varepsilon(m) = 1 + \chi_\infty + \chi_D(\omega) \tag{1.4}$$

where the background susceptibility χ_∞ arises from the core electron polarizability and interband (d → sp) transitions and χ_D is the Drude response of the conduction electrons. The background polarizability and free space response are often combined into $\varepsilon_\infty = 1 + \chi_\infty$ In the Drude model [30],

$$\chi_D(\omega) = -\frac{\omega_P^2}{\omega^2 + i\Gamma\omega} = -\frac{\omega_p^2}{\omega^2 + \Gamma^2} + i\frac{\omega_p^2\Gamma}{\omega(\omega^2 + \Gamma^2)} \tag{1.5}$$

where ω_P is the bulk plasmon frequency and Γ is the reciprocal electron relaxation time. In the visible and NIR, $\Gamma << \omega$; therefore,

$$\chi_D(\omega) \cong -\frac{\omega_P^2}{\omega^2} + i\frac{\omega_p^2}{\omega^3}\Gamma \tag{1.6}$$

To completely understand the role that the metal plays in determining the optical properties of metallic nanoparticles, it is necessary to examine and account for the effects of both the free-electron and electronic interband transition contributions to the metal's dielectric response. Figure 1.6 shows a comparison of dielectric functions of Ag, Au, and Cu, together with the calculated extinction spectra of Au, Ag, and Cu nanospheres that are 30 nm in diameter obtained using Mie scattering theory. The dielectric medium surrounding the nanoparticles is water. The spectral regions where interband transitions occur are shaded in green. The onset of electronic interband transitions from the valence band to the Fermi level causes a sharp increase in the imaginary part (ε_2) and a marked change in the slope of the real part (ε_1) of the dielectric functions. For 30-nm-diameter solid nanospheres, the relative spectral locations of the particle plasmon resonance and the constituent metal's interband transitions determine the nanoparticles' optical response, resulting in significant variations between Au, Ag, and Cu nanospheres. The Ag nanosphere has by far the strongest plasmon resonance because of the higher energy of the interband transitions (~3.8 eV), relative to the energy of the plasmon resonance, resulting in minimal damping of the plasmon. The Au nanosphere displays a well-defined plasmon resonance at ~520 nm, which is closer to the edge of the interband transitions region (~2.5 eV) than the case of Ag. With plasmon resonant energies well below the interband transitions, Au and Ag nanoparticles can be treated as free-electron systems whose optical properties are determined by the conduction electrons, with only a constant real background polarizability associated with the core electrons. The Cu nanosphere, however, has much weaker optical response in comparison to Ag and Au due to the nanosphere plasmon being resonant with the interband transition region (~2.1 eV)

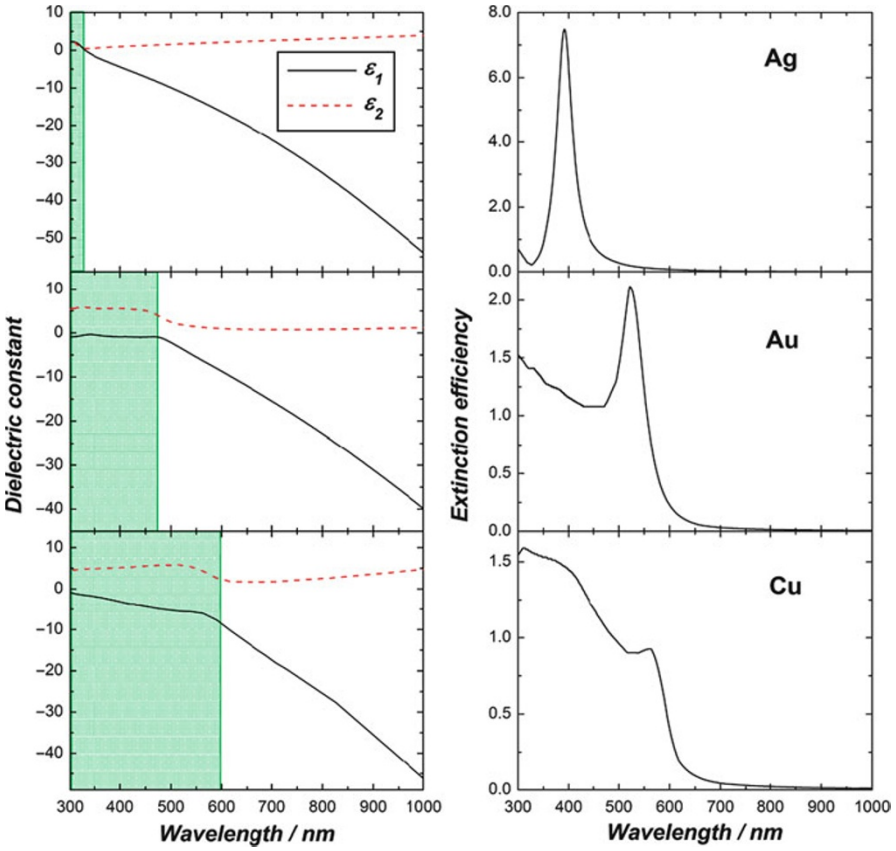

Fig. 1.6 Dielectric functions (*left column*) and calculated extinction spectra of a 30-nm-diameter nanosphere (*right column*) of Ag (*top*), Au (*middle*), and Cu (*bottom*)

of the spectrum. The interband transitions are responsible for a strong damping of the Cu nanosphere plasmon and the strong "background" absorption on top of which a weak plasmon resonance peak is visible.

5.3 Bimetallic Nanospheres

When multiple metallic components are integrated into one nanosphere, the resulting optical properties become dependent upon both the compositions and the compositional distribution inside the nanoparticle. Although various bimetallic nanoparticle systems have been studied, combinations of Au and Ag are of particularly interest largely for two reasons. First, both metals display intense and well-defined LSPR bands in the visible at around 400 and 520 nm for spherical nanoparticles of Ag and Au, respectively. Second, both Au and Ag form

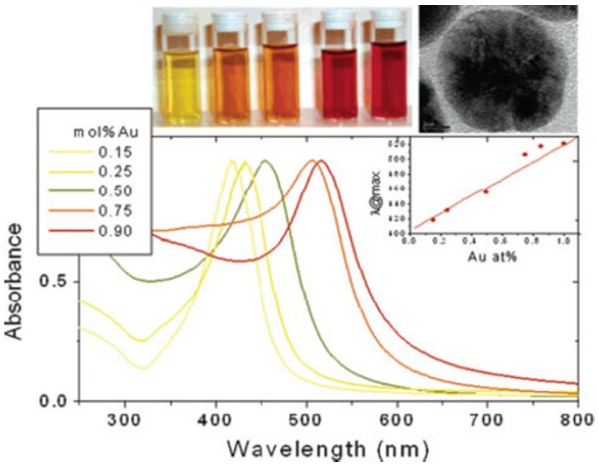

Fig. 1.7 UV–visible spectra of Au–Ag alloy nanoparticle colloids with varying compositions. A linear fit of the peak position of the experimental absorption band as a function of composition obtained using Mie theory is plotted (*inset*). HRTEM image shows the homogeneous distribution of Au and Ag atoms within the particles (Reprinted with permission from Ref. [80]. Copyright 2006 American Chemical Society)

face-centered cubic crystalline structures with very small lattice mismatch (lattice constants of 4.078 Å and 4.086 Å for Au and Ag, respectively), and therefore, they can form heteronanostructures through epitaxy growth or form alloy nanostructures with various compositional stoichiometries. Spherical nanoparticles of Au–Ag alloy [67–73], Au–Ag core–shell [74–78], and Ag–Au core–shell [74, 79] have been fabricated through various bottom-up chemistry approaches. Precise control over both the compositional stoichiometry and distribution enables one to systematically study the interesting optical tunability of bimetallic nanospheres.

For alloy nanospheres normally prepared by simultaneous reduction of the metal salts, it has been observed that the plasmon band of the alloy nanoparticles lies somewhere between those for pure Ag and pure Au nanoparticles [70, 71], and there is a linear relationship between the compositional stoichiometry and the wavelength of the plasmon band of the alloy particles. As shown in Fig. 1.7, a continuous color evolution from yellow to red can be clearly observed as the Au to Ag ratio progressively increases [80]. As shown in the inset plots of Fig. 1.7, the experimentally observed linear relationship between compositional stoichiometry and LSPR wavelength can be well reproduced by Mie scattering theory calculations. The LSPR shifts were initially modeled by assuming a linear combination of the dielectric functions of pure Au and Ag as input for the Mie scattering theory calculations, but El-Sayed and coworkers have demonstrated that the theoretical predictions agreed with the experimental results more accurately when experimentally measured dielectric functions for Au–Ag alloy films were used. The linear relationship between compositional stoichiometry and wavelength of LSPR band applies to alloy nanoparticles only and cannot be simply extended to core–shell heterostructured nanoparticles.

Core–shell heterostructured bimetallic nanoparticles can be fabricated either via segregation during simultaneous reduction or by successive reduction of the

different metals [68, 81, 82]. Recently, the creation of onion-like multilayer bimetallic nanoparticles obtained by successive reduction of $AgNO_3$ and $HAuCl_4$ with ascorbic acid in the presence of cetyltrimethylammonium bromide (CTAB) has been reported. The optical properties of these core–shell bimetallic nanoparticles are quite sensitive to the multilayer deposition, and the extinction spectral line shape are mostly dominated by the geometry of the outermost layer [83]. It is interesting that the core–shell heterostructured bimetallic nanoparticles may undergo alloying processes under appropriate conditions. For Au–Ag bimetallic nanoparticles, the core–shell heterostructures may be kinetically favorable during the particle formation, while the alloy particles are thermodynamically more stable. Therefore, the transitions from the core–shell heterostructures to alloy homostructures are in principle spontaneous at room temperature. By modifying the experimental conditions, such transitions may be accelerated and kinetically better controlled. For example, Hartland and coworkers [75] used nanosecond and picosecond lasers to melt the Au–Ag core–shell particles into homogeneously alloyed nanoparticles. Sun and coworkers [79] reported the formation of monodisperse Au–Ag alloy nanoparticles through interface diffusion of Ag–Au core–shell nanoparticles under solvothermal conditions in organic solvents. Recently, Tracy and coworkers [84] reported a facile method for the synthesis of Au–Ag core–shell nanoparticles and their subsequent transition to Au–Ag alloy nanoparticles through digestive ripening. By controlling the relative sizes of the Au core and Ag shell, the stoichiometry of the resulting Au–Ag alloy nanoparticles can be precisely controlled. The structural change of the particles during the alloying processes can be monitored through the shift of the LSPR bands. Precise control over the particle's geometry and compositions is important to the fine-tuning of the optical properties of the bimetallic nanoparticles as their LSPRs are sensitively dependent on both the stoichiometry and geometrical distribution of the metal compositions.

6 LSPRs of Metallic Nanorods

6.1 Geometrically Tunable LSPRs of Nanorods

Metal nanorods are elongated, anisotropic nanoparticles with polarization-dependent response to the incident light. The excitation of the electron oscillation along the short axis induces a plasmon band at wavelength similar to that of Au nanospheres, commonly referred to as the transverse band. The excitation of the electron oscillation along the long axis induces a much stronger plasmon band in the longer wavelength region, referred to as the longitudinal band. When Au nanorods are dispersed in a solvent, a steady-state extinction spectrum containing both bands of longitudinal and transverse plasmons can be observed due to the random orientation caused by the continuous Brownian motion of the particles. While the transverse band is insensitive to the size of the nanorods, the longitudinal band is redshifted significantly from the visible to NIR region with increasing aspect ratio (length/width) [85–87].

Because of the nonspherical shape, the plasmonic properties of nanorods cannot be fully described by Mie scattering theory. However, qualitative features of nanorod LSPRs are well reproduced by Gans theory [88] which is an extension of Mie theory for ellipsoidal nanoparticles. Gans theory puts depolarization factors for each direction in the Mie-theory expression to capture the optical anisotropy. In 1912, Gans predicted that for very small ellipsoids, where the dipole approximation holds, the plasmon mode would split into two distinct modes [88]. In Gans theory, the LSPRs are only dependent on the aspect ratio of the particles but not on the absolute dimensions. Gans theory gives the exact solution to Maxwell equations for ellipsoidal particles. The experimentally fabricated nanorods, however, are more like cylinders or sphere-capped cylinders than ellipsoids. Using numerical methods, such as DDA, one can more accurately model the exact shape of the particles. Nevertheless, Gans theory calculations match the experimental data adequately well in most cases and can further shed light on the origin of the geometry–property relationship of nanorods. To interpret the optical properties of small metal nanorods using Gans formula, it has been common to treat them as ellipsoids [11, 89].

The cross sections of absorption (C_{abs}), scattering (C_{csa}), and total extinction (C_{ext}) derived from Gans theory can be quantitative described by the following equations:

$$C_{abs} = \frac{2\pi}{3\lambda}\varepsilon_m^{3/2} V \sum_i \frac{\varepsilon_2/\left(n^{(i)}\right)^2}{\left(\varepsilon_1 + [(1-n^{(i)})/n^{(i)}]\varepsilon_m\right)^2 + \varepsilon_2^2} \tag{1.7}$$

$$C_{sca} = \frac{8\pi^3}{9\lambda^4}\varepsilon_m^2 V^2 \sum_i \frac{\left(\varepsilon_1 - \varepsilon_m\right)^2 + \varepsilon_2^2/\left(n^{(i)}\right)^2}{\left(\varepsilon_1 + [(1-n^{(i)}/n^{(i)}]\varepsilon_m\right)^2 + \varepsilon_2^2} \tag{1.8}$$

$$C_{ext} = C_{abs} + C_{sca} \tag{1.9}$$

where λ is the wavelength of light, V is the unit volume of the nanoparticle, and $n^{(i)}$ is the depolarization factor defined by:

$$n^{(a)} = \frac{2}{R^2-1}\left(\frac{R}{2\sqrt{R^2-1}} \ln\frac{R+\sqrt{R^2-1}}{R-\sqrt{R^2-1}} - 1\right) \tag{1.10}$$

$$n^{(b)} = n^{(c)} = (1-n^{(a)})/2 \tag{1.11}$$

where a, b, and c are the three axes of the nanoparticle, $a > b = c$, and aspect ratio, R is equivalent to a/b or a/c. The LSPRs of an ellipsoidal particle occur when the following equation applies:

$$\varepsilon_1 = -(1-n^{(i)}) \times \varepsilon_m/n^{(i)} \tag{1.12}$$

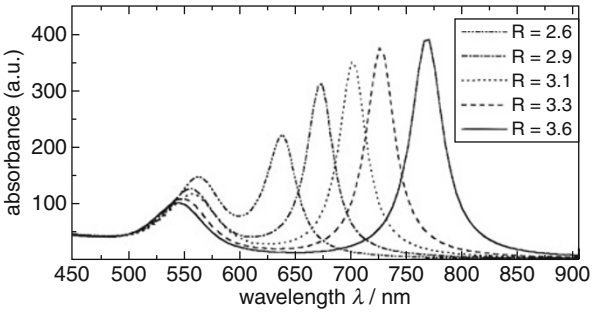

Fig. 1.8 Calculated extinction spectra of elongated Au ellipsoids with varying aspect ratio R using Gans theory (Reprinted with permission from Ref. [11]. Copyright 1999 American Chemical Society)

where $i = a$ for the longitudinal resonance and $i = b$ or c for the transverse resonance. At such resonance wavelengths, the absorption, scattering, and total extinction are all strongly enhanced, giving rise to the extinction peaks in the extinction spectra.

Gans equation predicts that for small ellipsoids embedded in the same medium, an almost linear correlation exists between longitudinal LSPR wavelength and aspect ratio of the ellipsoids. Figure 1.8 shows the calculated extinction spectra of nanorods with different aspect ratios. The longitudinal plasmon band is continuously shifted from the visible to NIR as the aspect ratio of the nanorods increases [11], while the transverse plasmon band exhibits a slight blue shift as aspect ratio increases.

In addition to aspect ratio, the longitudinal plasmon resonance frequency of metal nanorods is also sensitively dependent on the dielectric properties of the local environment. Figure 1.9 shows the calculated spectra of ellipsoidal Au nanoparticles with a fixed aspect ratio of 3.5 in dielectric media with varying refractive indices. As the refractive index of the surrounding medium increases, the longitudinal plasmon band progressively shifts to longer wavelength, exhibiting greatly enhanced sensitivity toward dielectric perturbations in comparison to Au nanospheres [87]. It has also been observed that the larger aspect ratio of the nanorod is, the greater the sensitivity to refractive index effects the nanorod has. Therefore, a single nanorod may serve as a nanoscale sensor that can be used to probe the local environment changes surrounding the particle based on the shift of its LSPR.

In comparison to metal nanospheres, nanorods exhibit greatly enhanced LSPR tunability over a much broader spectral range. In addition, metallic nanorods have further enhanced electric fields at the tips compared to nanospheres, which is crucial to the achievement of larger signal enhancements in surface-enhanced spectroscopies, such as SERS. As calculated by using classical electromagnetic theory and TDDFT, the maximum field enhancement is more pronounced for more elongated nanorods compared to ones with smaller aspect ratios (Fig. 1.10) [90]. Although the values of maximum field enhancement of nanorods with different aspect ratios are somewhat different, the spatial distributions of the field enhancements are similar for both TDDFT and classical calculations.

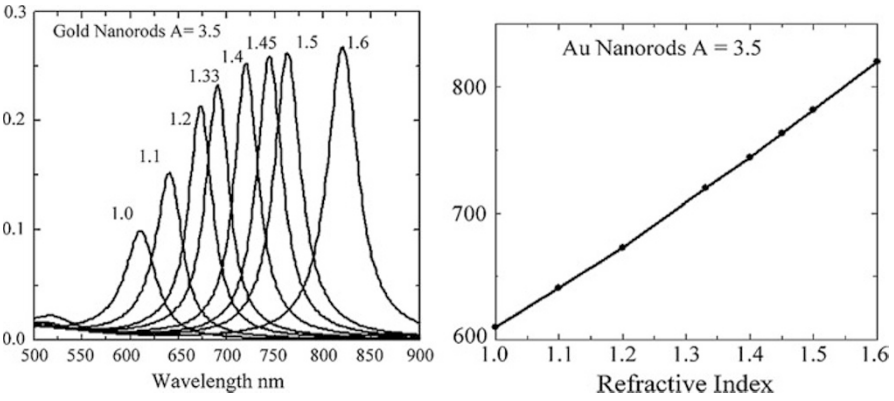

Fig. 1.9 Calculated spectra for Au ellipsoids with an aspect ratio of 3.5 in different media (*left*) and the LSPR band position as a function of the medium refractive index (*right*) (Reprinted with permission from Ref. [87]. Copyright 2005 Elsevier B. V.)

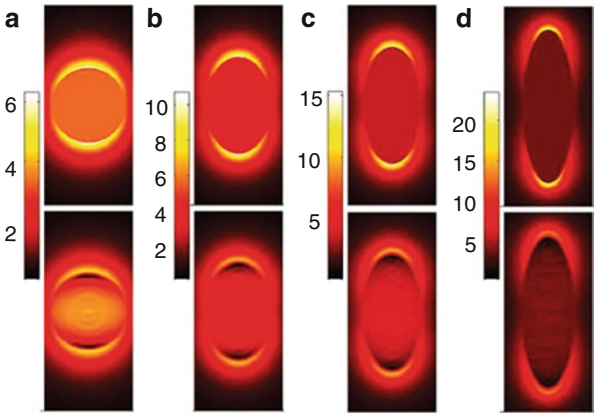

Fig. 1.10 Comparisons of the field distributions calculated using classical electromagnetic theory (*top panels*) and TDDFT (*bottom panels*) for aspect ratios of 1 (**a**), 1.5 (**b**), 2 (**c**), and 3 (**d**), respectively (Reprinted with permission from Ref. [90]. Copyright 2010 American Chemical Society)

6.2 Controllable Fabrication of Nanorods

Although the synthesis of spherical Au nanoparticles has a history of more than a century since the pioneering work by Faraday in 1857 [3], methods for the fabrication of colloidal Au nanorods with well-controlled aspect ratios emerged only during the past two decades. The controllability over the size and morphology enables us to experimentally study the geometrically tunable optical properties of metallic nanorods. Although there are successful examples of controllable fabrication of Ag and Cu nanorods [91–93], the fabrication of Au nanorods has received much more success with much better controllability over the yield, aspect ratio, and

uniformity of the samples. Here we give a brief outline of various synthetic approaches, including both bottom-up and top-down techniques, for the geometry-controlled fabrication of Au nanorods.

The template method for the synthesis of Au nanorods, first developed by Martin and coworkers [94], involves the electrochemical deposition of Au within the pores of nanoporous template membranes. Using this method, the diameter of the Au nanorods roughly equals to the pore diameter of the template membrane, which can be controlled during the membrane fabrication process. The length of the nanorods can be controlled by controlling the amount of Au deposited within the pores during the electrodeposition. More complicated one-dimensional metallic nanostructures, such as Au nanotubes, multicomponent coaxial nanocables, and bar-code heterojunction structures, can also be fabricated using this method [95].

In 1990s, Wang and coworkers developed an electrochemical method for the fabrication of Au nanorods with high yield [89, 96]. In this method, a metallic Au plate anode and a Pt plate cathode are immersed in an electrolytic solution containing a structural directing agent, CTAB, and a cosurfactant tetradodecylammonium bromide (TOAB). During the electrolysis, the bulk Au anode is consumed, forming $AuBr_4^-$ which are then complexed to the cationic surfactants, and migrates to the cathode where Au ions are reduced to metallic Au. A Ag plate is gradually inserted into the solution to control the aspect ratio of the nanorods. Sonication is needed to dissipate the nanorods away from the cathode to form free-standing colloidal Au nanorods. The redox reaction between Au ions generated from the anode and Ag metal leads to the formation of Ag ions and the concentration of Ag ions, and their release rate have been found to be the key factors that determine the aspect ratio of the nanorods, though the exact role of the Ag ions is still unclear at the present stage.

The seed-mediated growth method is so far the most popular method for the synthesis of colloidal Au nanorods [15, 85–87, 97]. The seed-mediated growth method has several advantages over other approaches, such as the simplicity of the procedure, high yield of nanorods, ease of tight control over aspect ratios, and flexibility for structural modifications. The anisotropic growth of Au nanoparticles was first reported in 1989 by Wiesner and Wokaun [98] who fabricated anisotropic Au colloids by introducing Au nuclei into $HAuCl_4$ growth solutions. This idea was further developed into a robust seed-mediated chemical approach for the controllable fabrication of Au nanorods originated in 2001 by Murphy and coworkers [99, 100]. For more explicit details about the seed-mediated growth of Au nanorods, the readers are referred to several excellent reviews by Murphy group [86, 97], El-Sayed group [85], and Mulvany group [87, 101].

The earliest version of nanorod fabrication protocol developed by Murphy group [99, 100] involves the addition of citrate-capped small Au nanospheres to a bulk $HAuCl_2$ growth solution obtained by the reduction of $HAuCl_4$ with ascorbic acid in the presence of CTAB surfactant and $AgNO_3$, which results in the formation of Au nanorods with aspect ratio of 1–7. In 2003, Nikoobakht and El-Sayed [13] made

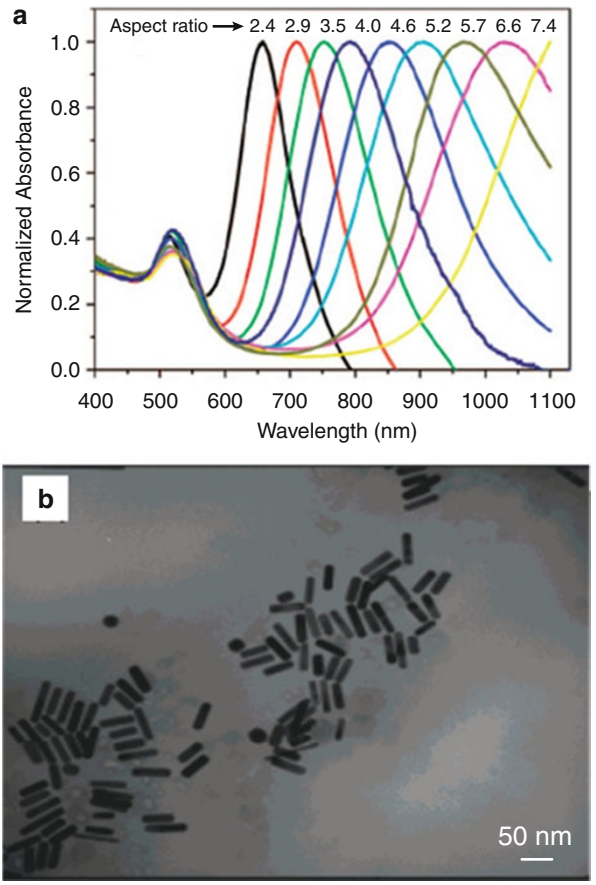

Fig. 1.11 (**a**) Extinction spectra of experimentally fabricated Au nanorods with different aspect ratios. (**b**) TEM image of nanorods of aspect ratio of 4.0 (Adapted with permission from Ref. [13]. Copyright 2003 American Chemical Society)

two modifications to this protocol: replacing sodium citrate with sodium borohydride, a stronger reducing agent in the seed formation process, and utilizing silver ions to control the aspect ratio of the resulting Au nanorods. This method produces high-yield Au nanorods (99 %) with aspect ratios from 1.5 to 4.5. To grow Au nanorods with further increased aspect ratios up to ~20, a three-step seeding method has been developed by Murphy and coworkers [12]. Another way to increase the aspect ratio of the resulting Au nanorods in high yield is to use a cosurfactant, such as benzyldimethylhexadecylammonium chloride (BDAC), in addition to CTAB. The BDAC–CTAB binary surfactant system produces nanorods with aspect ratios of up to 10 by changing the silver concentrations (Fig. 1.11) [13]. Using the Pluronic F-127 cosurfactant system, the aspect ratio can further increase up to 20 [43]. Introduction of other reagents into the growth solution can further adjust the kinetics of the nanorod growth and even longer nanorods can be obtained. For example, adding controllable amount of nitric acid into the growth solution

significantly enhances the production of nanorods with high aspect ratio over 20 [102]. Long Au nanorods with aspect ratios of up to 70 can be fabricated in high yield by controlling the volume of the growth solution [103].

Using the seed-mediated growth method, the yield, monodispersity, and aspect ratio of the resulting Au nanorods are all sensitively dependent on a whole set of experimental parameters, such as seed concentration, seed size, reducing agent, temperature, pH values, Au precursor concentration, surfactant concentration, the use of other cosurfactants, other additives, and even the nanorod aging time. Variation of experimental parameters of the nanorod fabrication protocol may also result in significant modifications to the typical cylindrical shape of the Au nanorods and even the formation of Au nanoparticles in other shapes, such as nanocubes, nano-dogbones, nanopolyhedral, and branched nanocrystals [104]. It is particularly worth mentioning that silver ions in the growth solution are the key factor that controls the dimensions of the resulting Au nanorods. In addition, the properties of the surfactants, such as chain length, head group structure, counterions, and even the purity of CTAB surfactant, play important roles in the nanorod growth. Korgel and coworkers [105] reported that even with exactly the same recipe, CTAB from different suppliers with different catalog numbers affects not only the aspect ratio but also the yield and monodispersity of the nanorods, due to the existence of impurities. They later found out that iodide, the low concentration impurity in CTAB, is the key shape-directing element that inhibits the nanorod growth [106].

Au nanorods can also be conveniently prepared by seedless photochemical growth in the presence of selected surfactants. Yang and coworkers first synthesized uniform Au nanorods with tunable aspect ratios in the range of 1–5 by irradiating gold ions in a micellar solution with a 254-nm ultraviolet light (420 $\mu W/cm^2$) for $\sim$30 h [107]. In analogy to the seed-mediated synthesis, the aspect ratio of the resulting Au nanorods can be controlled through the addition of silver ions using this photochemical approach [107–110]. In addition to the silver ions, the photochemical anisotropic growth of Au nanorods can also be controlled by other experimental parameters, such as irradiation light source and additives in the reaction solutions [111–113].

Lithographic techniques are top-down methods used in the production of Au nanostructures with highly controllable dimensions and orientation. Well-aligned Au nanorod structures supported on substrates have been fabricated using electron beam lithography (EBL) [114] and focused ion beam (FIB) lithography techniques [115]. However, these lithography techniques are not as widely used for nanorod fabrication as the bottom-up chemical approaches mentioned above due to three major reasons. First, lithographic techniques are much more expensive and time-consuming than bottom-up chemical approaches. Second, nanorods generated through lithography approaches are much larger than those from bottom-up chemical approaches due to the resolution limit of these top-down techniques. Third, nanostructures can be fabricated over a limit area of a substrate each time, and large-scale fabrication of free-standing nanorods is beyond the capability of lithographic techniques.

6.3 Geometry-Dependent LSPR Lifetimes of Au Nanorods

In addition to the LSPR frequencies, the LSPR linewidths of Au nanorods have also been observed to be dependent on the geometric parameters of the nanorods. Upon plasmonic excitation, the collective electron oscillations may undergo a number of damping or dephasing processes, either radiatively or nonradiatively, which ultimately result in the decay of the plasmon. Radiative damping occurs when the oscillating dipole moment of the plasmon gives rise to photon emission, while nonradiative damping occurs when the plasmon excites intraband or interband electronic transitions or through electron scattering processes at the surface of the nanostructures. The resonance linewidth provides a measure of these processes as it is inversely proportional to the plasmon lifetime [116]. Using ensemble spectroscopies to accurately characterize the intrinsic LSPR linewidth of nanoparticles has been challenging because the measured LSPR linewidth only provides ensemble-averaged information that includes both inhomogeneous broadening due to the size and shape distributions of the samples and the intrinsic band broadening of individual nanoparticles. Therefore, single-particle spectroscopic measurements have to be carried out to accurately probe the intrinsic LSPR linewidth of individual nanoparticles.

Sönnichsen et al. [117] used a dark-field microscope to measure the Rayleigh scattering from individual nanospheres of various sizes and individual nanorods with varying aspect ratios (see Fig. 1.12). They found that the longitudinal LSPRs of nanorods were significantly narrower than those of nanospheres and the LSPR linewidths of nanorods decreased as the aspect ratio of nanorods increased, indicating that the higher aspect ratios corresponded to longer LSPR lifetimes. There are numerous decay routes available to the longitudinal LSPR of nanorods. By tailoring the geometric parameters of nanorods, one can modify the plasmon decay pathways and achieve the optimized geometry that gives rise to the longest plasmon lifetimes [118]. The LSPR linewidths of nanorods have also been found to be determined by the width of the nanorods. Hartland and coworkers [116] measured the light scattering from individual Au nanorods of various widths but approximately the same aspect ratios. Keeping the aspect ratio constant ensures that the resonance frequencies and, therefore, the bulk dephasing contributions are similar for all samples. Due to the increased radiative damping associated with larger volumes, linewidth broadening was observed as the width of the nanorod increased. However, increased broadening for small nanorod widths was also observed due to the surface scattering of electrons occurring when the nanorod dimension became significantly smaller than the electronic mean free path of Au (~20 nm). These two competing processes lead to an optimum nanorod width in the range of 10–20 nm where the resonance is sharpest and the LSPR lifetime is the longest.

6.4 Geometrically Tunable Photoluminescence of Au Nanorods

Bulk materials of noble metals, such as Au, Ag, and Cu, exhibit extremely weak fluorescence with quantum yield on the order of 10^{-10} due to the rapid nonradiative

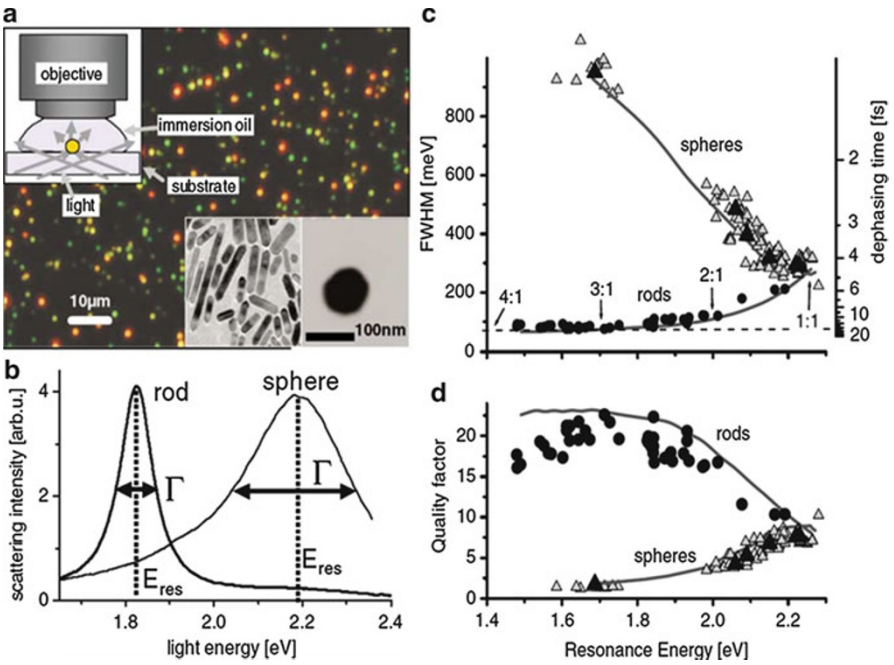

Fig. 1.12 (**a**) True color photograph of a sample of Au nanorods (*red*) and 60-nm nanospheres (*green*) in dark-field illumination (*inset upper left*). *Bottom right*: TEM images of a dense ensemble of nanorods and a single nanosphere. (**b**) Light-scattering spectra from a Au nanorod and a 60-nm Au nanosphere measured under identical conditions (light polarized along the long rod axis). (**c**) Measured linewidth Γ of plasmon resonances in single nanorods (*dots*) and nanospheres (*open triangles*) versus resonance energy E_{res}. (**d**) Same data plotted as quality factor $Q = E_{res}/\Gamma$ (Reprinted with permission from Ref. [117]. Copyright 2002 American Physical Society)

electron–hole recombinations [119]. Experimental and theoretical results published by Shen and coworkers [120] indicate that photoluminescence of noble metals can be attributed to an interband recombination of the electrons and holes. In contrast to the weak emission from bulk metals, large enhancement in emission on roughened metal surfaces has been observed largely due to local field enhancements around the surface of the metal [120].

Au nanorods exhibit interesting geometrically tunable photoluminescence properties. Although it essentially arises from interband recombinations of electrons and holes, the photoluminescence of Au nanorods is sensitively dependent on the tunable LSPRs. Mohamed and El-Sayed et al. [121] observed that Au nanorods with aspect ratios less than 3 have fluorescence quantum efficiency on the order of 10^{-4} to 10^{-3}, which is 6–7 orders of magnitude higher than that observed in the bulk materials, whereas almost no photoluminescence enhancements are observable for Au nanospheres. Such emission enhancements are directly related to the longitudinal LSPR of Au nanorods as the polarization of the emission is along the

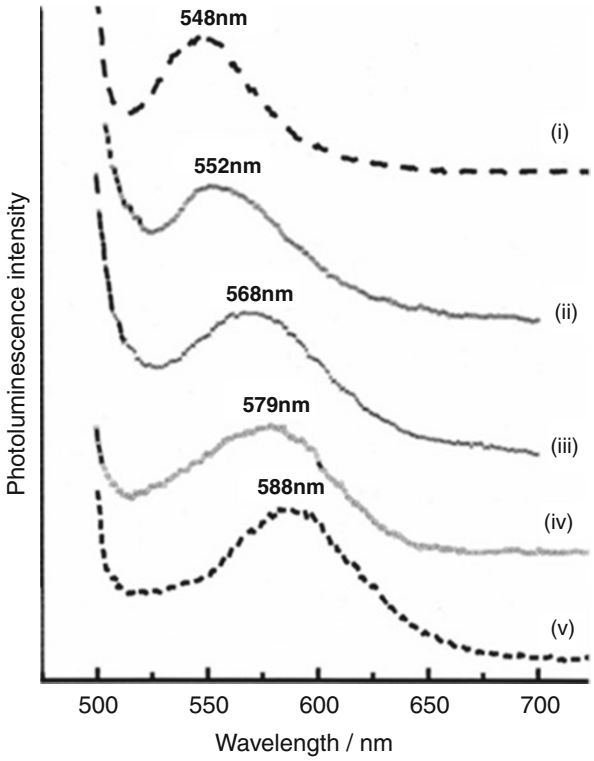

Fig. 1.13 Photoluminescence spectra i, ii, iii, iv, and v for Au nanorods of average aspect ratios of 2.0, 2.6, 3.3, 4.3, and 5.4, respectively. The excitation wavelength is 488 nm (Reprinted with permission from Ref. [121]. Copyright 2005 American Chemical Society)

long rod axis. The excitation of interband absorption simultaneously excites the longitudinal LSPR of Au nanorods, which results in enhanced local electric fields amplifying both excitation and emission fields. Interestingly, the photoluminescence maximum wavelength is found to increase linearly with increasing aspect ratio (Fig. 1.13) [122]. The quantum efficiency increases quadratically for aspect ratios below three and then begins to diminish thereafter. A detailed examination of the enhanced emission intensity was carried out for nanorods including high aspect ratios by Eustis and El-Sayed. Both the experimental data and simulation results show that the emission depends on three important factors: (1) the intensity of enhanced electric field associated with the longitudinal LSPRs, (2) the extent of spectral overlap between the interband absorption band and the LSPR band which determines the enhancement of the interband absorption of light, and (3) the overlap of the fluorescence spectrum of Au with the LSPR absorption band which determines the enhancement of the outgoing emitted fluorescence light. Because the LSPR absorption shifts to longer wavelengths as the nanorod aspect ratio increases,

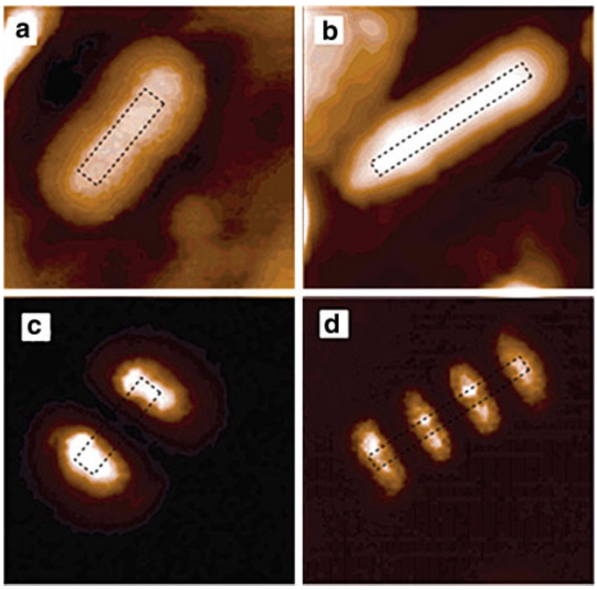

Fig. 1.14 (**a**, **b**) Topographic images of Au nanorods. (**c**, **d**) TPI-PL images for **a** and **b**, respectively (Reprinted with permission from Ref. [124]. Copyright 2004 American Chemical Society)

the extent of the overlap between the interband processes and the longitudinal LSPR absorption band will change accordingly. In the small aspect ratio regime, increase in the aspect ratio results in greater spectral overlap responsible for an emission enhancement. In the large aspect ratio regime, however, further increase in aspect ratio diminishes the degree of spectral overlap, resulting in decreased emission intensities.

Similar to one-photon photoluminescence, the two-photon-induced photoluminescence (TPI-PL) peaks of Au nanorods also redshift with increasing aspect ratio [123] and are more intense than that of spheres. The TPI-PL response originates from the sequential excitation of an intraband transition from just below the Fermi level, followed by a second d-band excitation to where the hole was created by the first excitation. Photoluminescence subsequently occurs when the remaining radiative charge–hole recombination takes place. Since two-photon optical processes involve an additional field enhancement, further enhanced photoluminescence is expected in comparison to the one-photon case. It has been reported by Okamoto and coworkers [124–126] that TPI-PL is also useful for revealing the near-field enhancements of individual Au nanorods associated with LSPR excitations (Fig. 1.14). Observation of TPI-PL from single nanoparticles enabled by NSOM measurements provides essential information for revealing the spatial distribution of the electric fields near the nanoparticle when a characteristic LSPR mode is excited. By locally exciting regions along the length of the nanorod while simultaneously monitoring the TPI-PL from the entire nanorod, the portions of the nanorod that yielded the strongest response can be mapped out [124–126]. Where the plasmon shows the strongest internal electric field, it also shows the strongest TPI-PL. Because of their interesting NIR TPI-PL properties, molecularly targeted

Au nanorods have been used as contrast agents for TPI-PL-based bioimaging both in vitro and in vivo [127, 128]. The TPI-PL signals from a single nanorod are found to be 57 times higher than those from a single rhodamine molecule [127].

7 Metallic Nanoshells

7.1 Tunable LSPRs of Nanoshells

Metal nanoshells are a class of fascinating subwavelength photonic particles with highly tunable plasmonic properties [24]. A nanoshell is composed of a spherical dielectric or semiconducting core homogenously coated with a concentric nanoscale metallic shell. By tailoring the geometric parameters of nanoshells, one can fine-tune the particles' light absorption and scattering properties all the way across the visible and NIR spectral regions, enabling widespread applications, such as optically triggered drug delivery [129], chemical and biomolecular sensing [130], surface-enhanced spectroscopies [131–134], and cancer diagnostic and photothermal therapy [9, 135, 136].

Because nanoshells are spherically symmetric, their LSPRs can be analytically described by Mie scattering theory. In 1951, Aden and Kerker [137] first proposed the model for simulating the absorption and scattering of electromagnetic waves from a spherical particle consisting of a dielectric core and a metallic shell based on Mie scattering theory. Neeves and Birnboim [138] proposed in 1989 that such a core–shell geometry could give rise to LSPR modes with their wavelengths tunable over a broad spectral range. The LSPRs of a nanoshell are extraordinarily sensitive to the inner and outer dimensions of the metallic shell layer. Figure 1.15 shows the optical extinction spectra of Au nanoshells calculated using Mie scattering theory [23]. In this set of calculations, the radius of the silica core was fixed at 60 nm, and the shell thickness was varied from 5 nm to 20 nm. Since the overall sizes of the Au nanoshells are beyond the quasi-static limit, both the dipole and quadrupole LSPR bands show up in the extinction spectra and progressively redshift as the shell thickness decreases. In this example, as the core radius–shell thickness ratio is varied between 3 and 12, the predicted resonances of the nanoshells span a range of 300 nm in wavelength. In contrast, if the order of these layers were inverted, that is, a Au core and a dielectric silica shell, less than a 20-nm optical resonance shift would be expected.

There is a long development gap between the original theoretical predictions about nanoshell plasmons and the experimental realization of the nanoshell geometry. The earliest example of experimentally fabricated nanoshells is Au_2S–Au core–shell nanoparticles produced by the reduction of $HAuCl_4$ in an aged Na_2S solution [22, 139]. By adjusting the amount ratios between $HAuCl_4$ and Na_2S, Au_2S–Au nanoshells can be grown with different core sizes and shell thicknesses. However, the tuning range of the overall size (<40 nm) and LSPR wavelength (600–900 nm) of the Au_2S–Au nanoshells is rather limited. Additionally, a large number of Au colloids are formed as a secondary product, generating an additional absorption peak at ~520 nm.

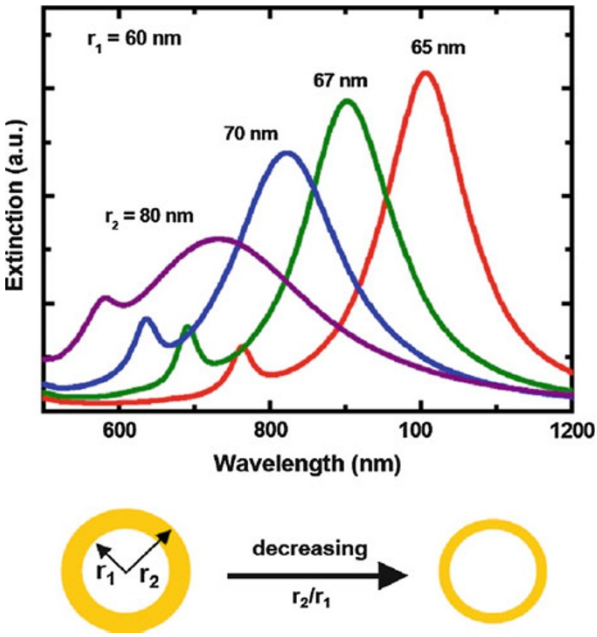

Fig. 1.15 Plasmonic tunability demonstrated for nanoshells with an inner silica core radius $r_1 = 60$ nm and an overall particle radius $r_2 = 65$, 67, 70, and 80 nm. The plasmon resonance (extinction) of the particles redshifts as r_1/r_2 increases (Adapted with permission from Ref. [23]. Copyright 1998 Elsevier B. V.)

Halas and coworkers have done pioneering work on the fabrication of metal nanoshells through a multistep, seed-mediated electroless plating approach [23]. In 1998, they controllably fabricated silica–Au core–shell nanoparticles, which overcame many of the limitations of the Au_2S–Au nanoshells. The whole procedure for the fabrication of the silica–Au nanoshells can be schematically illustrated in Fig. 1.16a. Highly monodisperse silica cores with precisely controlled diameters ranging from 50 to 800 nm are fabricated using the Stober method [140]. The surfaces of the silica core particles are then functionalized with amine groups, and small Au colloids (1–2 nm) are subsequently adsorbed onto the silica surfaces through Au–amine interactions. The immobilized Au colloids act as nucleation sites that catalyze the electroless plating of Au to form Au islands on the surface of silica. As increasing amount of Au is plated, the Au islands gradually grow larger and eventually coalesce to form a complete Au nanoshell. Figure 1.16b shows a set of TEM images that reveal the whole process of Au nanoshell growth on the surface of the silica cores. The final thickness of the Au nanoshells, which is typically in the range from 5 to 100 nm, can be precisely controlled by adjusting the amount ratio between silica and $HAuCl_4$ added. By using this seed-mediated electroless plating method, continuous Au [141–143], Ag [144, 145], Cu [146], and bimetallic nanoshells [147] with controllable core and shell dimensions have been successfully fabricated using silica, polymer, or cuprous oxide beads as core materials. The experimental extinction spectra of nanoshells show very good agreement with the calculated results using Mie theory, both at the ensemble [23, 148, 149] and single-nanoparticle levels [150].

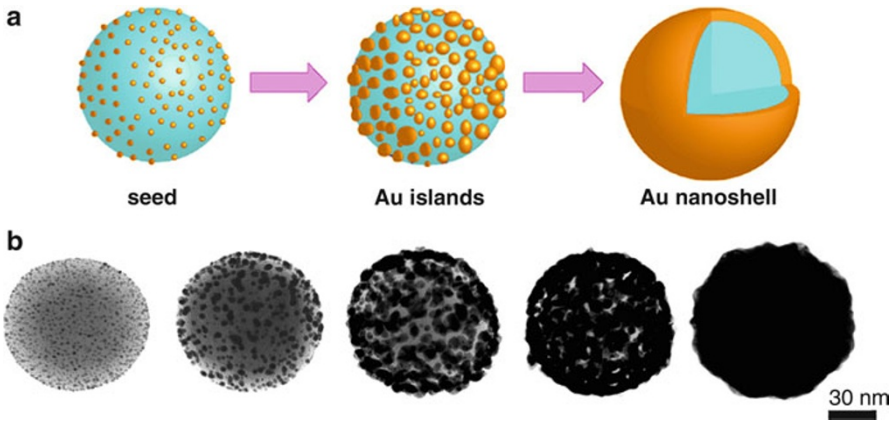

Fig. 1.16 (**a**) Scheme of seed-mediated electroless plating of Au nanoshells surrounding silica cores. (**b**) TEM images that reveal the whole process of Au nanoshell growth on the surface of silica cores (Reprinted with permission from Ref. [23]. Copyright 1998 Elsevier B. V.)

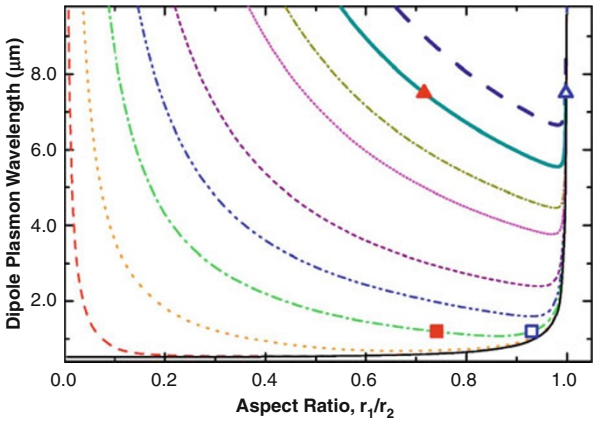

Fig. 1.17 Calculated dipole plasmon resonance of silica core–Au shell nanoshells with core radii of 0.1 (*solid*), 10 (*dashed*), 50 (*dotted*), 120 (*dash dotted*), 200 (*dash dot dotted*), 300 (*short dashed*), 500 (*short dotted*), 600 (*short dash dotted*), 750 (*thick solid*), and 900 nm (*thick dashed navy*). The *solid* and *hollow triangles* and *squares* are experimental data (Reprinted with permission from Ref. [151]. Copyright 2007 American Institute of Physics)

By tailoring the relative core–shell ratio and overall sizes of nanoshells, the frequencies of nanoshell LSPRs can be fine-tuned all the way across the visible, NIR, and mid-IR regions [23, 148, 151]. In Fig. 1.17, the optical resonance as a function of core–shell ratio is calculated for the silica–Au nanoshell system with varying overall dimensions both within and beyond the quasi-static limit [152]. These theoretical studies indicate that for small silica–Au nanoshells within the

quasi-static limit, inner–outer radius ratios close to 1 could in principle give rise to optical resonances shifted into the infrared as far as 10 μm in wavelength, though nanoshells with these extremely thin shells are impossible to fabricate experimentally. Known as phase retardation or finite size effects, the immediate impact of increasing particle size beyond the quasi-static limit results in a systematic shifting of the dipole plasmon to lower energies and a significant broadening of the plasmon resonance linewidth. Higher-order multipolar resonances appear as particle size is increased, as distinct spectral features at energies higher than that of the dipolar plasmon energy. Although the dipolar plasmon response of metallic nanoshells has been shown to be remarkably robust in the presence of defects or imperfections in the nanoparticle's metallic layer, the higher-order modes can be significantly damped by nanoscale surface texturing of the nanoshells [153, 154]. Practically, one can shift the nanoshell LSPRs deep into the IR region using nanoshells with relatively large core sizes and thin shell thicknesses. For small nanoshells within the quasi-static limit, the extinction properties are dominated by absorption rather than scattering, while for large nanoshells beyond the quasi-static limit, the extinction is dominated by scattering. Therefore, one can selectively tune the light absorption and scattering properties of nanoshells by controlling the overall size of the nanoshells.

Nanoshell LSPRs are also much more sensitive to local environment than solid nanospheres [149], significantly redshifting as the refractive index of surrounding medium increases. The sequence of LSPR sensitivity is typically dipole > quadrupole > octupole > higher-order modes. The LSPR sensitivity of nanoshells depends primarily on overall nanoparticle size and less sensitively on the core–shell ratio. Understanding how the geometrical parameters control LSPR sensitivities offers insight toward the design and engineering of nanoshell sensors for LSPR sensing applications.

Although the geometry dependence of nanoshell LSPRs can be analytically described by the Mie scattering theory, this classical electromagnetic theory provides little insights into the origin of nanoshells' optical tunability. Numerical computation methods, such as FDTD, have been used to simulate the plasmonic properties of nanoshells [155]; however, they do not provide a clear picture of the underlying physics behind the geometrically tunable nanoshell plasmons. In this context, plasmon hybridization theory, a plasmonic analog to the molecular orbital theory, has emerged as an effective and powerful method that can be used to fundamentally interpret the origin of the plasmonic tunability of metal nanoshells [156–158]. Next we will briefly introduce the basic ideas of plasmon hybridization model and demonstrate how it can be used to interpret the structure–property relationship of nanoshells. The plasmon hybridization picture extends to an entire family of nanoshell-based geometries with increasing structural complexity, such as multilayer shell-in-shell structures known as nanomatryushkas, nanoshells with offset cores known as nanoeggs, semi-nanoshell structures (half-shells, nanocups, and nanocaps), and spheroidal nanoshells known as nanorice. We will demonstrate how plasmon hybridization model can be used as a powerful tool to both predict and analyze the tunable optical properties of these complex nanoshell-based structures.

7.2 Plasmon Hybridization Model

Plasmon hybridization theory provides a conceptually enlightening method for calculating the plasmon resonance of complex nanostructures. The basic idea of plasmon hybridization theory is to deconstruct a nanoparticle or composite structure into more elementary shapes and then calculate how the primitive plasmons supported by the elementary geometries interact or hybridize with each other to form the hybridized plasmons of the composite structure. This theory enables scientists to draw on decades of intuition from molecular orbital theory to predict the plasmonic response of nanostructures with increasing structural complexity [159].

Plasmon hybridization model considers the conduction electrons of a metal to be a charged, incompressible, and irrotational fluid sitting on a rigid, uniform, and positive background charge representing the fixed ion cores. The deformation of the fluid can be expressed in terms of a scalar function η. Infinitesimal deformations in this fluid give rise to a surface charge density that interacts electrostatically, and plasmons are considered to be the self-sustained oscillations of this electron fluid. The Lagrangian for such a system is

$$L = \frac{n_0 m_e}{2} \int \eta \vec{\nabla} \eta \cdot dS - \frac{1}{2} \int \frac{\sigma(\vec{r}) \sigma(\vec{r}')}{|\vec{r} - \vec{r}'|} dS dS' \tag{1.13}$$

where n_0 is the free-electron density, m_e is the mass of electrons, and σ is the surface charge density,

$$\frac{d}{dt}\sigma = n_0 e \frac{d\eta}{d\hat{n}} \tag{1.14}$$

and the integrations are performed over all surfaces of the metal. The plasmon modes of the systems are obtained from the Euler–Lagrange equations.

In the context of plasmon hybridization model, the geometry-dependent nanoshell plasmon resonances result from the interaction between the essentially fixed-frequency plasmon response of a sphere and that of a cavity (Fig. 1.18a) [156, 157, 159]. Sphere and cavity plasmons are electromagnetic excitations at the outer and inner interfaces of the metal shell, respectively. Because of the finite thickness of the shell layer, the sphere and cavity plasmons interact with each other and hybridize in a way analogous to the hybridization between atomic orbitals. This interaction results in the splitting of the plasmon resonances into two new resonances, the lower-energy symmetric or "bonding" plasmon (ω_-) and the higher energy antisymmetric or "antibonding" plasmon (ω_+).

The hybridization of the cavity and the sphere plasmons depends on the difference in their energies $\omega_{C,l}$ and $\omega_{S,l}$ and on their interaction, which is determined by the thickness of the shell. To describe the geometry of a nanoshell, the notation (a, b) is adopted to indicate the inner radius a and the outer radius b of the shell. The hybridization between the cavity and sphere

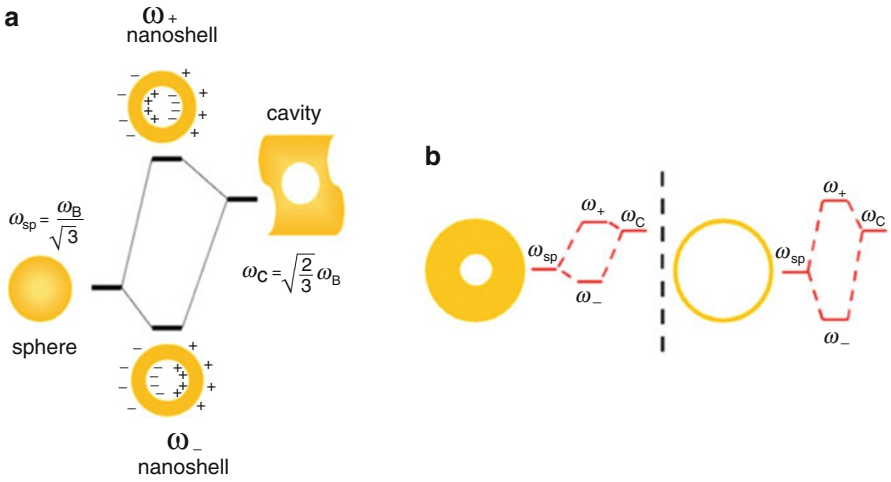

Fig. 1.18 Energy-level diagram (**a**) depicting plasmon hybridization in metal nanoshells and (**b**) illustrating the dependence of nanoshell plasmon energies on the strength of the interaction between the sphere and cavity plasmons, determined by the thickness of the metallic shell (Reprinted with permission from Ref. [159]. Copyright 2007 American Chemical Society)

plasmons gives rise to two hybridized plasmon modes $|\omega_+\rangle$ and $|\omega_-\rangle$ for each $l > 0$. The frequencies of these modes are

$$\omega_{l\pm}^2 = \frac{\omega_B^2}{2}\left\{1 \pm \frac{1}{2l+1}\left[1 + 4l(l+1)\left(\frac{a}{b}\right)^{2l+1}\right]^{1/2}\right\} \tag{1.15}$$

The $|\omega_+\rangle$ mode corresponds to antisymmetric coupling between the sphere and cavity modes, and the $|\omega_-\rangle$ mode corresponds to symmetric coupling between the two modes (see Fig. 1.18b). The ω_- plasmon interacts strongly with the incident optical field, while the ω_+ mode interacts weakly and, in the case of Au, is further damped by interband transitions at energies above the d-band to Fermi energy optical transitions at approximately 2.3 eV.

The validity of this expression for the nanoshell plasmon energies has been explicitly verified using fully quantum mechanical calculations [160]. Although the resulting plasmon energies are the same as what would be obtained from a Drude dielectric function and classical Mie scattering theory in the quasi-static limit, the present treatment very clearly elucidates the nature of the nanoshell plasmon resonances and, in particular, the microscopic origin of their sensitive dependence on geometry. For example, this picture provides a simple and intuitive explanation for why the energy of the optically active plasmon resonance shifts to lower energies with decreasing shell thickness: the decreased shell thickness leads to a stronger coupling between the sphere and cavity plasmons, increasing the splitting between the bonding and antibonding hybridized plasmons. The plasmon

hybridization model can also be used to interpret the LSPR sensitivity of nanoshells to surrounding medium. As illustrated in Fig. 1.18b, the optically bright plasmon mode (ω_-) is more sphere-like, while the optically dark plasmon mode (ω_+) is more cavity-like. Therefore, ω_- sensitively shifts upon a change in refractive index of the embedding medium, while ω_+ is more sensitive to the change of the core materials.

7.3 Nanomatryushkas

The plasmon hybridization picture extends naturally to more complicated multilayer nanoshell structures known as nanomatryushkas [156, 161]. The nanomatryushka geometry can be experimentally realized by first growing a uniform nanoscale layer of Au surrounding a silica nanoparticle, then coating this nanoparticle with a silica layer of controlled thickness, followed by the growth of a second thin Au layer. A schematic depicting the composition of this particle is shown in Fig. 1.19a. The plasmon responses of this structure can be understood as a hybridization of the plasmon resonances of the inner and outer nanoshells. As illustrated in Fig. 1.19b, for each multipolar symmetry, there are four linearly independent plasmon modes. Obviously, the thickness of the dielectric spacer layer $|a_2 - b_1|$ controls the strength of the coupling between the inner and outer nanoshells, whose plasmon resonances can each be tuned independently.

The energy-level diagram in Fig. 1.19b depicts the hybridization of the concentric nanoshell plasmons in terms of the mixing of the inner- and outer-shell plasmons. The experimentally observable eigenmodes correspond to the hybridization of the bonding plasmon modes of the two metal shell layers. Figure 1.19c shows the strong coupling case. Spectrum (1) shows the experimental and theoretical extinction spectra for the isolated inner-shell plasmon $\left|\omega_{-,NS1}\right\rangle$. Spectrum (2) is the theoretical extinction spectrum of the isolated outer-shell plasmon $\left|\omega_{-,NS2}\right\rangle$, calculated as though the inner-shell structure was replaced wholly by a dielectric (silica) core. Spectrum (3) is the experimental and theoretical extinction for the concentric nanoshell in which $\left|\omega^{+}_{-,CS}\right\rangle$ and $\left|\omega^{-}_{-,CS}\right\rangle$ plasmons are clearly apparent. The plasmon hybridization and splittings are quite strong because of the small interlayer spacing between inner- and outer-metal shell layers and the fact that the inner-shell plasmon $\left|\omega_{-,NS1}\right\rangle$ and outer-shell plasmon $\left|\omega_{-,NS2}\right\rangle$ are nearly resonant with each other. The hybridization of the plasmons appears to be strongly asymmetric primarily due to phase-retardation effects. A second contributing factor to the asymmetry is the small but finite interaction with the higher energy $\left|\omega_{+,NS1}\right\rangle$ and $\left|\omega_{+,NS2}\right\rangle$ plasmon modes. Figure 1.19d depicts a concentric nanoshell with a weak plasmon coupling between the inner and outer shell. In this case, the inner- and outer-plasmon resonances are detuned from each other in energy, as the spacing between inner and outer-metal layers is increased. Because the hybridization is weak, the concentric shell plasmon modes show only small shifts relative to the isolated shell plasmons. In Fig. 1.19e, a concentric nanoshell with a fully decoupled

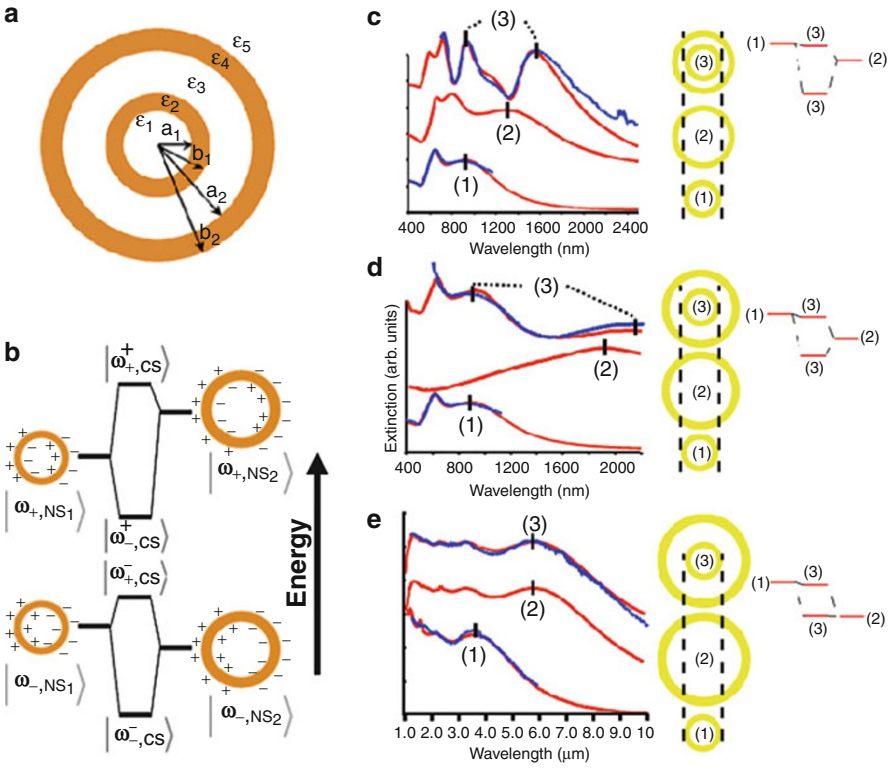

Fig. 1.19 (**a**) Concentric nanoshell geometry with concentric radii of core (a_1), inner shell (b_1), spacer layer (a_2), and outer shell (b_2) where ε_1 and ε_3 are assumed to be SiO_2, ε_2 and ε_4 are Au, and ε_5 is embedding medium. (**b**) Energy-level diagram of hybridization between the inner and outer nanoshell plasmons. (**c**) Experimental (*blue*) and theoretical (*red*) extinction spectra for concentric nanoshells (3), inner shell (1), and outer shell (2); the inner- and outer-nanoshell plasmons interact strongly, resulting in strongly hybridized plasmons. (**d**) The inner- and outer-nanoshell plasmons interact weakly with a relatively small change in the concentric nanoshell plasmon compared with single-nanoshell plasmons. (**e**) Noninteracting inner- and outer-shell plasmons (Adapted with permission from Ref. [156]. Copyright 2003 American Association for the Advancement of Science)

plasmon response is shown. In this case, the intershell spacing is so large that the concentric nanoshell response (3) appears to be almost indistinguishable from the calculated nanoshell response for the outer shell. Because of the large intershell spacing and the finite penetration depth of the light, the inner-nanoshell plasmon is not excited.

Recently, Halas and coworkers reported that the geometrically tunable optical properties of another type of nanomatryushkas are composed of a silica-coated gold nanosphere surrounded by a Au nanoshell layer in a sub-100-nm-size range [162]. The nanoshell was fabricated by seed-mediated electroless plating of Au onto silica-coated Au nanoparticles using CO as the reducing agent. This approach allows independent control over the size of the Au core, the silica layer thickness,

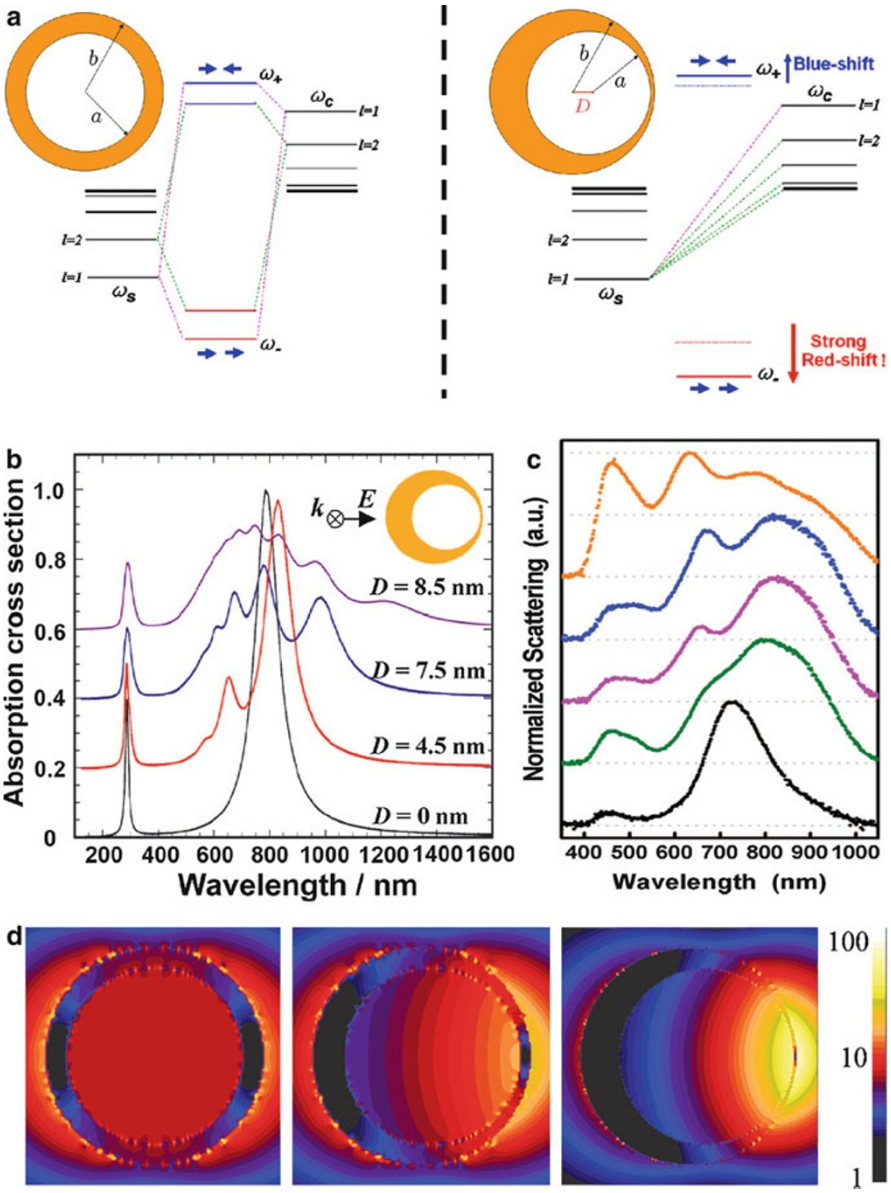

Fig. 1.20 (**a**) Schematic of plasmon hybridization in a nanoshell (*left*) and a nanoegg (*right*). (**b**) Theoretical absorption spectra as a function of offset D obtained by the plasmon hybridization method, for a $[a, b] = [39, 48]$-nm Au nanoshell with vacuum core. (**c**) Experimentally measured single-particle dark-field scattering spectra of a nanoshell (*black curve*, $[a, b] = [94, 103]$ nm.) and four nanoegg particles with varying core offset (*colored spectra*, D increases from bottom to top). (**d**) Near-field plots of $[a, b] = [39, 48]$-nm Au nanoshells with different offset cores and an empirically based dielectric function for Au. *Left*: $D = 0$ nm at $\lambda = 604$ nm. *Center*: $D = 4.5$ nm at

and the thickness of the Au nanoshell layer. Therefore, detailed investigation on plasmon hybridization between the Au nanosphere core and Au outer nanoshell becomes possible with minimized phase-retardation effects. As the core–shell interactions become stronger, a larger split between $\left|\omega^{+}_{-,CS}\right\rangle$ and $\left|\omega^{-}_{-,CS}\right\rangle$ can be observed with $\left|\omega^{-}_{-,CS}\right\rangle$ further redshifted and $\left|\omega^{+}_{-,CS}\right\rangle$ progressively blueshifts. The resulting plasmon resonances are in exact agreement with Mie scattering theory.

7.4 Nanoeggs

Symmetry breaking can introduce dramatic changes in the optical properties of the plasmonic nanoshells. The plasmon hybridization picture can be applied to a nanoshell with an offset core known as a nanoegg [163, 164]. For a spherically symmetric nanoshell, where the center of the inner-shell radius is coincident with the center of the outer-shell radius, plasmon hybridization only occurs between cavity and sphere plasmon states of the same angular momentum, denoted by multipolar index $l(\Delta l = 0)$. In the quasi-static limit, only the $l = 1$ dipolar bonding plasmon is excited by an incident optical plane wave. However, when the center of the inner shell is displaced with respect to the center of the outer shell, this selection rule is relaxed, and cavity and sphere plasmons of all multipolar indices hybridize. As a consequence, all plasmon modes can be optically excited, even in the dipole limit, resulting in a multipeaked and redshifted plasmonic response with increasing line-shape complexity as the core–shell displacement increases. The relaxation of the selection rules of plasmon hybridization due to symmetry breaking is schematically illustrated in Fig. 1.20a.

A nanoegg with a dielectric core of radius a displaced a distance D from the center of an outer shell of radius b can be denoted (a, b, D) and is schematically illustrated as an extension of the spherically symmetric nanoshell geometry in Fig. 1.20a. The deformation field can be expressed as a gradient of a scalar potential η [157], which takes the form

$$\eta(r_C, \Omega_C, r_S, \Omega_S) = \sum_{lm} \left[\sqrt{\frac{a^{2l+1}}{l+1}}\, \dot{C}_{lm}(t) {r_C}^{-l-1} Y_{lm}(\Omega_C) \right] + \sqrt{\frac{1}{l b^{2l+1}}}\, \dot{S}_{lm}(t) r_S^l Y_{lm}(\Omega_S) \tag{1.16}$$

Fig. 1.20 (continued) λ = 619 nm. *Right*: D = 7.5 nm at λ = 674 nm. Maximum field enhancements $|E|/|E_0|$ are 13.8, 24.5, and 67.7 from left to right. The incident field is horizontally polarized (Reprinted with permission from Ref. [163]. Copyright 2006 National Academy of Sciences of the United States of America)

where (r_C, Ω_C) are spherical coordinates centered in the cavity and (r_S, Ω_S) are spherical coordinates with an origin at the center of the spherical outer shell. The quantities of C_{lm} and S_{lm} are the amplitudes for the primitive cavity and sphere plasmons, respectively. For finite offset D, the spherical harmonics centered on the two different origins are no longer orthogonal for different l, resulting in interactions between the cavity and sphere modes in a manner analogous to the coupling between the individual nanoparticle plasmons of a nanoparticle dimer or in periodic structures of metallic nanoparticles in close proximity [158, 165, 166].

The Lagrangian for this system can be constructed directly from η. The structure of the resulting eigenvalue problem is illustrated in Fig. 1.20a [163]. The left panel shows the resulting plasmon modes for a spherically symmetric nanoshell. In this case, the plasmon energies depend on multipolar index l but not on the azimuthal index m which labels the $2l + 1$ possible orientations of the plasmon modes. For finite offset D (right panel), an interaction exists between all cavity and sphere modes of the same m. This leads to stronger hybridization and an admixture of all primitive cavity and sphere plasmons. For simplicity, we will refer to these reduced-symmetry nanoparticle plasmon modes by multipolar index l, corresponding to the spherical or zero-offset case, although for finite offset the plasmon modes contain an admixture of plasmons of all l for a given m. For the nonconcentric nanoshell, the coupling of the cavity and sphere plasmons depends on azimuthal m, but the resulting plasmon energy spectrum is only weakly dependent upon orientation. Figure 1.20b shows the theoretical optical absorption spectra of nanoeggs with $[a, b] = [39, 48]$ nm as a function of core-offset D obtained by the plasmon hybridization model. As D increases, the $l = 1$ mode is redshifted and the higher l modes, now also dipole active, contribute additional peaks to the spectrum, resulting in increased spectral line-shape complexity with increasing D. The calculated spectra using the plasmon hybridization model are in very good agreement with the results of FDTD simulations.

Nanoeggs are experimentally fabricated by anisotropically depositing additional metallic Au onto preformed silica − Au concentric nanoshells [163]. The Au nanoshells are first immobilized onto polyvinylpyridine-functionalized glass substrates as a sub-monolayer of isolated nanoshells. The nanoshell films are subsequently immersed in an aqueous solution containing an appropriate amount of chloroauric acid and potassium carbonate, where the addition of formaldehyde then initiates the electroless plating of Au onto the nanoparticle surfaces. The films are subsequently removed from the plating solution, rinsed, and dried. As a result, all the nanoeggs fabricated in this manner have the same orientation on the glass slides, with the point of contact with the glass substrate corresponding to the minimum in shell thickness for each nanoparticle. Increasing the time duration of the plating process results in an increase in the effective core offset of each nanoegg particle. The immobilized nanoeggs can be released into a solvent through sonication to form free-standing colloidal nanoegg particles. Figure 1.20c shows the single-particle scattering spectra of individual nanoeggs of increasing asymmetry. As the offset between the center of the inner- and outer-shell radius increases, the optical spectrum broadens and includes additional peaks adjacent to the original

dipolar plasmon resonance which is significantly redshifted. The experimentally obtained single-particle spectra clearly show the characteristic offset-dependent multipeaked features that are predicted by the plasmon hybridization model.

Another striking feature arising from the symmetry breaking is the near-field enhancement on the surface of nanoeggs. Figure 1.20d shows the local field enhancements calculated using the FDTD method for nanoeggs with a silica core and Au shell modeled using the empirically obtained dielectric function for Au. The largest field enhancements achievable on the outer surface dramatically increase as the core-offset D increases. Such large field enhancements on the open, exterior surface of an individual nanoparticle make nanoegg extremely promising for ultrasensitive molecular sensing based on surface-enhanced spectroscopies.

7.5 Semi-Shell Nanostructures

The case of nanoeggs has clearly demonstrated that the symmetry breaking of individual plasmonic nanostructures has profound impact to their optical properties. If a further reduction in symmetry of nanoeggs occurs when the shell is completely removed from one side of the spherical nanoparticle core, it would then result in partially broken semi-shell nanostructures known as half-shells, nanocups, or nanocaps, depending on how much of the shell is preserved in the final structures. The plasmonic responses of these semi-shell nanostructures become a sensitive function of the orientation of the nanostructure with respect to the incident light due to the asymmetry of the particle geometry.

Whitesides and coworkers fabricated semi-shell nanostructures at an approximately 50 % metal coverage (half-shell) by vertical evaporation of metal onto dielectric nanoparticles predeposited on a substrate [167]. These half-shell structures show highly tunable plasmonic properties that are significantly redshifted in comparison to the solid nanosphere plasmons. As demonstrated using Au half-shells [168], both decrease in shell thickness, and increase in core size will shift the LSPRs dramatically to longer wavelengths. Halas and coworkers [169] reported a chemical approach to two types of reduced-symmetry nanoparticles: nanocups, with approximately $70 - 80$ % metal coverage, and nanocaps, the inverse structure with approximately $20 - 30$ % metal coverage. The plasmon response of both nanocups and nanocaps was dependent upon the nanoparticle orientation with respect to incident light and polarization angle.

By carefully adjusting the angle of metal deposition with respect to the substrate orientation, Lee and coworkers [170] fabricated Au nanocup structures with sharp shell edges, which they called as nanocrescent moons (see Fig. 1.21). Unique multiple scattering peaks are observed in a single Au nanocrescent moon with dark-field white-light illumination. The sub-10-nm sharp edge of Au nanophotonic crescent moons incorporates the advantages of both metallic sharp nanotips and ultrathin nanorings and generates intense local electromagnetic-field enhancements. Lee's group later demonstrated [171] that by further incorporating magnetic components into the nanocrescent moons, each nanocrescent particle cannot only

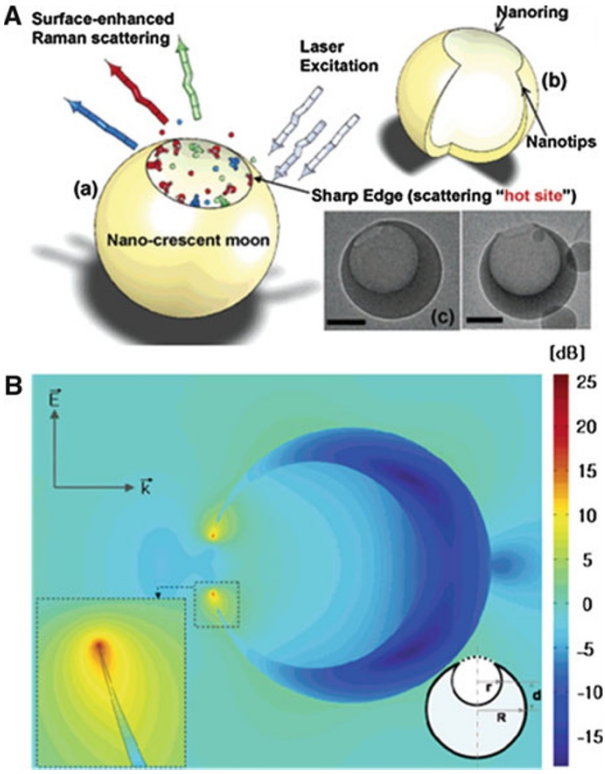

Fig. 1.21 (**A**) Au nanocrescent moons with sharp edges. (*a*) Conceptual schematics of a nanocrescent moon SERS substrate. The Au surface can be functionalized with biomolecular linker to recognize specific biomolecules. The sharp edge of the nanocrescent moon can enhance the Raman scattering intensity so that the biomolecules on it can be detected. (*b*) Geometrical schematics of a nanocrescent moon. A Au nanocrescent moon with sharp edges integrates the geometric features of nanoring and nanotips. (c) TEM images of two nanocrescent moons. Scale bars: 100 nm. (**B**) Local electric field amplitude distribution of a nanocrescent moon excited at 785 nm (Reprinted with permission from Ref. [170]. Copyright 2005 American Chemical Society)

serve as stand-alone SERS substrates with high local electromagnetic-field enhancement factors but also be manipulated by external magnetic fields to produce translational and rotational motion of the nanoprobes.

The nanocup structures can also be obtained through a unique electron-beam-induced ablation process as demonstrated by Halas and coworkers [172]. Using this approach, one can monitor the spectral evolution of individual particles as the particle morphology is reshaped from a symmetric nanoshell to an asymmetric nanoegg and eventually a nanocup. The optical response of the nanocups exhibits strong dependence on the particle orientations with respect to the polarization of the incident light due to the anisotropy of their geometry. Nanocups support both the "electric" and "magnetic" (electroinductive) plasmon modes, with potential applications as constituents in optical frequency magnetic materials or in metamaterials [173–175].

Halas and coworkers [173] systematically measured the plasmonic properties of Au nanocups and developed theoretical understanding of the origin of the plasmonic characteristics of nanocups. They showed that Au nanocups possess magneto-inductive modes that redirect scattered light in a direction dependent on particle orientation, an effect that also controls the interparticle coupling of plasmons in adjacent nanocups. As a true three-dimensional plasmonic nanoantenna, the Au nanocups exhibit unique light-bending properties.

Recently, a more complicated semi-shell nanostructure, perforated semi-shells, has been fabricated using a combination of clean-room techniques [176]. For a semi-shell with a single spherical perforation positioned on its symmetry axis, its plasmon modes strongly depend on the hole size and shape. Placing the perforation off the symmetry axis allows a family of higher-order modes to be excited in the nanostructure, along with complex near-field charge distributions for the various resonant modes. Two important variations of this structure: a semi-shell with multiple perforations in the shell layer and a semi-shell with a wedge-like "slice" in the shell layer were also investigated. A semi-shell with a wedge-like perforation can be thought of as a three-dimensional analog of a split-ring resonator, an important nanoscale component in metamaterial design.

7.6 Nanorice

Nanorice is a hybrid nanoparticle that combines the intense local fields of nanorods with the highly tunable plasmon resonances of nanoshells. This dielectric core–metallic shell prolate spheroid nanoparticle bears a remarkable resemblance to a grain of rice, inspiring the name "nanorice" (see Fig. 1.22a) [159]. This geometry possesses far greater structural tunability, along with much larger local field enhancements and far greater sensitivity as a LSPR sensor than either a nanorod or a nanoshell.

Halas and coworkers developed a seed-mediated electroless plating method for the fabrication of nanorice using spindle-shaped hematite nanoparticle cores [177]. In a typical procedure, the spindle-shape hematite (α-Fe_2O_3) nanoparticles are functionalized with (3-aminopropyl)trimethoxysilane (APTMS) to generate amine moiety-terminated surfaces. Then ultrasmall Au nanoparticles ($\sim$2 nm in diameter) were immobilized onto the surface of functionalized cores at a nominal coverage of $\sim$30 %. The immobilized Au colloids act as nucleation sites to catalyze the electroless Au plating onto the surface of core particles, leading to the gradual formation of a continuous and complete Au shell surrounding the hematite cores. By controlling the amount of Au deposited on the surface of each hematite core, the shell thickness of the nanorice can be precisely controlled. Figure 1.22b shows a SEM image of the as-fabricated hematite core–Au shell nanorice particles. Figure 1.22c shows the experimentally measured optical extinction spectra of nanorice with varying shell thicknesses. For each sample, two well-defined plasmon modes are observed. The strong plasmon resonance feature observed at longer wavelengths arises due to the excitation of longitudinal plasmon supported

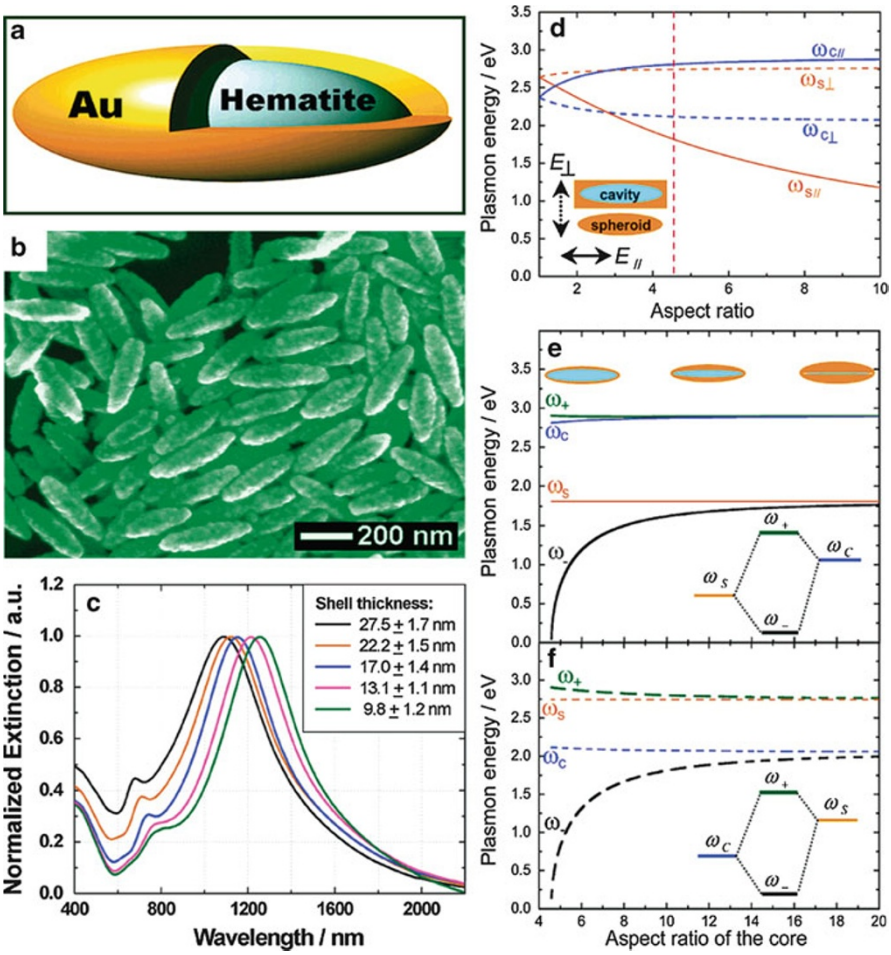

Fig. 1.22 (**a**) Illustration of nanorice, (**b**) SEM image, and (**c**) extinction spectra of nanorice with different shell thicknesses fabricated on a hematite core with longitudinal diameter of 340 ± 20 nm and transverse diameter of 54 ± 4 nm, (**d**) plasmon energy versus aspect ratio (major radius/minor radius) of the solid prolate spheroid and prolate cavity (*solid lines*, longitudinal plasmon; *dashed lines*, transverse plasmon), and (**e**) longitudinal and (**f**) transverse plasmon energies versus core aspect ratio for an aspect ratio of 4.575 (Reprinted with permission from Ref. [159]. Copyright 2007 American Chemical Society)

by the nanorice structure. The little shoulder at shorter wavelengths is mostly corresponding to the transverse plasmon mode of nanorice. Both the longitudinal and transverse plasmon resonances progressively redshift as the shell thickness decreases. The longitudinal plasmon mode exhibits a more sensitive structural dependence of its optical resonance on the shell thickness than the transverse plasmon.

It was found that both the longitudinal and transverse plasmons of nanorice redshift as the refractive index of solvents increases with a linear dependence of plasmon wavelength on refractive index [177]. Although the transverse plasmon is relatively insensitive to the local environment, the longitudinal nanorice plasmon resonance wavelength is highly sensitive to the surrounding dielectric medium, with LSPR sensitivity as high as over 800 nm per refractive index unit. The LSPR sensitivity of the longitudinal plasmon is maintained as shell thickness is varied, while that of the transverse plasmon decreases as shell thickness increases. Such environmental sensitivity of the nanorice plasmons holds great potential for monitoring local environmental changes during chemical and biological processes.

The sphere–cavity model for spherical nanoshells [156, 157] can be generalized to describe the plasmon resonances of nanorice as the result of the hybridization between plasmon modes of a solid prolate spheroid and an ellipsoidal cavity inside a continuous metal [152, 177]. For a solid prolate spheroidal particle of aspect ratio (semimajor/semiminor axis) = $\coth\alpha$, which consists of a metal with an electron density corresponding to a bulk plasmon frequency ω_B and a polarizability of ε_S (immersed in a dielectric with permittivity ε_E), the energies of the plasmon modes take the form

$$\omega^2_{S,lm}(\alpha) = \omega^2_B \frac{P'_{lm}(\cosh\,\alpha)Q_{lm}(\cosh\,\alpha)}{\varepsilon_S P'_{lm}(\cosh\,\alpha)Q_{lm}(\cosh\alpha) - \varepsilon_E P_{lm}(\cosh\,\alpha)Q'_{lm}(\cosh\,\alpha)} \tag{1.17}$$

For a prolate dielectric cavity of aspect ratio $\coth\alpha$ filled with a dielectric medium of permittivity ε_C in the same metallic material, the plasmon energies are

$$\omega^2_{C,lm}(\alpha) = \omega^2_B \frac{P_{lm}(\cosh\,\alpha)Q'_{lm}(\cosh\,\alpha)}{\varepsilon_S P_{lm}(\cosh\,\alpha)Q'_{lm}(\cosh\alpha) - \varepsilon_C P'_{lm}(\cosh\,\alpha)Q_{lm}(\cosh\,\alpha)} \tag{1.18}$$

Figure 1.22d shows the dependence on aspect ratio of the transverse and longitudinal plasmon resonances of a Au nanorod, modeled as a prolate spheroid (Eq. 1.17), and that of an elliptical dielectric cavity embedded in an infinite Au volume (Eq. 1.18). Each of these nanostructures supports longitudinal and transverse plasmon resonances strongly dependent upon aspect ratio, where an aspect ratio of 1 corresponds to the spherical particle and cavity case. The cavity plasmon described here corresponds to a void filled with a dielectric medium of dielectric constant $\varepsilon_C = 9.5$, that of hematite. For this large dielectric function, the cavity is strongly redshifted to energies lower than the solid spheroid plasmon resonance. As the aspect ratio increases, the energies of the longitudinal plasmon of the spheroid and the transverse plasmon of the cavity decrease, while the longitudinal plasmon of the cavity and the transverse plasmon of the spheroid increase. Varying the aspect ratio of the cavity and spheroid shifts the relative energy of the cavity and spheroid parent plasmon modes, which ultimately affects the way in which the cavity and spheroid plasmon states hybridize in the nanorice geometry.

In Fig. 1.22e and f, we show how the nanorice resonances vary as the aspect ratio of the core is varied, while the outer-shell aspect ratio is held constant at 4.575 for the longitudinal and transverse excitations, respectively. As the aspect ratio of the

core is decreased, the hybridization between the cavity and spheroid modes becomes progressively stronger, resulting in larger energy gaps between the bonding and antibonding plasmon modes. The lower-energy bonding plasmon modes of nanorice are much more sensitive to the core and shell dimensions than the antibonding plasmon modes for both the longitudinal and the transverse cases. The nanorice plasmon modes have a significantly increased geometric sensitivity and can be tuned across a broader spectral range than the parent solid spheroid and cavity plasmon modes. In particular, the bonding plasmon extends toward zero frequency in the thin shell limit, for both the transverse and longitudinal cases. For longitudinal polarization, the nature of the bonding plasmon is solid particle-like and the antibonding mode is cavity-like. For transverse polarization, the situation is reversed. Since the solid spheroidal plasmons have a much larger induced dipole moment and couple more strongly to incident light than cavity-like plasmons, the extinction cross section for longitudinal polarization is dominated by the bonding nanorice plasmon and, for transverse polarization, the spectrum is dominated by the antibonding plasmon mode. The difference in LSPR sensitivity of the longitudinal and transverse nanorice plasmons can also be explained in the context of the plasmon hybridization model, where the spheroid-like plasmon resonance has increased sensitivity to changes in its dielectric environment, while a cavity-like resonance has greater sensitivity to changes in the dielectric properties within the nanoparticle core [157].

The asperities of a nanorice particle support very strong local field intensity enhancements at wavelengths corresponding to the longitudinal plasmon resonance of nanorice [177]. The field enhancements are several times larger than those reported for nanofabricated bowtie junctions [178] and those measured in scanning probe junctions [179] and are similar in magnitude to the localized plasmon resonant "hot spots" occurring in junctions between metallic nanoparticles [158]. The nanorice local fields should give rise to intense SERS enhancements with the added advantage that the hot spots are completely open to the surrounding medium in this geometry. From this point of view, each nanorice particle can potentially serve as a stand-alone, optically addressable nanoscale substrate for surface-enhanced spectroscopies. Moreover, since the enhanced near-field intensities can extend several tens of nanometers from the surface of the nanorice, these particles may exhibit unique advantages in the spectroscopic sensing and characterization of large biomolecules, such as proteins and DNA, biological samples, or materials placed directly adjacent to the nanoparticles.

8 Other Metallic Nanostructures with Geometrically Tunable Optical Properties

Besides nanorods and nanoshells, a series of other nanoparticle geometries have also been found to possess geometrically tunable optical properties. Here we provide several representative examples, including nanoprisms, nanopolyhedrons, nanostars, and nanocages, to highlight how the geometric parameters profoundly impact the optical responses of these anisotropic nanostructures.

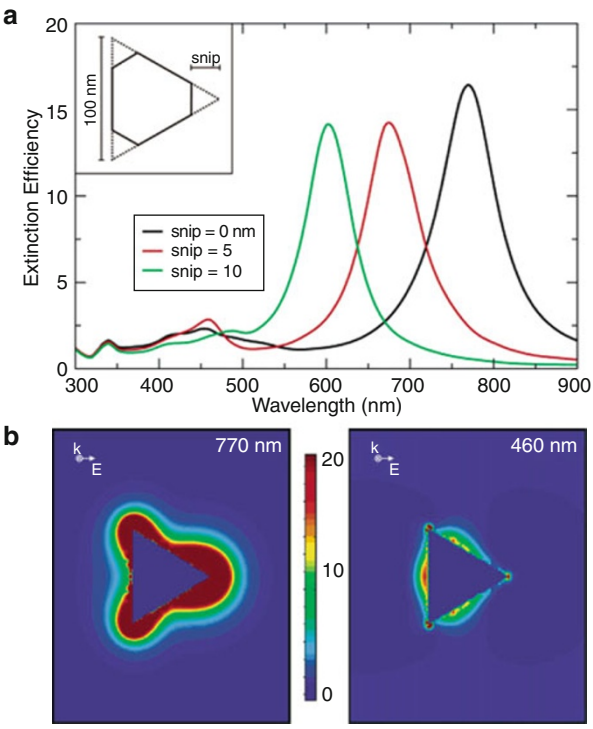

Fig. 1.23 (**a**) Orientation-averaged extinction efficiency for trigonal prisms based on a 100-nm edge dimension with snips of 0, 10, and 20 nm. The *inset* shows the shape of a snipped prism. The prism thickness is 16 nm. (**b**) E-field enhancement contours external to the Ag trigonal prism, for a plane that is perpendicular to the trigonal axis and that passes midway through the prism (Reprinted with permission from Ref. [56]. Copyright 2003 American Chemical Society)

8.1 Nanoprisms

Nanoprisms or triangular nanoplates display a wide range of geometrically tunable optical features [180]. Triangular nanoprisms contain three sharp vertices that contribute significantly to their optical properties. However, experimentally fabricated metallic triangular nanoprisms typically exhibit varying degrees of tip truncation. The LSPR band position of nanoprisms is essentially determined by the tip sharpness, the edge length, and the aspect ratio (lateral dimension/thickness). Sharper tips, larger edge lengths, and higher aspect ratios generally give rise to more redshifted resonances, while round and truncated tips and low aspect ratios result in oppositely blueshifted bands.

The LSPRs of triangular Ag nanoprisms have been simulated by Schatz and coworkers using DDA method [56, 181]. For the perfect triangular prism as shown in Fig. 1.23a, the extinction spectrum consists of three LSPR bands, a long wavelength peak at 770 nm (in-plane dipole), a weaker peak at 460 nm (in-plane quadrupole), and a small but sharp peak at 335 nm (out-of-plane quadrupole). A dipole plasmon resonance can be described as the electron cloud surrounding the nanoparticle moving either parallel or antiparallel to the applied field. For a quadrupole mode, half of the cloud moves parallel and half moves antiparallel. Since a nanoprism is anisotropic with respect to the propagation and polarization of

the incident light, both in-plane and out-of-plane excitation lead to dipole and quadrupole resonances; however, the out-of-plane dipole resonance at 430 nm is not resolved because it is a very broad resonance. Interestingly, the red-most peak is very sensitive to snipping, with the 20-nm snipped prism giving rise to a peak that is blueshifted by 100 nm as compared to the perfect triangular nanoprism, while the other peaks at shorter wavelengths are much less sensitive to snipping. As shown in Fig. 1.23b, the maximum enhancement for the dipole resonance is located around the tips, while for the quadrupole resonance, the regions of significant field enhancements are largely confined at the sides.

The experimentally fabricated nanoprisms typically have sufficiently large edge lengths of sub-100 nm and high aspect ratio over 10 and therefore exhibit both dipole and quadrupole plasmon resonances that shift in frequency as a function of nanoprism size, shape, and dielectric environment. With spherical particles smaller than 100 nm, quadrupole and dipole plasmon resonances are not distinguishable from each other as shown in Fig. 1.4; however, in an anisotropic nanoprism with similar size, these modes oscillate at markedly different frequencies (generally separated by 100–400 nm) and can be resolved experimentally for nanoprisms of both Au and Ag [17, 18, 182].

Ag nanoprisms have been synthesized with tight control over their aspect ratio in relatively high yield through photochemically induced growth [17, 182–185] or thermal reduction in organic solvents [19, 20, 186], while Au nanoprisms have been mostly fabricated through solution-phase seed-mediated growth approaches [18, 187–190]. In the photochemical synthesis, a variety of radiation wavelengths can be used to selectively tailor the architectural parameters of the resulting nanoprisms, such as thickness and edge lengths, and thereby to fine-tune the optical properties of nanoprisms (Fig. 1.24) [184]. In the solution-phase chemical synthesis of Au and Ag nanoprisms, the particle geometry can be tuned by adjusting a whole set of experimental conditions, such as reducing agents, reaction media, temperature, and surfactants. For more details about the fabrication of Ag and Au nanoprisms and mechanisms of nanoprism formation under various conditions, the readers are recommended to read a recently published review article by Mirkin and coworkers [180].

Ag nanoprisms may also undergo post-fabrication morphological changes under various conditions, introducing interesting modifications to the LSPRs. Therefore, post-fabrication treatments provide an alternative way to fine-tune the optical properties of Ag nanoprisms. The optical properties of Ag nanoprisms can be precisely tuned over a wide spectral range through a process of shape reconstruction induced by UV irradiation, in which the morphology of the nanoparticles is changed from thin triangular nanoprisms to thick round nanoplates [191]. It has been recently reported that Ag nanoprisms may also undergo an interesting sculpturing process due to chemical etching by halide ions [192–194]. Thermal treatments of Ag nanoprisms can also give rise to interesting reshaping of Ag nanoprisms, which results in systematic evolution of LSRPs [195]. The blueshift of LSPRs is a direct consequence of both tip truncation and size reduction during the thermal treatments.

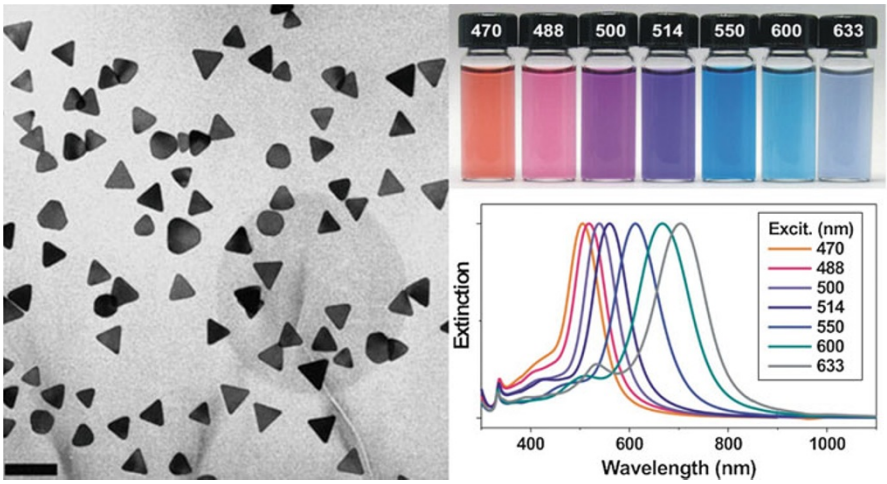

Fig. 1.24 TEM image of Au nanoprisms (*left*), extinction spectra, and corresponding solutions of Ag nanoprisms with varying edge length (*right*). Labeled vial and spectra numbers correspond to the wavelength of irradiation used to prepare the nanostructures (Reprinted with permission from [184]. Copyright 2007 John Wiley & Sons, Inc)

8.2 Nanopolyhedra

Controlling nanocrystal shapes in the mesoscopic size regime provides an elegant strategy for optical tuning. Whereas highly symmetric spherical particles within the quasi-static limit exhibit a single LSPR peak, anisotropic multifaceted nanoparticles such as cubes, bipyramids, and other polyhedra exhibit multiple scattering peaks in the visible and NIR regions due to their mesoscopic sizes beyond the quasi-static limit and highly localized charge polarizations at corners and edges.

Yang and coworkers systematically investigated LSPRs of metallic nanopolyhedrons both at the ensemble and single-particle levels [196] Monodisperse colloidal solutions of Ag nanocrystals with regular polyhedral shapes were synthesized in a highly controllable manner using the polyol method, where the metal salt is reduced by hot pentanediol at near-reflux temperature in the presence of PVP as the capping polymer. Silver nitrate and PVP were dissolved separately and injected into the system periodically, and specific polyhedral shapes can be obtained in high yield depending on how long the sequential additions are continued. Figure 1.25 shows the differences in LSPR modes for cubic, cuboctahedra, and octahedral nanoparticles, all of which exhibit highly complex plasmon signatures as a result of their geometric anisotropy.

8.3 Nanostars

Metallic nanostars are multipointed, branched metal nanoparticles, each of which may exhibit highly complex multipeaked extinction spectral line shapes [197].

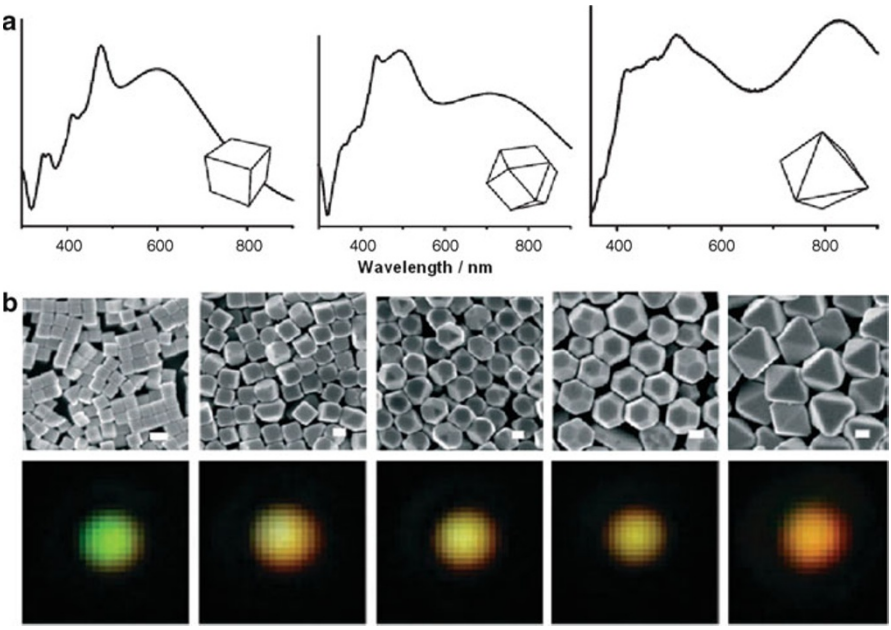

Fig. 1.25 (**a**) UV–visible spectra of colloidal dispersions of Ag nanocubes, cuboctahedra, and octahedra. (**b**) SEM and real color images taken with a digital camera displaying the different colors arising from plasmon-mediated scattering. Each spot corresponds to the light scattered from a single crystal. From *left to right*: *cube*, *truncated cube*, *cuboctahedron*, *truncated octahedron*, and *octahedron*. Scale bars: 100 nm (Reprinted with permission from Ref. [196]. Copyright 2006 John Wiley & Sons Inc)

For branched Au nanocrystals or nanostars, the precise control over particle morphology is often challenging because the number of branches or pods can vary within each preparation [25, 104, 198–201], which results in formation of mixtures of monopods, bipods, tripods, tetrapods, and other multipods in each sample. To synthesize Au nanostars with a specific number of branches, the utilization of structurally well-defined and multi-twinned Au nanoparticles, such as nanorods, bipyramids, and decahedra, is necessary as templates or seeds for the nanostar growth. Xia and coworkers [202] recently reported the facile synthesis of Au nano-hexapods by seeded growth with controllable arm lengths. During the seed-mediated growth, $HAuCl_4$ was reduced by *N*,*N*-dimethylformamide (DMF) in water in the presence of single-crystalline Au octahedra. The newly formed Au atoms preferentially nucleated and grew from the six vertices of an octahedral seed, leading to the formation of nano-hexapods. The LSPR peaks of the resultant Au nano-hexapods redshifted from the visible to the NIR depending upon the lengths of the arms, which could be controlled by varying the amount of $HAuCl_4$, the temperature, or both. The preparation and optical properties of penta-branched Au nanostars obtained using seed-mediated method have also been reported recently [26, 203–206]. The extinction spectra of the colloidal nanostars taken at

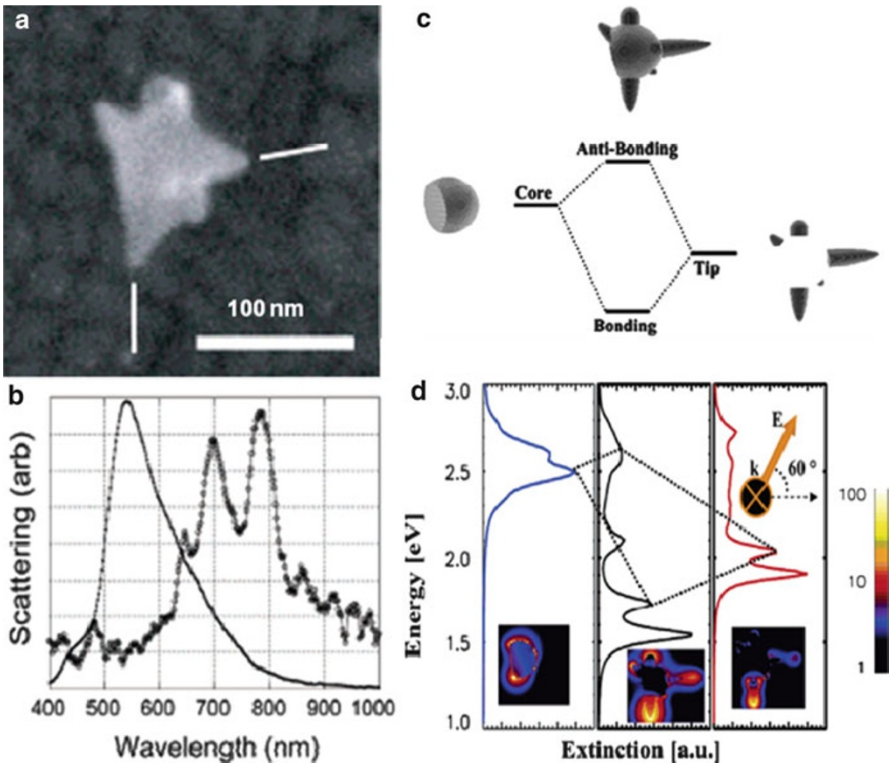

Fig. 1.26 (**a**) SEM image and (**b**) single-particle dark-field light-scattering spectrum (*open circles*) of a Au nanostar. The scattering spectrum of a 100-nm Au colloid is also plotted (*points*). (**c**) The plasmon hybridization picture of Au nanostar LSPRs. (**d**) The *left panels* show the extinction spectra of the individual core. The *right panels* show the spectra of the tips. The *middle panels* show the extinction spectra of the interacting nanostar system (Reprinted with permission from Refs. [26] and [207]. Copyright 2006 and 2007 American Chemical Society)

different time points demonstrate that there are two distinct peaks which correspond to short-wavelength transverse absorption band arising from the formation of fully developed side branches and redshifted longitudinal band due to the elongation of the developed branched nanocrystals.

To further shed light on the structure–property relationship of nanostars, Hafner and coworkers [26] studied the optical properties of individual Au nanostars at single-nanoparticle level. They used commercially available 10-nm-diameter Au colloids as the seed to produce star-shaped nanoparticles under the exact growth conditions suitable for nanorods in the presence of CTAB. Their single-particle light-scattering data show that nanostars have multiple plasmon resonances resulting in polarization-dependent scattering, which correspond to different tips of the star-shaped structure (Fig. 1.26a and b). The plasmon resonances are extremely sensitive to the local dielectric environment changes and that shows great promise for the nanostars to be used as LSPR sensors. Nordlander and

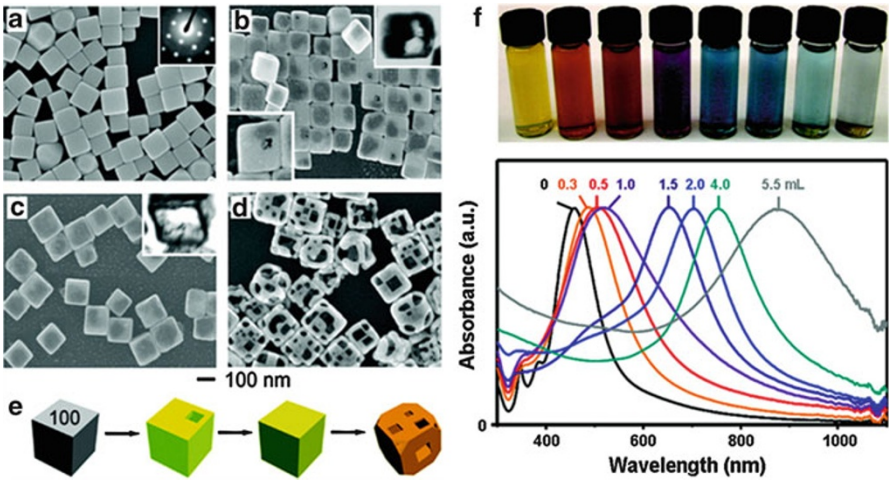

Fig. 1.27 SEM images of (**a**) Ag nanocubes and (**b–d**) Au–Ag porous nanocages. (**e**) Illustration summarizing morphological changes. (**f**) *Top panel*, vials containing Au nanocages prepared by adding different volumes of $HAuCl_4$ solution. Lower panel, the corresponding extinction spectra of Ag nanocubes and Au nanocages (Adapted with permission from Ref. [208]. Copyright 2008 American Chemical Society)

coworkers [207] interpreted the nanostar plasmons as a result of plasmon hybridization between the core and tips of the nanoparticle (Fig. 1.26c and d). The nanostar core serves as a nanoscale antenna, dramatically increasing the excitation cross section and the electromagnetic-field enhancements of the tip plasmons.

8.4 Nanocages

Metallic nanocages are a class of interesting photonic nanostructures possessing hollow interiors and porous walls [208]. They can be prepared in high yield through a remarkably simple galvanic replacement reaction between solutions containing metal precursor salts and metallic nanoparticle templates. Regarding the preparation of Au-based nanocages, Ag nanocubes prepared by polyol reduction [209, 210], can serve as a template for the galvanic reactions during which the produced Au is confined to the Ag nanocube surface, growing on it and adopting its morphology. Concurrent with this deposition, the interior Ag is oxidized and removed, together with alloying and dealloying, to produce hollow and, eventually, porous nanocage structures (see Fig. 1.27a–e). This approach is versatile and can be extended to the fabrication of multiple-walled Au nanorattles or nanotubes [211]. In addition to Au-based structures, switching the metal salt precursors to Na_2PtCl_4 and Na_2PdCl_4 allows for the preparation of Pt- and Pd-containing nanocages, respectively [212, 213].

Accompanying the compositional and morphological changes induced by the galvanic replacement reactions is the evolution of LSPRs of Au nanocages. The upper panel of Fig. 1.27f shows a picture of vials containing Au nanocages prepared by reaction between Ag nanocubes (edge length ≈ 40 nm) and different volumes of $HAuCl_4$ solution (0.1 mM) [211, 214]. As the photograph and corresponding extinction spectra (Fig. 1.27f, lower panel) indicate, the LSPR peak position of the Au nanocages is tunable throughout the visible and NIR. This observation makes Au nanocages attractive for colorimetric sensing and biomedical applications. The relative intensity of the scattering and absorption cross sections of Au nanocages can be tuned by varying their size. DDA simulations indicate that when Au nanocages are small (edge length<45 nm), light absorption predominates; however, light scattering prevails with larger Au nanocages [214]. Thus, one must consider their size and the magnitude of their scattering and absorption cross sections, in addition to LSPR position, when engineering nanocages for a specific application. The tunable LSPRs of nanocages hold great promise to biomedical applications. For example, Xia and coworkers have explored the use of Au nanocages as contrast enhancement agents for both optical coherence tomography and photoacoustic tomography [215–217], with significantly improved performance observed in each case.

9 Multi-nanoparticle Systems

In this section, we would like to expand our discussions to the geometrically tunable optical properties of more complicated multi-nanoparticle systems composed of multiple nanoparticles that are in close proximity to each other. The plasmonic interactions between neighboring nanoparticles give rise to further redshifted lowest-energy plasmon resonance, further increased complexity of extinction spectral line shapes, and significantly enhanced electric fields in the interparticle junctions [218]. The multi-nanoparticle systems possess more geometric parameters that one can adjust to further fine-tune the optical responses over a broader spectral range and, thus, may exhibit superior optical properties in comparison to individual nanoparticle building blocks. One striking example observed by colloidal chemists is the dramatic color change of noble metal colloids when a dilute suspension of nanoparticles forms nanoparticle aggregates upon the introduction of ions, such as Cl^-, or molecular linkers, such as DNA [52, 219–222]. When Au or Ag nanoparticles begin to aggregate, they form clusters of nanoparticles, and their extinction spectrum acquires a new band that is redshifted significantly from the extinction band of the isolated nanoparticles. In addition, the local electric fields can be enormously enhanced in the nanoscale gaps between the adjacent nanoparticles upon the excitation of the "aggregate" plasmons, providing "hot spots" for surface-enhanced spectroscopies. It is essentially these features that have been attributed to the enormous SERS enhancements reported for random colloidal aggregates, approaching single-molecule sensitivity for certain molecules [51, 52, 223–228].

The interesting optical properties of multi-nanoparticle systems can be essentially interpreted as results of plasmon coupling between individual nanoparticles that are in close proximity to each other [159, 218], in analogy to the hybridized molecular orbitals in a polyatomic molecule. In this context, individual nanoparticles can be regarded as artificial atoms, while a multi-nanoparticle system can be regarded as an artificial molecule. Plasmon hybridization model allows us to express the fundamental plasmon modes of these multiparticle systems as linear combinations of the primitive plasmons supported by individual nanoparticles. The geometry of individual constituent nanoparticles, the geometric arrangements of the nanoparticles, and the distance between adjacent nanoparticles are all key factors that profoundly impact the synergistic far-field and near-field optical properties of a multi-nanoparticle system. Halas and Nordlander [218] recently published a comprehensive review article on plasmons in strongly coupled metallic multi-nanoparticle systems, and the readers are strongly encouraged to read this review and the references cited therein to get a more complete and thorough understanding on this topic. In this section, we would like to focus on three representative systems, nanoparticle dimers, nanoparticle oligomers (clusters composed of a finite number of nanoparticles), and infinite nanoparticle arrays, to highlight how the plasmon coupling in multi-nanoparticle systems gives rise to a whole set of interesting optical properties that are exploitable for widespread applications, such as molecular sensing and surface-enhanced spectroscopies.

9.1 Nanoparticle Dimers

The simplest geometry of multi-nanoparticle systems is a pair of directly adjacent, interacting nanoparticles known as a nanoparticle dimer. The importance of the nanoparticle dimer geometry was first recognized from a theoretical point of view in the early 1980s [229], stimulating further theoretical investigations of this geometry ever since [158, 230–232]. In spite of the challenges associated with large-scale and high-yield synthesis of nanoparticle dimers, the optical properties of nanoparticle dimers have been studied in great detail at single-nanoparticle level using dark-field microscopy [233, 234]. The results of single-particle light-scattering measurements have been directly compared to electrodynamics simulations based on which detailed understanding of the plasmon coupling in nanoparticle dimers has been developed.

Figure 1.28a shows a diagram illustrating the plasmon coupling of a Au nanoparticle homodimer [158]. The plasmon hybridization between the two nanoparticles results in an increased redshift of the bonding $l = 1$ dimer mode with decreasing interparticle distance (Fig. 1.28b). This behavior is characteristic of a dimer excited by light polarized along its interparticle axis. For light polarized perpendicular to the dimer axis (Fig. 1.28c), interparticle coupling is minimal, and a small blueshift of the antibonding mode, which is optical "bright," is observed as the interparticle distance decreases, while the bonding plasmon mode is optically "dark."

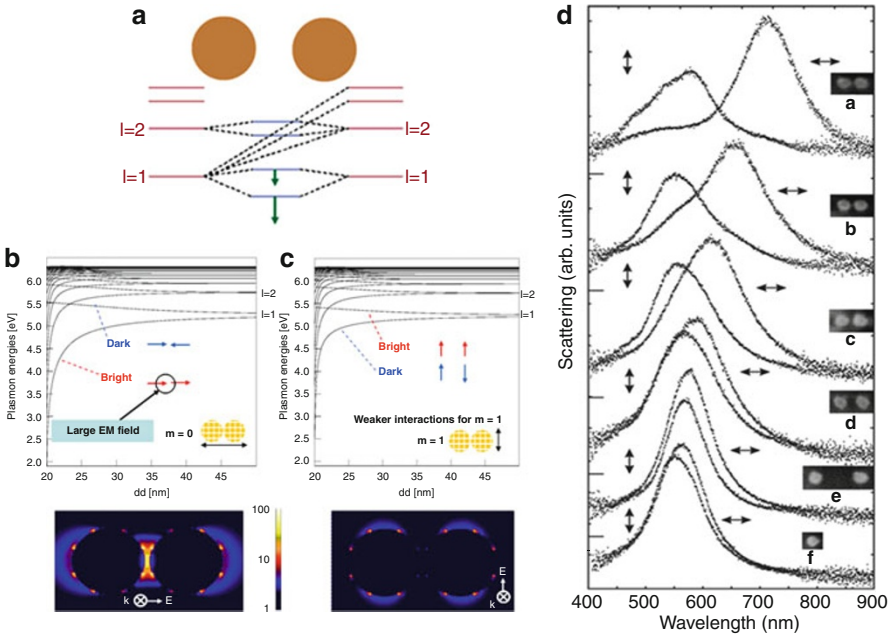

Fig. 1.28 (**a**) Schematic diagram of the dimer system and calculated plasmon energies versus dimer separation for a homodimer of Au nanospheres for (**b**) parallel and (**c**) perpendicular polarizations. (**d**) Dark-field spectra and SEM micrographs from isolated nanoparticle pairs with varying separations in parallel and perpendicular polarization, as indicated by *arrows*. (*Panels A–C*: adapted with permission from Ref. [158]. Copyright 2004 American Chemical Society. *Panel D*: reprinted with permission from Ref. [242]. Copyright 2005 American Chemical Society)

It is of particular interest that the local electric fields inside the interparticle gaps can be enormously enhanced when the bonding dipolar plasmon mode is optically excited for the polarization parallel to the dimer axis (Fig. 1.28b). Such local field enhancements in the nanoparticle junctions can fundamentally interpret the "hot-spots" effects in nanoparticle aggregates that are exploitable for surface-enhanced spectroscopies. Halas and coworkers have directly compared the SERS performance of individual nanoparticles vs. nanoparticle dimers [235]. They found that nanoparticle dimers exhibit much larger SERS enhancement than the individual nanoparticle primarily due to the hot spots in the interparticle junctions. Similar "hot-spots" effects have also been observed in dimers of Ag nanospheres [236], pairs of Ag nanocubes [237, 238], and metallic bowtie nanostructures (a nanoparticle dimer composed of two triangular nanoplates in close proximity with sharp tips directly pointing to each other) [239–241]. Figure 1.28d shows the experimentally measured scattering spectra from individual pairs of Ag nanoparticles with varying interparticle gaps [242]. The experimentally observed dependence of the dimer plasmon modes on the interparticle distance and dimer orientation with respect to the incident light polarization are in good agreement with the theory.

For a nanoparticle heterodimer, both the bonding and antibonding modes for both polarizations can be excited by the incident light because even for the hybridized plasmon modes in which the two dipole modes of individual nanoparticles are antiparallelly aligned, there is still a net dipole moment due to the asymmetry of the system. Halas and coworkers [233] have systematically studied the optical responses of plasmonic heterodimers and carefully correlated their experimental results with electrodynamics simulations. While a plasmonic homodimer can support both bright and dark modes, symmetry breaking relaxes selection rules and enhances coupling between all of the plasmon modes of a heterodimer nanostructure. In the case of two adjacent, mismatched nanoparticles, this allows modes with different characteristics, such as angular momentum or linewidth, to interact strongly with each other especially in the small gap regime, giving rise to more complicated spectral line shapes and asymmetric plasmon splitting. These interactions are a strong function of interparticle distance and relative energy level of primitive plasmons of the individual nanoparticles, resulting in energy shifts and avoided crossings of the plasmon modes as the constituent nanoparticles coalesce into the dimer structure. Interactions between broad and narrow resonant modes can occur, giving rise to a Fano resonance with its characteristically asymmetric line shape in nanoparticle heterodimer systems [233, 243].

Altering the symmetry of individual constituent nanoparticles inside a dimer will also introduce dramatic modifications to the optical properties of the dimer structure. For example, the shape anisotropy of metallic nanorods leads to different possible orientations within a dimer, resulting in different orientational modes of plasmon coupling [244–248]. Coupling of the nanorod longitudinal modes leads to bonding and antibonding interactions when the dimer is arranged end-to-end or side-to-side. Many other possible dimer geometries, including L-shaped and T-shaped dimers as well as dimers laterally and longitudinally displaced with respect to one another, may also form taking into consideration of the character of anisotropy.

Because of the strong dependence of the dimer plasmons on the interparticle distance, one can use nanoparticle dimers to construct “plasmon rulers” to measure distance changes over nanometer-length scale [249–253]. By using molecules as the linker between the two nanoparticles, the conformational changes of the molecular linker can be probed in real time simply based on the plasmon shift as the interparticle distance varies. Alivisatos and coworkers developed a single-molecule version of plasmon-based colorimetric sensing strategy using individual nanoparticle dimers as plasmon rulers to probe the DNA hybridization by monitoring the plasmon shift under a dark-field optical microscope [249]. Later, they further developed a DNA-linked nanoparticle dimer that can be used to probe the conformational dynamics of protein–DNA complexes and the kinetics of DNA digestion at single-molecular level [252]. In comparison to other nanoscale molecular rulers, such as fluorescence resonance energy transfer (FRET) [254], plasmon rulers have several unique advantages, such as high photostability of the probes (no blinking), long-lasting signals (no photobleach), and simplicity of instrumentation (colorimetric sensing based on dark-field scattering).

9.2 Nanoparticle Oligomers

The fundamental principles of plasmon hybridization described in the nanoparticle dimer systems can be further extended to more complicated nanoparticle oligomer structures. Just as molecular orbital theory can be applied to complex, polyatomic molecules, there has been interest in extending coupled plasmon systems beyond the plasmonic dimers to multi-nanoparticle systems. Because of the invariance of the interactions through symmetry transformations for a specific structure, group theory may be applied quite naturally to the analysis of plasmon modes of multi-nanoparticle systems with various symmetries. For example, symmetric linear combinations of plasmons corresponding to the underlying symmetry of the system can be used to interpret and classify the modes of a triangularly arranged nanosphere trimer (group D_{3h}) and squarely arranged quadrumer (group D_{4h}) [255]. The linear combinations of individual nanoparticle plasmons can be used to predict which modes have a dipole moment for a given polarization, resulting in a significant simplification of the problem.

Breaking the symmetry of a nanoparticle trimer will introduce interesting modifications to the plasmon coupling between the constituent nanoparticles. Chuntonov and Haran [256] followed the evolution of LSPR spectra of plasmonic trimers, assembled from equal-sized Ag nanoparticles, as gradual geometric alterations break their structural symmetry. The spectral modes of an equilateral triangle, the most symmetric structure of a trimer (D_{3h}), are degenerate. This degeneracy is lifted as the symmetry is lowered to C_{2v} and eventually to $D_{\infty h}$ as one of the vertex angles is gradually opened. This symmetry breaking leads to a subtle transition between bright and dark modes. The evolution of the plasmon modes across different symmetry groups was monitored through the scattering spectra of the symmetry-broken trimers, and the results can be well explained with the aid of group correlation tables and plasmon hybridization theory.

As the cluster size further increases, the spectral line shape of the plasmonic oligomers becomes increasingly more complicated due to the interaction and hybridization of more multipolar plasmon modes within these nanostructures. Highly asymmetric spectral line shapes due to pronounced Fano resonances have been observed in lithographically fabricated or chemically self-assembled planar symmetric plasmonic nanoparticle oligomers, such as quadrumers [257], pentamers [258] and heptamers [259–262]. These Fano resonances observed in planar plasmonic oligomers arise from interactions between a superradiant "bright" mode and a subradiant "dark" mode in a nanostructure, and they are characterized by a pronounced, asymmetric dip in the scattering spectra. As shown in Fig. 1.29, a self-assembled Au nanoshell heptamer cluster (one nanoparticle in the center of a six nanoparticle ring) on a planar substrate exhibits pronounced Fano resonance line shape in their extinction spectrum [259]. This Fano resonance line shape has also been observed in lithographically fabricated plasmonic heptamers by Hentschel et al. [261, 262] who symmetrically studied the effects of interparticle spacing and geometric arrangement on the frequency and line shape of the Fano resonance of the heptamers. The Fano resonances observed in plasmonic oligomers

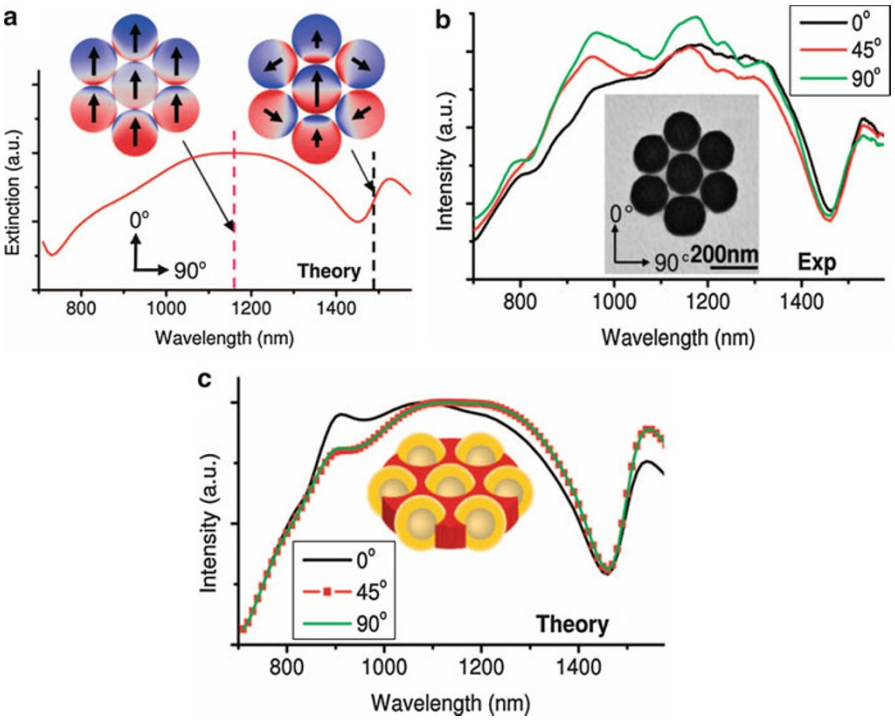

Fig. 1.29 Fano-resonant behavior of a plasmonic nanoshell heptamer. (**a**) Calculated extinction spectrum and charge density plots for a heptamer excited at normal incidence with a 0° orientation angle. (**b**) TEM image and spectra of a heptamer at three different incident electric-field orientation angles. (**c**) Calculated scattering spectra for a heptamer with a geometry matching that in (**a**), for the three orientation angles in (**b**) (Reprinted with permission from Ref. [259]. Copyright 2010 American Association for the Advancement of Science)

have relatively narrow linewidth and high sensitivity to the surrounding medium and thus are very attractive for LSPR sensing due to the great figure of merit (LSPR shift/linewidth).

9.3 Infinite 1D and 2D Nanoparticle Arrays

Periodic 1D and 2D nanoparticle arrays with homogeneous nanoparticle sizes and shapes as well as regular interparticle separations provided important geometries for far-field and near-field plasmon coupling to occur over a macroscopic area [263–268]. In nanoparticle arrays with the interparticle distance comparable to the LSPR wavelength of the isolated nanoparticles, far-field diffractive plasmon coupling leads to a spectral narrowing of the collective plasmon response [269, 270]. Hickes et al. investigated the line shape of an array of Ag nanoparticle chains and observed that the long wavelength shoulder in scattering spectra significantly

gained in intensity and narrowed spectrally for interparticle distances comparable to the resonance wavelength of an isolated nanoparticle [270]. Sharp, coherently coupled plasmon bands in 2D Ag nanoparticle arrays have also been observed by Chumanoc and coworkers [271, 272]. Simulations using the coupled dipole approximation have also shown that the bandwidth of the collective plasmon mode induced by far-field diffractive coupling can be smaller than 1 nm, which is important for applications such as LSPR sensing since the sensitivity improves for narrower linewidths [273].

Near-field plasmon coupling in linear nanoparticle chains has attracted significant attention because the plasmon modes are no longer localized on the individual nanoparticles but can propagate along the chain axis, which makes it possible to direct energy along a chain of nanoparticles [274–277] and allows for electromagnetic energy transport in waveguide structures smaller than the diffraction limit of the incident light [278–282]. It is very interesting to note that the characteristics of bending light around corners or splitting it into two or more branches can be achieved for nanoparticle arrays with complex geometries, such as T-shaped structures. Many research groups found that an increasing redshifted longitudinal plasmon resonance of the nanoparticle chains can be observed as increasing the number of nanoparticles from a dimer to a periodic linear chain while keeping the interparticle distance constant [283–285].

The synergistic optical properties of a 2D infinite nanoparticle array are sensitively dependent on the interparticle spacing. Yang and coworkers developed a Langmuir–Blodgett self-assembly approach for the fabrication of Ag nanoparticle arrays with fine-controlled interparticle spacing [286–288]. They found that when the interparticle spacing is relatively large with respect to individual particle size, the arrays exhibit plasmonic responses that are similar to individual nanoparticles due to lack of interparticle plasmon coupling. As the interparticle spacing gradually decreases, the plasmon coupling between nanoparticles becomes progressively stronger, giving rise to dramatic changes in the extinction spectral line shapes. As the interparticle spacing further decreases to a regime where the nanoparticles are almost touching, the optical properties become similar to those of a macroscopically continuous metallic film.

Tiny but nonzero interparticle gaps in 2D nanoparticle arrays are critical for the emergence of large local field enhancements in the interparticle junctions that are exploitable for surface-enhanced spectroscopies as demonstrated by several groups [289–293]. For example, Halas and coworkers developed a convenient and cost-effective chemical self-assembly approach to highly ordered Au nanosphere arrays with sub-10-nm interparticle spacing [291]. These sub-10-nm nanogaps between adjacent nanoparticles have been proved to be very crucial for reproducible, large, averaged SERS enhancements on the order of 10^8 for nonresonant molecules. 2D arrays of metallic nanoshells have recently been found to possess ideal properties as a substrate for combining SERS and surface-enhanced infrared absorption (SEIRA) spectroscopies [294]. For sub-10-nm interparticle distances, the multipolar plasmon resonances of individual nanoshells hybridize and form redshifted bands, a relatively narrow band in the NIR originating from quadrupolar nanoshell

resonances enhancing SERS and a very broad band in the mid-infrared (MIR) arising from dipolar resonances enhancing SEIRA. The resulting nanoshell arrays possess "hot spots" in the interparticle junctions that can enhance Raman scattering by a factor of 10^8–10^9 at near-infrared wavelengths and simultaneously provide broadband mid-infrared hot spots that can enhance infrared absorption by a factor of 10^4 on the same substrate [294]. Nordlander and coworkers [295] theoretically studied the origin of the interesting optical properties of metal nanoshell arrays. They systematically studied the evolution of optical properties from nanoshell oligomers to infinite nanoshell 2D arrays as the number of nanoshells gradually increases. They proposed that the large field enhancements in the MIR and at longer wavelengths are due to the lightning-rod effects and are well described with an electrostatic model.

10 Concluding Remarks

Over the past two decades, significant progress has been made on the controllable fabrication of metallic nanoparticle in various geometries through both top-down clean-room techniques and chemical bottom-up approaches. Tight control over particle geometries enables one to fine-tune the plasmon-dominated optical properties of metal nanoparticles or nanoparticle assemblies over broad spectral ranges. Classical electromagnetic theory and numerical electrodynamics simulations as well as plasmon hybridization model provide a powerful theoretical platform based on which the optical properties of nanostructures with almost arbitrary structural complexity can be predicted and quantitatively analyzed. All these are directly related to our capabilities to tackle grand challenges in energy conversion, photonics, spectroscopies, and biomedicine.

(a) Plasmon-Enhanced Absorption in Photovoltaic Devices
Plasmon-enhanced light absorption in photovoltaic devices has shown significant impact to advances in photovoltaics [296]. For solar cells, three distinct mechanisms for enhancing light absorption could be utilized, which are (1) the scattering from the metallic nanoparticles (far-field effect), (2) the near-field enhancement associated with the localized surface plasmon resonance of the nanoparticles, and (3) excitation of the propagating waveguide modes and direct generation of charge carriers within the thin absorbing or semiconductor layer [297–299]. Thin-film solar cells are currently widely used for low-cost photovoltaics. However, most photovoltaic materials face a trade-off between the necessary thickness for complete optical absorption and the requisite electronic quality for long minority carrier diffusion lengths [300]. The traditional method for enhancing absorption in a solar cell is to employ front or back surface texturing as a way of effective light trapping by increasing its path length [301–303], but this micrometer-sized method is inappropriate for thin-film solar cells because the total film thickness may be only a fraction of a wavelength. On the contrary, the incorporation of plasmonic nanostructures in photovoltaic devices has the potential to overcome this problem of light

trapping due to the ability of surface plasmons to guide and confine light in small volumes [304]. In addition, the feasibility of designing plasmonic nanoparticles with high effective scattering cross sections and geometrically tunable optical properties makes them the optimized candidates for photovoltaic devices. Hence, plasmonic nanoparticles have great potential to revolutionize the photovoltaic industry.

(b) Optical Antennas for Photonic Applications
Optical antennas are devices that convert freely propagating optical radiation into localized energy and vice versa. The control and manipulation of optical fields at the nanometer scale can be achieved using metallic nanoparticles as subwavelength antennas. From the first use of colloidal Au particles for localizing optical radiation on a simple surface proposed by Edward Synge in 1928 [305] to the subsequent experimental demonstrations followed by Dieter Pohl and Ulrich Fischer in 1995 [306] and applications to near-field microscopy [307], optical antennas have attracted tremendous attention. More importantly, LSPRs make optical antennas particularly efficient at selected frequencies [308–310]. Hence, metallic nanoparticles with geometrically tunable LSPRs are very promising candidates for this specific application. With the development of fabrication techniques, a wide range of applications including controlled single-photon sources for quantum information, light harvesting, data storage, nanoscale optical circuitry, and optical imaging beyond 10-nm resolution will emerge [311, 312].

(c) Plasmon-Enhanced Spectroscopies
The quantitative understanding of structure–property relationship of various metal nanoparticles provides critical insights into plasmon-enhanced spectroscopies. The SERS enhancement effect is essentially a result of the creation of plasmons that can transfer energy to the bound molecule through the associated electric field [313–317]. The first discovery of SERS showed that it was possible for a roughed noble metal surface to dramatically enhance the sensitivity and intensity of Raman spectroscopy [318, 319]. The most inspiring aspect is to consider the application of the marked enhancements afforded by SERS to the more challenging goal of single-molecule detection in the biological environment. The search for high-performance SERS substrates has been directly related to our capabilities to engineer the optical properties of metal nanostructures. As already demonstrated in nanoprism arrays fabricated by nanosphere lithography [320] and chemically fabricated metallic nanoshells [131, 132] strong correlation exists between the LSPR frequency of the substrate, the wavelength of excitation laser, and the SERS enhancements achievable on the nanoparticle surfaces. It is believed that as our capability of optimizing the nanoparticle geometries keeps developing, achieving large SERS enhancements at single-molecule sensitivity reproducibly will become possible. Plasmon-enhanced fluorescence (PEF) is another intriguing phenomena associated with plasmonic excitations. It has been known that fluorophore quenching occurs in close proximity to metallic surfaces (typically$<$50 Å) [321], while interesting coupling between the fluorophore and the enhanced

local electric field near the metal structure occurs at longer distances ranging from 5 to 200 nm, resulting in fluorescence enhancements due to increase in both absorption cross section and radiative decay rates. Correlating the plasmonic responses and fluorescence enhancements at single-nanoparticle level has provided crucial insights into how to use plasmonic nanoparticle to optimize the fluorescence behavior of fluorophores that are widely used in bioimaging [322, 323].

(d) Biomedical Imaging and Photothermal Therapy
Metal nanoparticles have widespread applications in biomedicine, such as cancer cell diagnostics [324, 325], and therapeutics [135, 326, 327]. The enhanced radiative properties of metallic nanoparticles derived from the large surface electric fields when interacting with resonant electromagnetic radiation make both the absorption and scattering cross section of orders of magnitude stronger than those of organic molecules. Therefore, metallic nanoparticles can act as exceptionally novel contrast agents for optical detections. The strongly absorbed radiation can be converted efficiently into heat on a picosecond time scale due to electron–photon and photon–photon processes, which is the so-called process of photothermal therapy. This is a promising new medical technology for cancer treatment and affords potential advantages of active targeting at specific cancer site, low toxicity, minimal side effects, and high efficacy.

In summary, this chapter provides a compelling and comprehensive story of geometrically tunable optical properties of various metallic nanoparticles including nanospheres, nanorods, nanoshells, nanoprisms, nanopolyhedrons, nanostars, nanocages, and multi-nanoparticle assemblies. Developing quantitative understanding of the structure–property relationship of these experimentally realizable metallic nanostructures with increasing structural complexity is directly related to our capabilities to further fine-tune their optical properties to optimize a whole set of important physical, chemical, and biomedical processes. Because of the highly diverse nature, we firmly believe that this field will maintain a fast rate of growth and innovation for many years to come. We predict the future of this field to be an innovative and exciting one with great efforts and inspirations devoted by the scientists and engineers from all over the world.

References

1. Burda C, Chen XB, Narayanan R, El-Sayed MA (2005) Chemistry and properties of nanocrystals of different shapes. Chem Rev 105(4):1025–1102
2. Mie G (1908) Articles on the optical characteristics of turbid tubes, especially colloidal metal solutions. Annalen Der Physik 25(3):377–445
3. Faraday M (1857) The bakerian lecture: experimental relations of gold (and other metals) to light. Philos Trans Roy Soc Lond 147:145–181
4. Link S, El-Sayed MA (2003) Optical properties and ultrafast dynamics of metallic nanocrystals. Annu Rev Phys Chem 54:331–366

5. Link S, El-Sayed MA (2000) Shape and size dependence of radiative, non-radiative and photothermal properties of gold nanocrystals. Int Rev Phys Chem 19(3):409–453
6. El-Sayed MA (2001) Some interesting properties of metals confined in time and nanometer space of different shapes. Acc Chem Res 34(4):257–264
7. Xia YN, Halas NJ (2005) Shape-controlled synthesis and surface plasmonic properties of metallic nanostructures. Mrs Bull 30(5):338–344
8. Jain PK, Huang XH, El-Sayed IH, El-Sayed MA (2008) Noble metals on the nanoscale: Optical and photothermal properties and some applications in imaging, sensing, biology, and medicine. Acc Chem Res 41(12):1578–1586
9. Loo C, Lowery A, Halas NJ, West J et al (2005) Immunotargeted nanoshells for integrated cancer imaging and therapy. Nano Lett 5(4):709–711
10. Huang XH, El-Sayed IH, Qian W, El-Sayed MA (2006) Cancer cell imaging and photothermal therapy in the near-infrared region by using gold nanorods. J Am Chem Soc 128(6):2115–2120
11. Link S, El-Sayed MA (1999) Spectral properties and relaxation dynamics of surface plasmon electronic oscillations in gold and silver nanodots and nanorods. J Phys Chem B 103(40):8410–8426
12. Busbee BD, Obare SO, Murphy CJ (2003) An improved synthesis of high-aspect-ratio gold nanorods. Adv Mater 15(5):414–416
13. Nikoobakht B, El-Sayed MA (2003) Preparation and growth mechanism of gold nanorods (nrs) using seed-mediated growth method. Chem Mater 15(10):1957–1962
14. Murphy CJ, Jana NR (2002) Controlling the aspect ratio of inorganic nanorods and nanowires. Adv Mater 14(1):80–82
15. Murphy CJ, Sau TK, Gole A, Orendorff CJ (2005) Surfactant-directed synthesis and optical properties of one-dimensional plasmonic metallic nanostructures. Mrs Bull 30(5):349–355
16. Jana NR, Gearheart L, Murphy CJ (2001) Wet chemical synthesis of silver nanorods and nanowires of controllable aspect ratio. Chem Commun 7:617–618
17. Jin RC, Cao YW, Mirkin CA, Kelly KL et al (2001) Photoinduced conversion of silver nanospheres to nanoprisms. Science 294(5548):1901–1903
18. Millstone JE, Park S, Shuford KL, Qin LD et al (2005) Observation of a quadrupole plasmon mode for a colloidal solution of gold nanoprisms. J Am Chem Soc 127(15):5312–5313
19. Pastoriza-Santos I, Liz-Marzan LM (2002) Synthesis of silver nanoprisms in dmf. Nano Lett 2(8):903–905
20. Sun YG, Xia YN (2003) Triangular nanoplates of silver: synthesis, characterization, and use as sacrificial templates for generating triangular nanorings of gold. Adv Mater 15(9): 695–699
21. Chen SH, Carroll DL (2002) Synthesis and characterization of truncated triangular silver nanoplates. Nano Lett 2(9):1003–1007
22. Averitt RD, Sarkar D, Halas NJ (1997) Plasmon resonance shifts of au-coated au_2s nanoshells: insight into multicomponent nanoparticle growth. Phys Rev Lett 78(22):4217–4220
23. Oldenburg SJ, Averitt RD, Westcott SL, Halas NJ (1998) Nanoengineering of optical resonances. Chem Phys Lett 288(2–4):243–247
24. Halas NJ (2005) Playing with plasmons. Tuning the optical resonant properties of metallic nanoshells. Mrs Bull 30(5):362–367
25. Hao E, Bailey RC, Schatz GC, Hupp JT et al (2004) Synthesis and optical properties of "branched" gold nanocrystals. Nano Lett 4(2):327–330
26. Nehl CL, Liao HW, Hafner JH (2006) Optical properties of star-shaped gold nanoparticles. Nano Lett 6(4):683–688
27. Chen JY, Wiley B, Li ZY, Campbell D et al (2005) Gold nanocages: engineering their structure for biomedical applications. Adv Mater 17(18):2255–2261
28. Chen JY, McLellan JM, Siekkinen A, Xiong YJ et al (2006) Facile synthesis of gold-silver nanocages with controllable pores on the surface. J Am Chem Soc 128(46):14776–14777

29. Kreibig U, Vollmer M (1995) Optical properties of metal clusters. Springer, Berlin
30. Bohren CF, Huffman DR (1998) Absorption and scattering of light by small particles. Wiley, New York
31. Mulvaney P (1996) Surface plasmon spectroscopy of nanosized metal particles. Langmuir 12(3):788–800
32. Raether H (1988) Surface plasmon on smooth and rough surfaces and on gratings. Springer, Berlin
33. Willets KA, Van Duyne RP (2007) Localized surface plasmon resonance spectroscopy and sensing. Annu Rev Phys Chem 58:267–297
34. Kuwata H, Tamaru H, Esumi K, Miyano K (2003) Resonant light scattering from metal nanoparticles: practical analysis beyond rayleigh approximation. Appl Phys Lett 83(22):4625–4627
35. Gan QQ, Song GF, Yang GH, Xu Y et al (2006) Near-field scanning optical microscopy with an active probe. Appl Phys Lett 88(12):121111
36. Mitsui T (2005) Development of a polarization-preserving optical-fiber probe for near-field scanning optical microscopy and the influences of bending and squeezing on the polarization properties. Rev Sci Instrum 76(4):043703
37. Betzig E, Chichester RJ (1993) Single molecules observed by near-field scanning optical microscopy. Science 262(5138):1422–1425
38. Betzig E, Trautman JK, Harris TD, Weiner JS et al (1991) Breaking the diffraction barrier–optical microscopy on a nanometric scale. Science 251(5000):1468–1470
39. Bethe HA (1944) Theory of diffraction by small holes. Phys Rev 66(7–8):163–182
40. de Abajo F (2002) Light transmission through a single cylindrical hole in a metallic film. Opt Express 10(25):1475–1484
41. Ozcan A, Cubukcu E, Bilenca A, Crozier KB et al (2006) Differential near-field scanning optical microscopy. Nano Lett 6(11):2609–2616
42. Egerton RF (1996) Electron energy-loss spectroscopy in the electron microscope second edition. Plenum, New York
43. Raether H (1980) Excitation of plasmons and interband transitions by electrons, vol 88. Springer, Berlin
44. Koh AL, Fernandez-Dominguez AI, McComb DW, Maier SA et al (2011) High-resolution mapping of electron-beam-excited plasmon modes in lithographically defined gold nanostructures. Nano Lett 11(3):1323–1330
45. Schaffer B, Grogger W, Kothleitner G, Hofer F (2010) Comparison of eftem and stem eels plasmon imaging of gold nanoparticles in a monochromated tem. Ultramicroscopy 110(8):1087–1093
46. Garcia de Abajo FJ (2010) Optical excitations in electron microscopy. Rev Mod Phys 82(1):209–275
47. Chu M-W, Myroshnychenko V, Chen CH, Deng J-P et al (2009) Probing bright and dark surface-plasmon modes in individual and coupled noble metal nanoparticles using an electron beam. Nano Lett 9(1):399–404
48. Nelayah J, Kociak M, Stephan O, Garcia de Abajo FJ et al (2007) Mapping surface plasmons on a single metallic nanoparticle. Nat Phys 3(5):348–353
49. N′Gom M, Li S, Schatz G, Erni R et al (2009) Electron-beam mapping of plasmon resonances in electromagnetically interacting gold nanorods. Phys Rev B 80(11):113411
50. Guiton BS, Iberi V, Li SZ, Leonard DN, Parish CM, Kotula PG, Varela M, Schatz GC, Pennycook SJ, Camden JP (2011) Correlated optical measurements and plasmon mapping of silver nanorods. Nano Lett 11(8):3482–3488
51. Campion A, Kambhampati P (1998) Surface-enhanced raman scattering. Chem Soc Rev 27(4):241–250
52. Kneipp K, Kneipp H, Itzkan I, Dasari RR et al (1999) Ultrasensitive chemical analysis by raman spectroscopy. Chem Rev 99(10):2957–2976

53. Schatz GC (1984) Theoretical-studies of surface enhanced raman-scattering. Acc Chem Res 17(10):370–376
54. Moskovits M (1985) Surface-enhanced spectroscopy. Rev Mod Phys 57(3):783–826
55. Lal S, Grady NK, Goodrich GP, Halas NJ (2006) Profiling the near field of a plasmonic nanoparticle with raman-based molecular rulers. Nano Lett 6(10):2338–2343
56. Kelly KL, Coronado E, Zhao LL, Schatz GC (2003) The optical properties of metal nanoparticles: the influence of size, shape, and dielectric environment. J Phys Chem B 107(3):668–677
57. Noguez C (2007) Surface plasmons on metal nanoparticles: the influence of shape and physical environment. J Phys Chem C 111(10):3806–3819
58. Riikonen S, Romero I, Garcia de Abajo FJ (2005) Plasmon tunability in metallodielectric metamaterials. Phys Rev B 71(23):235104
59. Gonzalez AL, Noguez C (2007) Influence of morphology on the optical properties of metal nanoparticles. J Comput Theoret Nanosci 4(2):231–238
60. Yee KS (1966) Numerical solution of initial boundary value problems involving maxwell's equations in isotropic media. IEEE Trans Antenn Propag AP14(3):302–307
61. Jensen LL, Jensen L (2009) Atomistic electrodynamics model for optical properties of silver nanoclusters. J Phys Chem C 113(34):15182–15190
62. Morton SM, Jensen L (2009) Understanding the molecule-surface chemical coupling in sers. J Am Chem Soc 131(11):4090–4098
63. Zangwill A, Soven P (1980) Density-functional approach to local-field effects in finite systems – photoabsorption in the rare-gases. Phys Rev A 21(5):1561–1572
64. Rodriguez-Fernandez J, Perez-Juste J, Garcia de Abajo FJ, Liz-Marzan LM (2006) Seeded growth of submicron au colloids with quadrupole plasmon resonance modes. Langmuir 22(16):7007–7010
65. Malynych S, Chumanov G (2007) Extinction spectra of quasi-spherical silver sub-micron particles. J Quan Spectros Radiat Trans 106(1–3):297–303
66. Luther JM, Jain PK, Ewers T, Alivisatos AP (2011) Localized surface plasmon resonances arising from free carriers in doped quantum dots. Nat Mater 10(5):361–366
67. Wang C, Yin H, Chan R, Peng S et al (2009) One-pot synthesis of oleylamine coated auag alloy nps and their catalysis for co oxidation. Chem Mater 21(3):433–435
68. Mulvaney P, Giersig M, Henglein A (1993) Electrochemistry of multilayer colloids - preparation and absorption-spectrum of gold-coated silver particles. J Phys Chem 97(27):7061–7064
69. Hostetler MJ, Zhong CJ, Yen BKH, Anderegg J et al (1998) Stable, monolayer-protected metal alloy clusters. J Am Chem Soc 120(36):9396–9397
70. Link S, Wang ZL, El-Sayed MA (1999) Alloy formation of gold-silver nanoparticles and the dependence of the plasmon absorption on their composition. J Phys Chem B 103(18):3529–3533
71. Mallin MP, Murphy CJ (2002) Solution-phase synthesis of sub-10 nm au-ag alloy nanoparticles. Nano Lett 2(11):1235–1237
72. Shibata T, Bunker BA, Zhang ZY, Meisel D et al (2002) Size-dependent spontaneous alloying of Au-Ag nanoparticles. J Am Chem Soc 124(40):11989–11996
73. Wilson OM, Scott RWJ, Garcia-Martinez JC, Crooks RM (2005) Synthesis, characterization, and structure-selective extraction of 1-3-nm diameter auag dendrimer-encapsulated bimetallic nanoparticles. J Am Chem Soc 127(3):1015–1024
74. Wilcoxon J (2009) Optical absorption properties of dispersed gold and silver alloy nanoparticles. J Phys Chem B 113(9):2647–2656
75. Hodak JH, Henglein A, Giersig M, Hartland GV (2000) Laser-induced inter-diffusion in auag core-shell nanoparticles. J Phys Chem B 104(49):11708–11718
76. Mallik K, Mandal M, Pradhan N, Pal T (2001) Seed mediated formation of bimetallic nanoparticles by uv irradiation: a photochemical approach for the preparation of "core-shell" type structures. Nano Lett 1(6):319–322

77. Wilcoxon JP, Provencio PP (2004) Heterogeneous growth of metal clusters from solutions of seed nanoparticles. J Am Chem Soc 126(20):6402–6408
78. Zhang J, Tang Y, Weng L, Ouyang M (2009) Versatile strategy for precisely tailored core@shell nanostructures with single shell layer accuracy: the case of metallic shell. Nano Lett 9(12):4061–4065
79. Wang C, Peng S, Chan R, Sun S (2009) Synthesis of auag alloy nanoparticles from core/shell-structured ag/au. Small 5(5):567–570
80. Liz-Marzan LM (2006) Tailoring surface plasmons through the morphology and assembly of metal nanoparticles. Langmuir 22(1):32–41
81. Rivas L, Sanchez-Cortes S, Garcia-Ramos JV, Morcillo G (2000) Mixed silver/gold colloids: a study of their formation, morphology, and surface-enhanced raman activity. Langmuir 16(25):9722–9728
82. Srnova-Sloufova I, Lednicky F, Gemperle A, Gemperlova J (2000) Core-shell (ag)au bimetallic nanoparticles: analysis of transmission electron microscopy images. Langmuir 16(25):9928–9935
83. Rodriguez-Gonzalez B, Burrows A, Watanabe M, Kiely CJ et al (2005) Multishell bimetallic auag nanoparticles: synthesis, structure and optical properties. J Mater Chem 15(17):1755–1759
84. Shore MS, Wang J, Johnston-Peck AC, Oldenburg AL et al (2011) Synthesis of au(core)/ag(shell) nanoparticles and their conversion to auag alloy nanoparticles. Small 7(2):230–234
85. Huang XH, Neretina S, El-Sayed MA (2009) Gold nanorods: from synthesis and properties to biological and biomedical applications. Adv Mater 21(48):4880–4910
86. Murphy CJ, San TK, Gole AM, Orendorff CJ et al (2005) Anisotropic metal nanoparticles: synthesis, assembly, and optical applications. J Phys Chem B 109(29):13857–13870
87. Perez-Juste J, Pastoriza-Santos I, Liz-Marzan LM, Mulvaney P (2005) Gold nanorods: synthesis, characterization and applications. Coord Chem Rev 249(17–18):1870–1901
88. Gans R (1912) The shape of ultra microscopic gold particles. Annalen Der Physik 37(5):881–900
89. Yu YY, Chang SS, Lee CL, Wang CRC (1997) Gold nanorods: electrochemical synthesis and optical properties. J Phys Chem B 101(34):6661–6664
90. Zuloaga J, Prodan E, Nordlander P (2010) Quantum plasmonics: optical properties and tunability of metallic nanorods. ACS Nano 4(9):5269–5276
91. Murphy CJ, Gole AM, Hunyadi SE, Orendorff CJ (2006) One-dimensional colloidal gold and silver nanostructures. Inorg Chem 45(19):7544–7554
92. Caswell KK, Bender CM, Murphy CJ (2003) Seedless, surfactantless wet chemical synthesis of silver nanowires. Nano Lett 3(5):667–669
93. Wiley BJ, Chen Y, McLellan JM, Xiong Y et al (2007) Synthesis and optical properties of silver nanobars and nanorice. Nano Lett 7(4):1032–1036
94. Martin CR (1996) Membrane-based synthesis of nanomaterials. Chem Mater 8(8):1739–1746
95. Mieszawska AJ, Jalilian R, Sumanasekera GU, Zamborini FP (2007) The synthesis and fabrication of one-dimensional nanoscale heterojunctions. Small 3(5):722–756
96. Chang SS, Shih CW, Chen CD, Lai WC et al (1999) The shape transition of gold nanorods. Langmuir 15(3):701–709
97. Murphy CJ, Thompson LB, Chernak DJ, Yang JA et al (2011) Gold nanorod crystal growth: from seed-mediated synthesis to nanoscale sculpting. Curr Opin Colloid Interf Sci 16(2):128–134
98. Wiesner J, Wokaun A (1989) Anisometric gold colloids - preparation, characterization, and optical-properties. Chem Phys Lett 157(6):569–575
99. Jana NR, Gearheart L, Murphy CJ (2001) Wet chemical synthesis of high aspect ratio cylindrical gold nanorods. J Phys Chem B 105(19):4065–4067
100. Jana NR, Gearheart L, Murphy CJ (2001) Seed-mediated growth approach for shape-controlled synthesis of spheroidal and rod-like gold nanoparticles using a surfactant template. Adv Mater 13(18):1389–1393

101. Grzelczak M, Perez-Juste J, Mulvaney P, Liz-Marzan LM (2008) Shape control in gold nanoparticle synthesis. Chem Soc Rev 37(9):1783–1791
102. Wu HY, Chu HC, Kuo TJ, Kuo CL et al (2005) Seed-mediated synthesis of high aspect ratio gold nanorods with nitric acid. Chem Mater 17(25):6447–6451
103. Chen HM, Peng HC, Liu RS, Asakura K et al (2005) Controlling the length and shape of gold nanorods. J Phys Chem B 109(42):19553–19555
104. Sau TK, Murphy CJ (2004) Room temperature, high-yield synthesis of multiple shapes of gold nanoparticles in aqueous solution. J Am Chem Soc 126(28):8648–8649
105. Smith DK, Korgel BA (2008) The importance of the ctab surfactant on the colloidal seed-mediated synthesis of gold nanorods. Langmuir 24(3):644–649
106. Smith DK, Miller NR, Korgel BA (2009) Iodide in ctab prevents gold nanorod formation. Langmuir 25(16):9518–9524
107. Kim F, Song JH, Yang PD (2002) Photochemical synthesis of gold nanorods. J Am Chem Soc 124(48):14316–14317
108. Giannici F, Placido T, Curri ML, Striccoli M et al (2009) The fate of silver ions in the photochemical synthesis of gold nanorods: an extended x-ray absorption fine structure analysis. Dalton Trans 46:10367–10374
109. Placido T, Comparelli R, Giannici F, Cozzoli PD et al (2009) Photochemical synthesis of water-soluble gold nanorods: the role of silver in assisting anisotropic growth. Chem Mater 21(18):4192–4202
110. Niidome Y, Nishioka K, Kawasaki H, Yamada S (2003) Rapid synthesis of gold nanorods by the combination of chemical reduction and photoirradiation processes; morphological changes depending on the growing processes. Chem Commun 18:2376–2377
111. Miranda OR, Ahmadi TS (2005) Effects of intensity and energy of cw uv light on the growth of gold nanorods. J Phys Chem B 109(33):15724–15734
112. Ahmed M, Narain R (2010) Rapid synthesis of gold nanorods using a one-step photochemical strategy. Langmuir 26(23):18392–18399
113. Nishioka K, Niidome Y, Yamada S (2007) Photochemical reactions of ketones to synthesize gold nanorods. Langmuir 23(20):10353–10356
114. Billot L, de la Chapelle ML, Grimault AS, Vial A et al (2006) Surface enhanced raman scattering on gold nanowire arrays: evidence of strong multipolar surface plasmon resonance enhancement. Chem Phys Lett 422(4–6):303–307
115. Dayal PB, Koyama F (2007) Polarization control of 0.85 mu m vertical-cavity surface-emitting lasers integrated with gold nanorod arrays. Appl Phys Lett 91(11):111–107
116. Hu M, Novo C, Funston A, Wang H et al (2008) Dark-field microscopy studies of single metal nanoparticles: understanding the factors that influence the linewidth of the localized surface plasmon resonance. J Mater Chem 18(17):1949–1960
117. Sonnichsen C, Franzl T, Wilk T, von Plessen G et al (2002) Drastic reduction of plasmon damping in gold nanorods. Phys Rev Lett 88(7):077402
118. Novo C, Gomez D, Perez-Juste J, Zhang Z et al (2006) Contributions from radiation damping and surface scattering to the linewidth of the longitudinal plasmon band of gold nanorods: a single particle study. Phys Chem Chem Phys 8(30):3540–3546
119. Mooradia A (1969) Photoluminescence of metals. Phys Rev Lett 22(5):185–187
120. Boyd GT, Yu ZH, Shen YR (1986) Photoinduced luminescence from the noble-metals and its enhancement on roughened surfaces. Phys Rev B 33(12):7923–7936
121. Mohamed MB, Volkov V, Link S, El-Sayed MA (2000) The 'lightning' gold nanorods: fluorescence enhancement of over a million compared to the gold metal. Chem Phys Lett 317(6):517–523
122. Eustis S, El-Sayed M (2005) Aspect ratio dependence of the enhanced fluorescence intensity of gold nanorods: experimental and simulation study. J Phys Chem B 109(34):16350–16356
123. Bouhelier A, Bachelot R, Lerondel G, Kostcheev S et al (2005) Surface plasmon characteristics of tunable photoluminescence in single gold nanorods. Phys Rev Lett 95(26):267405

124. Imura K, Nagahara T, Okamoto H (2004) Plasmon mode imaging of single gold nanorods. J Am Chem Soc 126(40):12730–12731
125. Imura K, Nagahara T, Okamoto H (2005) Near-field two-photon-induced photoluminescence from single gold nanorods and imaging of plasmon modes. J Phys Chem B 109(27):13214–13220
126. Imura K, Nagahara T, Okamoto H (2005) Near-field optical imaging of plasmon modes in gold nanorods. J Chem Phys 122(15):154701
127. Wang HF, Huff TB, Zweifel DA, He W et al (2005) In vitro and in vivo two-photon luminescence imaging of single gold nanorods. Proc Natl Acad Sci USA 102(44):15752–15756
128. Durr NJ, Larson T, Smith DK, Korgel BA et al (2007) Two-photon luminescence imaging of cancer cells using molecularly targeted gold nanorods. Nano Lett 7(4):941–945
129. Sershen SR, Westcott SL, Halas NJ, West JL (2000) Temperature-sensitive polymer-nanoshell composites for photothermally modulated drug delivery. J Biomed Mater Res 51(3):293–298
130. Hirsch LR, Jackson JB, Lee A, Halas NJ et al (2003) A whole blood immunoassay using gold nanoshells. Anal Chem 75(10):2377–2381
131. Jackson JB, Westcott SL, Hirsch LR, West JL et al (2003) Controlling the surface enhanced raman effect via the nanoshell geometry. Appl Phys Lett 82(2):257–259
132. Jackson JB, Halas NJ (2004) Surface-enhanced raman scattering on tunable plasmonic nanoparticle substrates. Proc Natl Acad Sci USA 101(52):17930–17935
133. Tam F, Goodrich GP, Johnson BR, Halas NJ (2007) Plasmonic enhancement of molecular fluorescence. Nano Lett 7(2):496–501
134. Kundu J, Le F, Nordlander P, Halas NJ (2008) Surface enhanced infrared absorption (seira) spectroscopy on nanoshell aggregate substrates. Chem Phys Lett 452(1–3):115–119
135. Hirsch LR, Stafford RJ, Bankson JA, Sershen SR et al (2003) Nanoshell-mediated near-infrared thermal therapy of tumors under magnetic resonance guidance. Proc Natl Acad Sci USA 100(23):13549–13554
136. Loo C, Lin A, Hirsch L, Lee MH et al (2004) Nanoshell-enabled photonics-based imaging and therapy of cancer. Technol Cancer Res Treat 3(1):33–40
137. Aden AL, Kerker M (1951) Scattering of electromagnetic waves from 2 concentric spheres. J Appl Phys 22(10):1242–1246
138. Neeves AE, Birnboim MH (1989) Composite structures for the enhancement of nonlinear-optical susceptibility. J Opt Soc Am B Opt Phys 6(4):787–796
139. Zhou HS, Honma I, Komiyama H, Haus JW (1994) Controlled synthesis and quantum-size effect in gold-coated nanoparticles. Phys Rev B 50(16):12052–12056
140. Stober W, Fink A, Bohn E (1968) Controlled growth of monodisperse silica spheres in micron size range. J Colloid Interf Sci 26(1):62–69
141. Shi WL, Sahoo Y, Swihart MT, Prasad PN (2005) Gold nanoshells on polystyrene cores for control of surface plasmon resonance. Langmuir 21(4):1610–1617
142. Bardhan R, Grady NK, Ali T, Halas NJ (2010) Metallic nanoshells with semiconductor cores: optical characteristics modified by core medium properties. ACS Nano 4(10):6169–6179
143. Brinson BE, Lassiter JB, Levin CS, Bardhan R et al (2008) Nanoshells made easy: improving au layer growth on nanoparticle surfaces. Langmuir 24(24):14166–14171
144. Jackson JB, Halas NJ (2001) Silver nanoshells: variations in morphologies and optical properties. J Phys Chem B 105(14):2743–2746
145. Jiang ZJ, Liu CY (2003) Seed-mediated growth technique for the preparation of a silver nanoshell on a silica sphere. J Phys Chem B 107(45):12411–12415
146. Wang H, Tam F, Grady NK, Halas NJ (2005) Cu nanoshells: effects of interband transitions on the nanoparticle plasmon resonance. J Phys Chem B 109(39):18218–18222
147. Liu JB, Dong W, Zhan P, Wang SZ et al (2005) Synthesis of bimetallic nanoshells by an improved electroless plating method. Langmuir 21(5):1683–1686

148. Oldenburg SJ, Jackson JB, Westcott SL, Halas NJ (1999) Infrared extinction properties of gold nanoshells. Appl Phys Lett 75(19):2897–2899
149. Tam F, Moran C, Halas NJ (2004) Geometrical parameters controlling sensitivity of nanoshell plasmon resonances to changes in dielectric environment. J Phys Chem B 108(45):17290–17294
150. Nehl CL, Grady NK, Goodrich GP, Tam F et al (2004) Scattering spectra of single gold nanoshells. Nano Lett 4(12):2355–2359
151. Tam F, Chen AL, Kundu J, Wang H et al (2007) Mesoscopic nanoshells: geometry-dependent plasmon resonances beyond the quasistatic limit. J Chem Phys 127(20):204703
152. Brandl DW, Nordlander P (2007) Plasmon modes of curvilinear metallic core/shell particles. J Chem Phys 126(14):144708
153. Wang H, Fu K, Drezek RA, Halas NJ (2006) Light scattering from spherical plasmonic nanoantennas: effects of nanoscale roughness. Appl Phys B Lasers Optics 84(1–2):191–195
154. Wang H, Goodrich GP, Tam F, Oubre C et al (2005) Controlled texturing modifies the surface topography and plasmonic properties of au nanoshells. J Phys Chem B 109(22):11083–11087
155. Oubre C, Nordlander P (2004) Optical properties of metallodielectric nanostructures calculated using the finite difference time domain method. J Phys Chem B 108(46):17740–17747
156. Prodan E, Radloff C, Halas NJ, Nordlander P (2003) A hybridization model for the plasmon response of complex nanostructures. Science 302(5644):419–422
157. Prodan E, Nordlander P (2004) Plasmon hybridization in spherical nanoparticles. J Chem Phys 120(11):5444–5454
158. Nordlander P, Oubre C, Prodan E, Li K et al (2004) Plasmon hybridization in nanoparticle dimers. Nano Lett 4(5):899–903
159. Wang H, Brandl DW, Nordlander P, Halas NJ (2007) Plasmonic nanostructures: artificial molecules. Acc Chem Res 40(1):53–62
160. Prodan E, Nordlander P (2003) Structural tunability of the plasmon resonances in metallic nanoshells. Nano Lett 3(4):543–547
161. Radloff C, Halas NJ (2004) Plasmonic properties of concentric nanoshells. Nano Lett 4(7):1323–1327
162. Bardhan R, Mukherjee S, Mirin NA, Levit SD et al (2010) Nanosphere-in-a-nanoshell: a simple nanomatryushka. J Phys Chem C 114(16):7378–7383
163. Wang H, Wu YP, Lassiter B, Nehl CL et al (2006) Symmetry breaking in individual plasmonic nanoparticles. Proc Natl Acad Sci USA 103(29):10856–10860
164. Wu Y, Nordlander P (2006) Plasmon hybridization in nanoshells with a nonconcentric core. J Chem Phys 125(12):124708
165. Shvets G, Urzhumov YA (2004) Engineering the electromagnetic properties of periodic nanostructures using electrostatic resonances. Phys Rev Lett 93(24):243902
166. Brandl DW, Oubre C, Nordlander P (2005) Plasmon hybridization in nanoshell dimers. J Chem Phys 123(2):024701
167. Love JC, Gates BD, Wolfe DB, Paul KE et al (2002) Fabrication and wetting properties of metallic half-shells with submicron diameters. Nano Lett 2(8):891–894
168. Liu J, McBean KE, Harris N, Cortie MB (2007) Optical properties of suspensions of gold half-shells. Mater Sci Engin B-Solid State Mater Advan Technol 140(3):195–198
169. Charnay C, Lee A, Man SQ, Moran CE et al (2003) Reduced symmetry metallodielectric nanoparticles: chemical synthesis and plasmonic properties. J Phys Chem B 107(30):7327–7333
170. Lu Y, Liu GL, Kim J, Mejia YX et al (2005) Nanophotonic crescent moon structures with sharp edge for ultrasensitive biomolecular detection by local electromagnetic field enhancement effect. Nano Lett 5(1):119–124
171. Liu GL, Lu Y, Kim J, Doll JC et al (2005) Magnetic nanocrescents as controllable surface-enhanced raman scattering nanoprobes for biomolecular imaging. Adv Mater 17(22):2683–2688

172. Lassiter JB, Knight MW, Mirin NA, Halas NJ (2009) Reshaping the plasmonic properties of an individual nanoparticle. Nano Lett 9(12):4326–4332
173. Mirin NA, Halas NJ (2009) Light-bending nanoparticles. Nano Lett 9(3):1255–1259
174. Cortie M, Ford M (2007) A plasmon-induced current loop in gold semi-shells. Nanotechnology 18(23):235704
175. Knight MW, Halas NJ (2008) Nanoshells to nanoeggs to nanocups: optical properties of reduced symmetry core-shell nanoparticles beyond the quasistatic limit. New J Phys 10:105006
176. Mirin NA, Ali TA, Nordlander P, Halas NJ (2010) Perforated semishells: far-field directional control and optical frequency magnetic response. ACS Nano 4(5):2701–2712
177. Wang H, Brandl DW, Le F, Nordlander P et al (2006) Nanorice: a hybrid plasmonic nanostructure. Nano Lett 6(4):827–832
178. Schuck PJ, Fromm DP, Sundaramurthy A, Kino GS et al (2005) Improving the mismatch between light and nanoscale objects with gold bowtie nanoantennas. Phys Rev Lett 94:017402
179. Sanchez EJ, Novotny L, Xie XS (1999) Near-field fluorescence microscopy based on two-photon excitation with metal tips. Phys Rev Lett 82(20):4014–4017
180. Millstone JE, Hurst SJ, Metraux GS, Cutler JI et al (2009) Colloidal gold and silver triangular nanoprisms. Small 5(6):646–664
181. Shuford KL, Ratner MA, Schatz GC (2005) Multipolar excitation in triangular nanoprisms. J Chem Phys 123(11):114713
182. Jin RC, Cao YC, Hao EC, Metraux GS et al (2003) Controlling anisotropic nanoparticle growth through plasmon excitation. Nature 425(6957):487–490
183. Callegari A, Tonti D, Chergui M (2003) Photochemically grown silver nanoparticles with wavelength-controlled size and shape. Nano Lett 3(11):1565–1568
184. Xue C, Mirkin CA (2007) pH-switchable silver nanoprism growth pathways. Angew Chem Int Ed 46(12):2036–2038
185. Xue C, Metraux GS, Millstone JE, Mirkin CA (2008) Mechanistic study of photomediated triangular silver nanoprism growth. J Am Chem Soc 130(26):8337–8344
186. Pastoriza-Santos I, Liz-Marzan LM (2002) Formation of pvp-protected metal nanoparticles in dmf. Langmuir 18(7):2888–2894
187. Malikova N, Pastoriza-Santos I, Schierhorn M, Kotov NA et al (2002) Layer-by-layer assembled mixed spherical and planar gold nanoparticles: control of interparticle interactions. Langmuir 18(9):3694–3697
188. Kim F, Connor S, Song H, Kuykendall T et al (2004) Platonic gold nanocrystals. Angew Chem Int Ed 43(28):3673–3677
189. Shankar SS, Rai A, Ankamwar B, Singh A et al (2004) Biological synthesis of triangular gold nanoprisms. Nat Mater 3(7):482–488
190. Millstone JE, Metraux GS, Mirkin CA (2006) Controlling the edge length of gold nanoprisms via a seed-mediated approach. Adv Funct Mater 16(9):1209–1214
191. Zhang Q, Ge JP, Pham T, Goebl J et al (2009) Reconstruction of silver nanoplates by uv irradiation: tailored optical properties and enhanced stability. Angew Chem Int Ed 48(19):3516–3519
192. Lee BH, Hsu MS, Hsu YC, Lo CW et al (2010) A facile method to obtain highly stable silver nanoplate colloids with desired surface plasmon resonance wavelengths. J Phys Chem C 114(14):6222–6227
193. An J, Tang B, Zheng XL, Zhou J et al (2008) Sculpturing effect of chloride ions in shape transformation from triangular to discal silver nanoplates. J Phys Chem C 112(39):15176–15182
194. Ciou SH, Cao YW, Huang HC, Su DY et al (2009) Sers enhancement factors studies of silver nanoprism and spherical nanoparticle colloids in the presence of bromide ions. J Phys Chem C 113(22):9520–9525

195. Tang B, An J, Zheng XL, Xu SP et al (2008) Silver nanodisks with tunable size by heat aging. J Phys Chem C 112(47):18361–18367
196. Tao A, Sinsermsuksakul P, Yang P (2006) Polyhedral silver nanocrystals with distinct scattering signatures. Angew Chem Int Ed 45(28):4597–4601
197. Khoury CG, Vo-Dinh T (2008) Gold nanostars for surface-enhanced raman scattering: synthesis, characterization and optimization. J Phys Chem C 112(48):18849–18859
198. Nehl CL, Hafner JH (2008) Shape-dependent plasmon resonances of gold nanoparticles. J Mater Chem 18(21):2415–2419
199. Xie JP, Lee JY, Wang DIC (2007) Seedless, surfactantless, high-yield synthesis of branched gold nanocrystals in hepes buffer solution. Chem Mater 19(11):2823–2830
200. Chen SH, Wang ZL, Ballato J, Foulger SH et al (2003) Monopod, bipod, tripod, and tetrapod gold nanocrystals. J Am Chem Soc 125(52):16186–16187
201. Bakr OM, Wunsch BH, Stellacci F (2006) High-yield synthesis of multi-branched urchin-like gold nanoparticles. Chem Mater 18(14):3297–3301
202. Kim DY, Yu T, Cho EC, Ma Y et al (2011) Synthesis of gold nano-hexapods with controllable arm lengths and their tunable optical properties. Angew Chem Int Ed 50(28):6328–6331
203. Wu HL, Chen CH, Huang MH (2009) Seed-mediated synthesis of branched gold nanocrystals derived from the side growth of pentagonal bipyramids and the formation of gold nanostars. Chem Mater 21(1):110–114
204. Liao HG, Jiang YX, Zhou ZY, Chen SP et al (2008) Shape-controlled synthesis of gold nanoparticles in deep eutectic solvents for studies of structure-functionality relationships in electrocatalysis. Angew Chem Int Ed 47(47):9100–9103
205. Burt JL, Elechiguerra JL, Reyes-Gasga J, Montejano-Carrizales JM et al (2005) Beyond archimedean solids: star polyhedral gold nanocrystals. J Cryst Growth 285(4):681–691
206. Yamamoto M, Kashiwagi Y, Sakata T, Mori H et al (2005) Synthesis and morphology of star-shaped gold nanoplates protected by poly(n-vinyl-2-pyrrolidone). Chem Mater 17(22):5391–5393
207. Hao F, Nehl CL, Hafner JH, Nordlander P (2007) Plasmon resonances of a gold nanostar. Nano Lett 7(3):729–732
208. Skrabalak SE, Chen J, Sun Y, Lu X et al (2008) Gold nanocages: synthesis, properties, and applications. Acc Chem Res 41(12):1587–1595
209. Sun YG, Xia YN (2002) Shape-controlled synthesis of gold and silver nanoparticles. Science 298(5601):2176–2179
210. Skrabalak SE, Au L, Li X, Xia Y (2007) Facile synthesis of ag nanocubes and au nanocages. Nat Protoc 2(9):2182–2190
211. Sun YG, Xia YN (2004) Mechanistic study on the replacement reaction between silver nanostructures and chloroauric acid in aqueous medium. J Am Chem Soc 126(12):3892–3901
212. Chen JY, Wiley B, McLellan J, Xiong YJ et al (2005) Optical properties of pd-ag and pt-ag nanoboxes synthesized via galvanic replacement reactions. Nano Lett 5(10):2058–2062
213. Cobley CM, Campbell DJ, Xia Y (2008) Tailoring the optical and catalytic properties of gold-silver nanoboxes and nanocages by introducing palladium. Adv Mater 20(4):748–752
214. Skrabalak SE, Chen J, Au L, Lu X et al (2007) Gold nanocages for biomedical applications. Adv Mater 19(20):3177–3184
215. Yang X, Skrabalak SE, Li Z-Y, Xia Y et al (2007) Photoacoustic tomography of a rat cerebral cortex in vivo with au nanocages as an optical contrast agent. Nano Lett 7(12):3798–3802
216. Chen J, Saeki F, Wiley BJ, Cang H et al (2005) Gold nanocages: bioconjugation and their potential use as optical imaging contrast agents. Nano Lett 5(3):473–477
217. Cang H, Sun T, Li ZY, Chen JY et al (2005) Gold nanocages as contrast agents for spectroscopic optical coherence tomography. Opt Lett 30(22):3048–3050

218. Halas NJ, Lal S, Chang W-S, Link S et al (2011) Plasmons in strongly coupled metallic nanostructures. Chem Rev 111(6):3913–3961
219. Jin RC, Wu GS, Li Z, Mirkin CA et al (2003) What controls the melting properties of DNA-linked gold nanoparticle assemblies? J Am Chem Soc 125(6):1643–1654
220. Storhoff JJ, Elghanian R, Mucic RC, Mirkin CA et al (1998) One-pot colorimetric differentiation of polynucleotides with single base imperfections using gold nanoparticle probes. J Am Chem Soc 120(9):1959–1964
221. Storhoff JJ, Lazarides AA, Mucic RC, Mirkin CA et al (2000) What controls the optical properties of DNA-linked gold nanoparticle assemblies? J Am Chem Soc 122(19):4640–4650
222. Tan SJ, Campolongo MJ, Luo D, Cheng WL (2011) Building plasmonic nanostructures with DNA. Nat Nanotechnol 6(5):268–276
223. Camden JP, Dieringer JA, Wang Y, Masiello DJ et al (2008) Probing the structure of single-molecule surface-enhanced raman scattering hot spots. J Am Chem Soc 130(38):12616–12617
224. Dieringer JA, Lettan RB II, Scheidt KA, Van Duyne RP (2007) A frequency domain existence proof of single-molecule surface-enhanced raman spectroscopy. J Am Chem Soc 129(51):16249–16256
225. Kneipp K, Kneipp H, Kneipp J (2006) Surface-enhanced raman scattering in local optical fields of silver and gold nanoaggregatess - from single-molecule raman spectroscopy to ultrasensitive probing in live cells. Acc Chem Res 39(7):443–450
226. Kneipp K, Wang Y, Kneipp H, Perelman LT et al (1997) Single molecule detection using surface-enhanced raman scattering (sers). Phys Rev Lett 78(9):1667–1670
227. Michaels AM, Nirmal M, Brus LE (1999) Surface enhanced raman spectroscopy of individual rhodamine 6g molecules on large ag nanocrystals. J Am Chem Soc 121(43):9932–9939
228. Nie SM, Emery SR (1997) Probing single molecules and single nanoparticles by surface-enhanced raman scattering. Science 275(5303):1102–1106
229. Aravind PK, Nitzan A, Metiu H (1981) The interaction between electromagnetic resonances and its role in spectroscopic studies of molecules adsorbed on colloidal particles or metal spheres. Surf Sci 110(1):189–204
230. Oubre C, Nordlander P (2005) Finite-difference time-domain studies of the optical properties of nanoshell dimers. J Phys Chem B 109(20):10042–10051
231. Su KH, Wei QH, Zhang X, Mock JJ et al (2003) Interparticle coupling effects on plasmon resonances of nanogold particles. Nano Lett 3(8):1087–1090
232. Hao E, Schatz GC (2004) Electromagnetic fields around silver nanoparticles and dimers. J Chem Phys 120(1):357–366
233. Brown LV, Sobhani H, Lassiter JB, Nordlander P et al (2010) Heterodimers: plasmonic properties of mismatched nanoparticle pairs. ACS Nano 4(2):819–832
234. Lassiter JB, Aizpurua J, Hernandez LI, Brandl DW et al (2008) Close encounters between two nanoshells. Nano Lett 8(4):1212–1218
235. Talley CE, Jackson JB, Oubre C, Grady NK et al (2005) Surface-enhanced raman scattering from individual au nanoparticles and nanoparticle dimer substrates. Nano Lett 5(8):1569–1574
236. Li W, Camargo PHC, Lu X, Xia Y (2009) Dimers of silver nanospheres: facile synthesis and their use as hot spots for surface-enhanced raman scattering. Nano Lett 9(1):485–490
237. Camargo PHC, Au L, Rycenga M, Li W et al (2010) Measuring the sers enhancement factors of dimers with different structures constructed from silver nanocubes. Chem Phys Lett 484(4–6):304–308
238. Camargo PHC, Rycenga M, Au L, Xia Y (2009) Isolating and probing the hot spot formed between two silver nanocubes. Angew Chem Int Ed 48(12):2180–2184
239. Fromm DP, Sundaramurthy A, Kinkhabwala A, Schuck PJ et al (2006) Exploring the chemical enhancement for surface-enhanced raman scattering with au bowtie nanoantennas. J Chem Phys 124(6):061101

240. Jackel F, Kinkhabwala AA, Moerner WE (2007) Gold bowtie nanoantennas for surface-enhanced raman scattering under controlled electrochemical potential. Chem Phys Lett 446(4–6):339–343
241. Schuck PJ, Fromm DP, Sundaramurthy A, Kino GS et al (2005) Improving the mismatch between light and nanoscale objects with gold bowtie nanoantennas. Phys Rev Lett 94(1):017402
242. Gunnarsson L, Rindzevicius T, Prikulis J, Kasemo B et al (2005) Confined plasmons in nanofabricated single silver particle pairs: experimental observations of strong interparticle interactions. J Phys Chem B 109(3):1079–1087
243. Pena-Rodriguez O, Pal U, Campoy-Quiles M, Rodriguez-Fernandez L et al (2011) Enhanced fano resonance in asymmetrical au:Ag heterodimers. J Phys Chem C 115(14):6410–6414
244. Shao L, Woo KC, Chen H, Jin Z et al (2010) Angle- and energy-resolved plasmon coupling in gold nanorod dimers. ACS Nano 4(6):3053–3062
245. Slaughter LS, Wu Y, Willingham BA, Nordlander P et al (2010) Effects of symmetry breaking and conductive contact on the plasmon coupling in gold nanorod dimers. ACS Nano 4(8):4657–4666
246. Yang Z-J, Zhang Z-S, Zhang W, Hao Z-H et al (2010) Twinned fano interferences induced by hybridized plasmons in au-ag nanorod heterodimers. Appl Phys Lett 96(13):131113
247. Funston AM, Novo C, Davis TJ, Mulvaney P (2009) Plasmon coupling of gold nanorods at short distances and in different geometries. Nano Lett 9(4):1651–1658
248. Jain PK, Eustis S, El-Sayed MA (2006) Plasmon coupling in nanorod assemblies: optical absorption, discrete dipole approximation simulation, and exciton-coupling model. J Phys Chem B 110(37):18243–18253
249. Sonnichsen C, Reinhard BM, Liphardt J, Alivisatos AP (2005) A molecular ruler based on plasmon coupling of single gold and silver nanoparticles. Nat Biotechnol 23(6):741–745
250. Jain PK, Huang W, El-Sayed MA (2007) On the universal scaling behavior of the distance decay of plasmon coupling in metal nanoparticle pairs: a plasmon ruler equation. Nano Lett 7(7):2080–2088
251. Liu GL, Yin Y, Kunchakarra S, Mukherjee B et al (2006) A nanoplasmonic molecular ruler for measuring nuclease activity and DNA footprinting. Nat Nanotechnol 1(1):47–52
252. Reinhard BM, Sheikholeslami S, Mastroianni A, Alivisatos AP et al (2007) Use of plasmon coupling to reveal the dynamics of DNA bending and cleavage by single ecorv restriction enzymes. Proc Natl Acad Sci USA 104(8):2667–2672
253. Reinhard BM, Siu M, Agarwal H, Alivisatos AP et al (2005) Calibration of dynamic molecular rule based on plasmon coupling between gold nanoparticles. Nano Lett 5(11):2246–2252
254. Roy R, Hohng S, Ha T (2008) A practical guide to single-molecule fret. Nat Methods 5(6):507–516
255. Brandl DW, Mirin NA, Nordlander P (2006) Plasmon modes of nanosphere trimers and quadrumers. J Phys Chem B 110(25):12302–12310
256. Chuntonov L, Haran G (2011) Trimeric plasmonic molecules: the role of symmetry. Nano Lett 11(6):2440–2445
257. Fan JA, Bao K, Wu C, Bao J et al (2010) Fano-like interference in self-assembled plasmonic quadrumer clusters. Nano Lett 10(11):4680–4685
258. Rahmani M, Lukiyanchuk B, Ng B, Liew A, Tavakkoli KG et al (2011) Generation of pronounced fano resonances and tuning of subwavelength spatial light distribution in plasmonic pentamers. Opt Expr 19(6):4949–4956
259. Fan JA, Wu C, Bao K, Bao J et al (2010) Self-assembled plasmonic nanoparticle clusters. Science 328(5982):1135–1138
260. Lassiter JB, Sobhani H, Fan JA, Kundu J et al (2010) Fano resonances in plasmonic nanoclusters: geometrical and chemical tunability. Nano Lett 10(8):3184–3189
261. Hentschel M, Dregely D, Vogelgesang R, Giessen H et al (2011) Plasmonic oligomers: the role of individual particles in collective behavior. ACS Nano 5(3):2042–2050

262. Hentschel M, Saliba M, Vogelgesang R, Giessen H et al (2010) Transition from isolated to collective modes in plasmonic oligomers. Nano Lett 10(7):2721–2726
263. de Waele R, Koenderink AF, Polman A (2007) Tunable nanoscale localization of energy on plasmon particle arrays. Nano Lett 7(7):2004–2008
264. Maier SA, Kik PG, Atwater HA (2003) Optical pulse propagation in metal nanoparticle chain waveguides. Phys Rev B 67(20):205402
265. Auguie B, Barnes WL (2008) Collective resonances in gold nanoparticle arrays. Phys Rev Lett 101(14):143902
266. Giannini V, Vecchi G, Rivas JG (2010) Lighting up multipolar surface plasmon polaritons by collective resonances in arrays of nanoantennas. Phys Rev Lett 105(26):266801
267. Vecchi G, Giannini V, Rivas JG (2009) Shaping the fluorescent emission by lattice resonances in plasmonic crystals of nanoantennas. Phys Rev Lett 102(14):146807
268. Chu YZ, Schonbrun E, Yang T, Crozier KB (2008) Experimental observation of narrow surface plasmon resonances in gold nanoparticle arrays. Appl Phys Lett 93(18):181108
269. Lamprecht B, Schider G, Lechner RT, Ditlbacher H et al (2000) Metal nanoparticle gratings: influence of dipolar particle interaction on the plasmon resonance. Phys Rev Lett 84(20):4721–4724
270. Hicks EM, Zou SL, Schatz GC, Spears KG et al (2005) Controlling plasmon line shapes through diffractive coupling in linear arrays of cylindrical nanoparticles fabricated by electron beam lithography. Nano Lett 5(6):1065–1070
271. Evanoff DD, Chumanov G (2005) Synthesis and optical properties of silver nanoparticles and arrays. Chemphyschem 6(7):1221–1231
272. Malynych S, Chumanov G (2003) Light-induced coherent interactions between silver nanoparticles in two-dimensional arrays. J Am Chem Soc 125(10):2896–2898
273. Zou SL, Schatz GC (2004) Narrow plasmonic/photonic extinction and scattering line shapes for one and two dimensional silver nanoparticle arrays. J Chem Phys 121(24):12606–12612
274. Mayshev AV, Malyshev VA, Knoester J (2008) Frequency-controlled localization of optical signals in graded plasmonic chains. Nano Lett 8(8):2369–2372
275. Sukharev M, Seideman T (2006) Phase and polarization control as a route to plasmonic nanodevices. Nano Lett 6(4):715–719
276. Nordlander P (2008) Plasmonics – subwavelength imaging in colour. Nat Photon 2(7):387–388
277. Kawata S, Ono A, Verma P (2008) Subwavelength colour imaging with a metallic nanolens. Nat Photon 2(7):438–442
278. Brongersma ML, Hartman JW, Atwater HA (2000) Electromagnetic energy transfer and switching in nanoparticle chain arrays below the diffraction limit. Phys Rev B 62(24):16356–16359
279. Zou SL, Schatz GC (2006) Metal nanoparticle array waveguides: proposed structures for subwavelength devices. Phys Rev B 74(12):125111
280. Nomura W, Ohtsu M, Yatsui T (2005) Nanodot coupler with a surface plasmon polariton condenser for optical far/near-field conversion. Appl Phys Lett 86(18):181108
281. Maier SA, Brongersma ML, Kik PG, Atwater HA (2002) Observation of near-field coupling in metal nanoparticle chains using far-field polarization spectroscopy. Phys Re B 65(19):193408
282. Maier SA, Brongersma ML, Kik PG, Meltzer S et al (2001) Plasmonics – a route to nanoscale optical devices. Adv Mater 13(19):1501–1505
283. Salerno M, Krenn JR, Hohenau A, Ditlbacher H et al (2005) The optical near-field of gold nanoparticle chains. Opt Commun 248(4–6):543–549
284. Bouhelier A, Bachelot R, Im JS, Wiederrecht GP et al (2005) Electromagnetic interactions in plasmonic nanoparticle arrays. J Phys Chem B 109(8):3195–3198
285. Maier SA, Kik PG, Atwater HA, Meltzer S et al (2003) Local detection of electromagnetic energy transport below the diffraction limit in metal nanoparticle plasmon waveguides. Nat Mater 2(4):229–232

286. Tao A, Sinsermsuksakul P, Yang P (2007) Tunable plasmonic lattices of silver nanocrystals. Nat Nanotechnol 2(7):435–440
287. Tao AR, Ceperley DP, Sinsermsuksakul P, Neureuther AR et al (2008) Self-organized silver nanoparticles for three-dimensional plasmonic crystals. Nano Lett 8(11):4033–4038
288. Tao AR, Huang J, Yang P (2008) Langmuir-blodgettry of nanocrystals and nanowires. Acc Chem Res 41(12):1662–1673
289. Wang HH, Liu CY, Wu SB, Liu NW et al (2006) Highly raman-enhancing substrates based on silver nanoparticle arrays with tunable sub-10 nm gaps. Adv Mater 18(4):491–495
290. Genov DA, Sarychev AK, Shalaev VM, Wei A (2004) Resonant field enhancements from metal nanoparticle arrays. Nano Lett 4(1):153–158
291. Wang H, Levin CS, Halas NJ (2005) Nanosphere arrays with controlled sub-10-nm gaps as surface-enhanced raman spectroscopy substrates. J Am Chem Soc 127(43):14992–14993
292. Wei A, Kim B, Sadtler B, Tripp SL (2001) Tunable surface-enhanced raman scattering from large gold nanoparticle arrays. Chemphyschem 2(12):743–745
293. Lee SJ, Morrill AR, Moskovits M (2006) Hot spots in silver nanowire bundles for surface-enhanced raman spectroscopy. J Am Chem Soc 128(7):2200–2201
294. Wang H, Kundu J, Halas NJ (2007) Plasmonic nanoshell arrays combine surface-enhanced vibrational spectroscopies on a single substrate. Angew Chem Int Ed 46(47):9040–9044
295. Le F, Brandl DW, Urzhumov YA, Wang H et al (2008) Metallic nanoparticle arrays: a common substrate for both surface-enhanced raman scattering and surface-enhanced infrared absorption. ACS Nano 2(4):707–718
296. Pillai S, Green MA (2010) Plasmonics for photovoltaic applications. Solar Energy Mater Solar Cells 94(9):1481–1486
297. Ferry VE, Sweatlock LA, Pacifici D, Atwater HA (2008) Plasmonic nanostructure design for efficient light coupling into solar cells. Nano Lett 8(12):4391–4397
298. Saeta PN, Ferry VE, Pacifici D, Munday JN et al (2009) How much can guided modes enhance absorption in thin solar cells? Opt Express 17(23):20975–20990
299. Pala RA, White J, Barnard E, Liu J et al (2009) Design of plasmonic thin-film solar cells with broadband absorption enhancements. Adv Mater 21(34):3504–3509
300. Ferry VE, Munday JN, Atwater HA (2010) Design considerations for plasmonic photovoltaics. Adv Mater 22(43):4794–4808
301. Yablonovitch E, Cody GD (1982) Intensity enhancement in textured optical sheets for solar-cells. IEEE Trans Elect Dev 29(2):300–305
302. Green MA (1984) Limits on the open-circuit voltage and efficiency of silicon solar-cells imposed by intrinsic auger processes. IEEE Trans Elect Dev 31(5):671–678
303. Campbell P, Green MA (1987) Light trapping properties of pyramidally textured surfaces. J Appl Phys 62(1):243–249
304. Catchpole KR, Polman A (2008) Plasmonic solar cells. Opt Expr 16(26):21793–21800
305. Novotny L (2007) Effective wavelength scaling for optical antennas. Phys Rev Lett 98(26):266802
306. Fischer UC, Pohl DW (1989) Observation of single-particle plasmons by near-field optical microscopy. Phys Rev Lett 62(4):458–461
307. Novotny L, Stranick SJ (2006) Near-field optical microscopy and spectroscopy with pointed probes. Ann Rev Phys Chem 57:303–331
308. Novotny L, van Hulst N (2011) Antennas for light. Nat Photon 5(2):83–90
309. Alu A, Engheta N (2008) Tuning the scattering response of optical nanoantennas with nanocircuit loads. Nat Photon 2(5):307–310
310. Muhlschlegel P, Eisler HJ, Martin OJF, Hecht B et al (2005) Resonant optical antennas. Science 308(5728):1607–1609
311. Stipe BC, Strand TC, Poon CC, Balamane H et al (2010) Magnetic recording at 1.5 pb m(-2) using an integrated plasmonic antenna. Nat Photon 4(7):484–488
312. Challener WA, Peng CB, Itagi AV, Karns D et al (2009) Heat-assisted magnetic recording by a near-field transducer with efficient optical energy transfer. Nat Photon 3(4):220–224

313. Otto A (2006) On the significance of shalaev's "hot spots' in ensemble and single-molecule SERS by adsorbates on metallic films at the percolation threshold. J Raman Spectros 37(9):937–947
314. Li KR, Stockman MI, Bergman DJ (2003) Self-similar chain of metal nanospheres as an efficient nanolens. Phys Rev Lett 91(22):227402
315. Stockman MI, Faleev SV, Bergman DJ (2001) Localization versus delocalization of surface plasmons in nanosystems: can one state have both characteristics? Phys Rev Lett 87(16):167401
316. Gresillon S, Aigouy L, Boccara AC, Rivoal JC et al (1999) Experimental observation of localized optical excitations in random metal-dielectric films. Phys Rev Lett 82(22):4520–4523
317. Tsai DP, Kovacs J, Wang ZH, Moskovits M et al (1994) Photon scanning-tunneling-microscopy images of optical-excitations of fractal metal colloid clusters. Phys Rev Lett 72(26):4149–4152
318. Albrecht MG, Creighton JA (1977) Anomalously intense raman-spectra of pyridine at a silver electrode. J Am Chem Soc 99(15):5215–5217
319. Jeanmaire DL, Vanduyne RP (1977) Surface raman spectroelectrochemistry. 1. Heterocyclic, aromatic, and aliphatic-amines adsorbed on anodized silver electrode. J Electroanal Chem 84(1):1–20
320. Haes AJ, Haynes CL, McFarland AD, Schatz GC et al (2005) Plasmonic materials for surface-enhanced sensing and spectroscopy. Mrs Bull 30(5):368–375
321. Lakowicz JR, Geddes CD, Gryczynski I, Malicka J et al (2004) Advances in surface-enhanced fluorescence. J Fluoresc 14(4):425–441
322. Chen Y, Munechika K, Ginger DS (2007) Dependence of fluorescence intensity on the spectral overlap between fluorophores and plasmon resonant single silver nanoparticles. Nano Lett 7(3):690–696
323. Munechika K, Chen Y, Tillack AF, Kulkarni AP et al (2010) Spectral control of plasmonic emission enhancement from quantum dots near single silver nanoprisms. Nano Lett 10(7):2598–2603
324. Wu XY, Liu HJ, Liu JQ, Haley KN et al (2003) Immunofluorescent labeling of cancer marker her2 and other cellular targets with semiconductor quantum dots. Nat Biotechnol 21(1):41–46
325. Alivisatos P (2004) The use of nanocrystals in biological detection. Nat Biotechnol 22(1):47–52
326. Melancon MP, Lu W, Yang Z, Zhang R et al (2008) In vitro and in vivo targeting of hollow gold nanoshells directed at epidermal growth factor receptor for photothermal ablation therapy. Mol Cancer Ther 7(6):1730–1739
327. Lu W, Xiong CY, Zhang GD, Huang Q et al (2009) Targeted photothermal ablation of murine melanomas with melanocyte-stimulating hormone analog-conjugated hollow gold nanospheres. Clin Cancer Res 15(3):876–886